Dynamics of Planetary Gear Trains with Consideration of Moving Force Effect and Ring Flexibility

by
© Mohammad Javad Abedinilaksar

A thesis submitted to the School of Graduate Studies in partial fulfilment of the requirements for the degree of

Doctor of Philosophy

Faculty of Engineering and Applied Science

Memorial University

August 2023
St. John's, Newfoundland and Labrador

Abstract

This Ph.D. dissertation focuses on the dynamics of planetary gear trains (PGTs). The direct motivation comes from the wind power industry, where PGT size and load become larger and larger, leading to more complicated dynamic behaviour.

The time-varying mesh stiffness in a gear system causes parametric resonances. Additionally, the multiple planet arrangement in a PGT makes the stability more complicated. This dissertation first investigates the instability caused by the time-varying stiffness, with a focus on the instability related to the repeated natural frequencies caused by the multiple planets. The research employs the method of multiple scales, enabling the derivation of an analytical formulation to describe the instability zones. The obtained results are validated against numerical results from Floquet theory. Notably, the research enhances the existing formulation for instability zones by presenting a slightly larger region for the unstable zone compared to what has been reported in earlier literature. To ensure the accuracy of the proposed formulation, the obtained results are validated against the numerical results from Floquet theory.

With the growing size and load of PGTs, the ring gear in these systems tends to be designed with a relatively thin wall, which leads to significant deflection when subjected to increased loads. In light of this phenomenon, this dissertation focuses on investigating the free vibration behaviour of the ring gear. Initially, the ring gear is simplified as an elastic

ring, and then Euler-Bernoulli and Timoshenko theories are applied based on the ring's thickness. The support is modeled with general elastic boundary conditions to mimic a bolt connection. As a result, the natural frequencies and closed-form mode shapes are derived and analyzed. The obtained results are then compared against Finite Element Method (FEM) results to ensure their validity.

In a PGT, the meshing force between the ring gear and planet gear is not stationary. Instead, it moves along the circumference of the ring with the angular speed of the carrier, creating a moving load excitation. The dissertation thoroughly investigates the dynamics of the ring gear subjected to this moving meshing load. By leveraging the obtained mode shapes, the partial differential equation of the ring is transformed into ordinary differential equations, which are solved using the Maple package. Furthermore, the effect of the moving force is analyzed in great detail, and the critical speed that causes resonances is obtained and examined. The results are compared against data from the literature and validated against FEM results.

Acknowledgement

In the scenario where the world resembles an art gallery, we, as humans belonging to diverse races and colors, act as the visitors appreciating various pieces of art. Among us, there are those who assert that their preferred artwork surpasses others, and some may even attempt to impose their preferences onto others. Despite these disagreements, it remains true that all these artworks were fashioned by a single artist who skillfully created them all. That artist, who deserves acknowledgment, is none other than God, and the diverse belief systems represent these artworks.

I would like to express my sincere gratitude to my uncle, Mr. Javad Abedini Laksar, who sacrificed his life in the Iran-Iraq war, and to the great commander who stated in his testament, 'martyrs are the axis of dignity and respect.' I also want to express my gratitude to my dear parents for their love, outstanding support, and encouragement in helping me achieve my dreams. Without their prayers and love, I would not be where I stand today. Despite feeling guilty for having seen them only twice in the past decade, I am extremely grateful for their understanding.

In addition to my family, I am profoundly grateful and indebted to my supervisors, Dr. James Yang and Dr. Geoff Rideout, for their unwavering support, patience, vast expertise, and invaluable insights. Their encouragement have been instrumental throughout my journey, and I sincerely appreciate their guidance on research, publications, and my dissertation. Without their tireless support, I would not have been able to conduct this research. I am truly grateful for their continued presence and assistance. Also, I would like to express my gratitude to NSERC and Memorial University for their generous financial support, which has been instrumental in the successful completion of my PhD dissertation

Table of Contents

List of Tables

List of Figures

Nomenclature

m_s	mass of the sun gear (kg)
m_c	mass of the carrier gear (kg)
m_p	mass of the planet gear (kg)
m	mass of the ring gear (kg)
J_s	moment of inertia for the sun gear (kg-m^2)
J_c	moment of inertia for the carrier gear (kg-m^2)
J_p	moment of inertia for the planet gear (kg-m^2)
r_s	radius of the sun gear (m)
r_c	radius of the carrier gear (m)
r_p	radius of the planet gear (m)
ρ	Density of the ring gear (kg/m^3)
A	Cross-sectional area of the ring gear (m^2)

E	Young's modulus of the ring gear (Pa)
G	Shear rigidity modulus the ring gear (Pa)
I	Moment of inertia of the ring gear (kg-m^2)
R	Radius of ring gear (m)
R_o	Outer radius of ring gear (m)
R_i	Inner radius of ring gear (m)
b	Face width of the ring gear (m)
t, h	Ring thickness (m)
γ	Shear deformation of the ring gear (rad)
r_{gy}	Radius of gyration of cross-sectional area (m)
θ_s, θ_i	Support location of the ring gear (rad)
θ_f	Position of end of a segment of the ring gear (rad)
ζ	Angle between two adjacent supports of a ring gear (rad)
ν	Poisson's ratio

ε	Strain
n	Number of supports/segments of the ring
k	Shear factor in Abaqus
k′	Ring cross-section shape factor
γ,σ	Pressure angle (rad)
î	Imaginary unit $\sqrt{-1}$
k_{sp}	stiffness of sun-planet mesh (N/m)
k_{rp}	stiffness of ring-planet mesh (N/m)
f	Radial moving force per unit length (N/m)
p	Tangential moving force per unit length (N/m)
φ	Rotation of the ring cross section (rad)
M	Bending moment (N-m)
N	Normal force (N)
Q	Shear force (N)

k_s Rotational spring constant for a ring support (N-m/rad)

k_t Tangential spring constant for a ring support (N/m)

k_r Radial spring constant for a ring support (N/m)

$\delta(t)$ Dirac delta function

ω_c Carrier angular speed (rad/s)

ω_{cr} Critical moving force speed (rad/s)

ω_m Meshing force frequency (rad/s)

F_0 Meshing force amplitude (N)

F_{sh} Meshing force offset (N)

θ_0 Meshing force phase angle (rad)

μ Dynamic coefficient

u_s Static deflection at midpoint of a segment (m)

Δ_{mid} Total deflection of a midpoint of a segment (m)

u_i State variables for sun, carrier, ring, and planet gears (i=s,c,r,p)

CHAPTER 1

Introduction

1.1 Background

Wind power has been harnessed throughout human history for centuries. For more than 1200 years before the Industrial Revolution of the 18th century, windmills and water-driven mills served as the sole sources of power generation. The term "windmill" mainly denotes a grain-processing apparatus powered by wind, used to grind or mill various grains like wheat or corn into flour, which was essential for making bread. These devices were present in ancient civilizations such as Egypt, Persia, Mesopotamia, and China [1-3]. During the 7th century BC, King Hammurabi of Babylon introduced a strategy to utilize vertical-axis wind machines for irrigating the productive plains surrounding the Euphrates and Tigris Rivers [1,2]. One of the earliest recorded pieces of evidence of using windmills dates to the 7th century in Sistan, Persia

(modern-day Iran) [3]. This period marks one of the earliest documented instances of their usage for tasks such as corn grinding, flour milling, and water pumping. The initial windmill designs consisted of lightweight wooden sails arranged vertically and connected to a central vertical shaft through horizontal struts, as shown in Fig. 1.1. As time progressed, wind technology spread to Europe through merchants and Crusaders during the 11th century, and later on, European immigrants introduced wind energy technology to the Western Hemisphere [4].

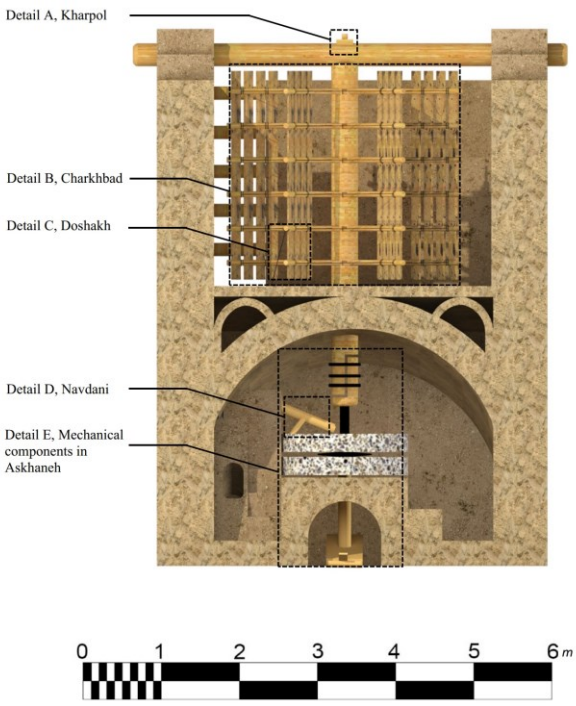

Fig. 1.1 *Cross Section of Persian Asbads (windmill) [5]*

The scarcity of oil during the 1970s sparked a notable surge in the inclination towards investing in wind turbines as a viable electricity-generating option in lieu of fossil fuels. The primary motivation behind this shift was the recognition of wind power's attributes, such as being renewable, sustainable, dependable, environmentally friendly, and cost-effective.

Wind energy extraction has emerged as a rapidly expanding technology over the last few decades, making significant contributions to economies worldwide. In the United States, wind power stands as one of the primary renewable energy sources and is anticipated to become the dominant form in the coming decade [6,7]. In Canada, wind energy fulfills approximately 6-8 percent of the country's electricity demand, generating enough power for about 3.3-3.6 million households [8]. From 2005 to 2019, wind power generation in Canada increased from 1,552 GWh to 32,333 GWh, representing 5.1% of total electricity production in 2019 [8]. The cumulative installed capacity in Canada has shown significant growth, as depicted in Fig. 1.2, and is projected to continue expanding by an additional 2400 MW until 2025.

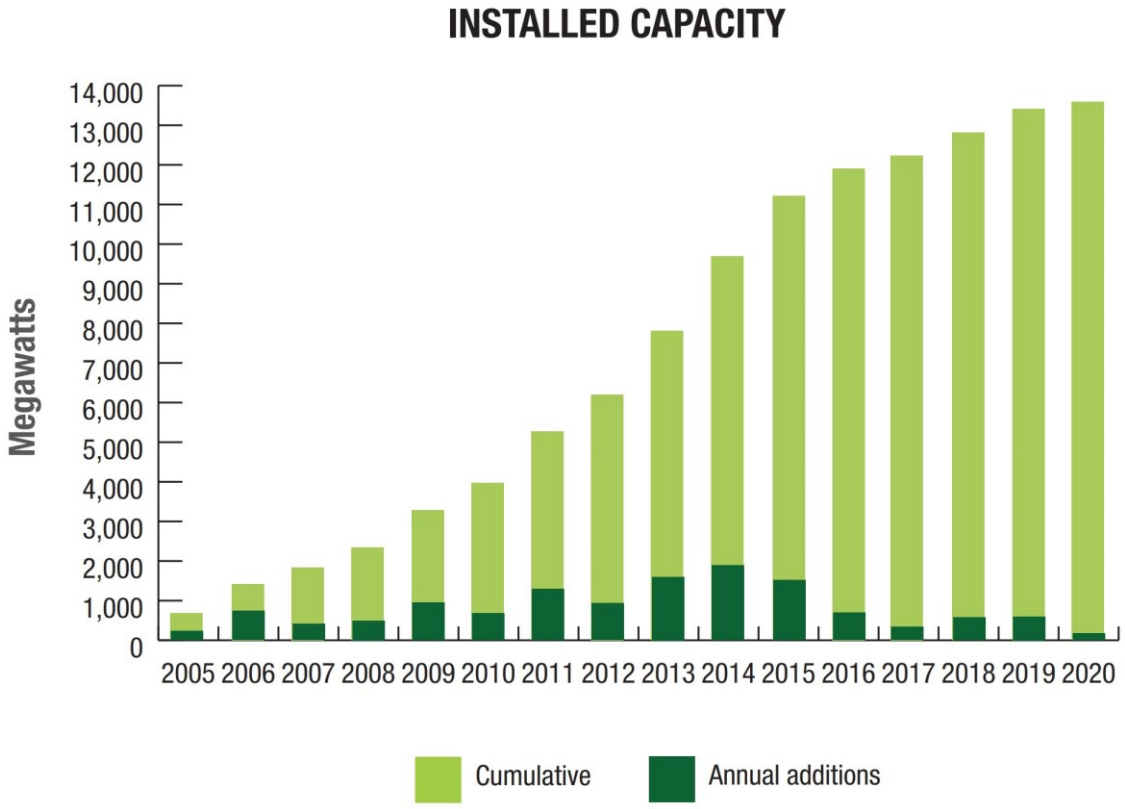

Fig. 1.2 *Installed Wind Power Capacity in Canada (in MW) [8]*

A wind turbine is a device that can transform the energy of wind into electricity by harnessing its kinetic force. Currently, the most widely utilized type of wind turbine is the

Horizontal Axis Wind Turbine (HAWT). These turbines employ aerodynamic blades, known as airfoils, which are connected to a rotor through a gear box. The Planetary Gear Train (PGT) stands out as the prevailing transmission system in wind turbines among various gearbox types, owing to its unique attributes. Fig. 1.3 from [9] depicts the main mechanical elements that exist within the nacelle of a typical wind turbine, showcasing the position of the planetary gearbox in relation to the other components.

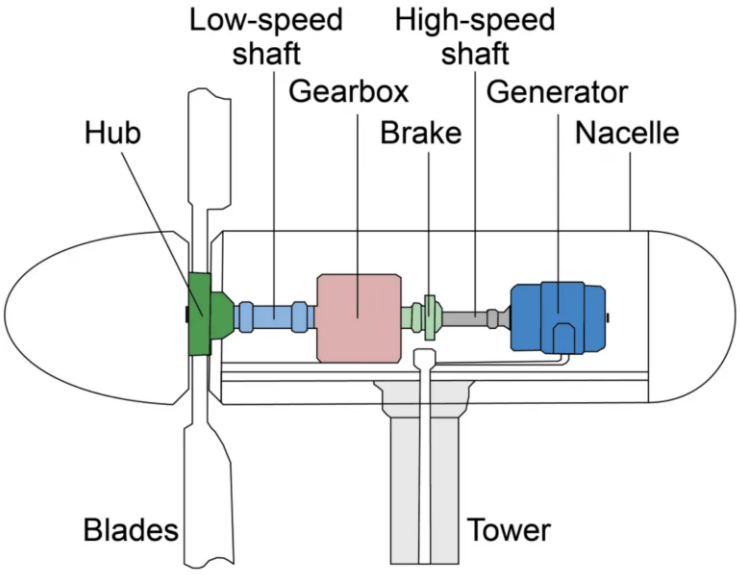

Fig. 1.3 *Schematic of a HAWT [9]*

PGTs were initially devised by the Greeks more than two millennia ago, aiming to forecast planetary motions within the solar system [10]. A planetary gear system is a specific type of gear arrangement that involves the placement of at least two gears in such a way that the center of one gear revolves around the center of the other. A carrier is responsible for connecting the centers of these two gears and rotates to carry the planet gear (one of the gears) around the sun gear (the other gear). Additionally, the planet gear rotates within another gear called the ring gear. The ring gear and planet gear mesh together, enabling their pitch circles to roll without slipping. All the planet gears are mounted onto a singular rotating component

referred to as the carrier. Within the context of [11], Fig. 1.4 portrays a disassembled wind turbine's PGT, where the sun and a planet gear are prominently displayed.

Fig. 1.4 *Disassembled ring gear of a wind turbine PGT [11]*

PGTs possess superior strength and power density, allowing them to handle higher levels of torque and achieve greater reductions in a smaller, more compact form. Moreover, they demonstrate remarkable resilience to intense impacts and possess the ability to withstand substantial overhung loads, owing to their distinctive self-aligning properties.

1.2 Problem Statement

Although wind turbines offer numerous advantages, there exist significant challenges when it comes to harnessing their energy. One prominent difficulty is the occurrence of component failure. Wind turbines are often situated in remote or hard-to-reach locations, making maintenance and repairs challenging. As a result, any failure incurred leads to costly

repairs and replacements. A study conducted over a span of 13 years investigated the failure and downtime of various components in two types of land-based wind turbines [12]. The surveyed components include electrical systems, electrical controls, hydraulic systems, rotor hubs, mechanical brakes, rotor blades, gearboxes, generators, drive trains, and yaw systems. According to the findings in [12,13], gearboxes, drive trains, and rotor blades exhibit the highest downtime per failure compared to other components. These parts form the core of the wind turbine's mechanical structure, being directly exposed to wind and responsible for transferring the generated torque from the blades to the generator.

The importance of studying the vibration of the planetary gearbox in wind turbines arises from the critical role this component plays in the overall performance and reliability of the turbine system. The planetary gearbox serves as a vital link between the low-speed shaft, driven by the wind turbine rotor, and the high-speed shaft, connected to the generator. However, the dynamic nature of the gearbox operation and the varying load conditions impose significant challenges in terms of vibration characteristics, leading to potential performance degradation, increased maintenance costs, and even premature failures.

The problem lies in the fact that the vibration behaviour of the planetary gearbox in wind turbines has not been thoroughly understood and characterized, thus hindering the development of effective maintenance strategies and reliable designs. The complex nature of gear meshing, high rotational speeds, moving loads, and the presence of multiple gear stages in the planetary gearbox contribute to intricate vibration patterns, including resonances. These vibrations can lead to excessive noise, accelerated wear and tear, lubrication issues, instabilities, and even catastrophic failures if left unaddressed.

Furthermore, the consequences of gearbox failures extend beyond the immediate operational and financial implications. Downtime for repairs not only reduces energy production and revenue generation but also affects the overall grid stability and renewable energy integration goals. Timely detection and mitigation of vibration-related issues in the planetary gearbox are essential for optimizing wind turbine performance, maximizing energy production, extending the service life of components, reducing maintenance costs, and ensuring the long-term sustainability of wind power generation. Wind turbine planetary gearboxes are a significant source of downtime and repair costs. Despite being designed for a 20-year lifespan, they frequently fail earlier due to fluctuating torques caused by wind speed variations. As the most expensive parts of a wind turbine, gearbox failures are a primary concern in the turbine's design. Improving the reliability of gearbox designs is one of the key points to reduce wind turbine downtime and make wind energy competitive as compared to fossil fuels. Failure of gear components would result in a pause in the operation, which can cause financial loss. Thus, any scientific effort toward predicting and avoiding failure in the gearbox system becomes an element of interest.

Therefore, comprehensive studies on the vibration characteristics of the planetary gearbox in wind turbines are crucial. By investigating and analyzing the complex vibration phenomena, researchers can identify the root causes of failures due to vibrations and predict and avoid the failure. Ring gear is one of the important elements of planetary gearboxes that its vibrations need to be fully understood since it can adversely affect the system's efficiency and power transmission capabilities [14]. Hence, there is a pressing need to comprehensively study and analyze this important element and investigate the vibrations of this part due to the moving force caused by the rotation of planet gears. By understanding the root causes and

characteristics of these vibrations, engineers and researchers can develop effective strategies for their mitigation. Ultimately, a thorough understanding of ring gear vibrations of PGTs will result in enhanced performance, improved reliability, and an extended lifespan of planetary gearboxes, leading to more efficient and sustainable mechanical systems overall. Hopefully, research endeavors like the current study will contribute to the widespread adoption of wind energy, promoting sustainable and clean power generation while reducing dependence on conventional fossil fuels.

1.3 Research Overview

Vibrations in the gearbox system are significant areas of concern when it comes to wind turbine structures. These vibrations have the potential to lead to various issues such as excessive noise and premature failure, significantly reducing the expected lifespan of the turbines. This research offers a chance to make progress in this significant scientific area by introducing a dynamic model and conducting an analysis that will be beneficial for the evaluation of planetary gearboxes. Therefore, this dissertation focuses on the the following four primary categories that encompass the main topics of investigation in this field.

- The calculation of vibrations in planetary gear transmissions is confronted by a significant problem related to parametric instabilities. These instabilities are primarily induced by the varying stiffness of gear meshes and the changes in tooth stiffness as the number of teeth in contact fluctuates. It is crucial to emphasize that this specific issue stands as the most critical factor contributing to the occurrence of unexpected

vibrations in PGTs. Therefore, it becomes imperative to allocate considerable attention and resources towards understanding and addressing this particular area of concern.

- In addition, it is important to note that thin-walled ring gears employed in PGTs exhibit elastic characteristics when subjected to heavy loads during operation. Consequently, the deformation of the ring gear significantly influences the dynamic response of the entire system. As a result, comprehensively investigating the vibration behavior of the elastic ring is of utmost significance to prevent structural failure.

- Furthermore, it is important to address the crucial role that constraints play in the behavior of a ring. The behavior and response of a ring structure are profoundly influenced by the specific boundary conditions imposed upon it. Consequently, in order to gain a comprehensive understanding of ring dynamics, it is imperative to conduct a thorough examination of the diverse range of boundary conditions that can potentially affect the system. This deeper analysis enables researchers to explore how variations in boundary conditions, such as fixed supports, free ends, or general elastic restraints, shape the structural behavior of the ring.

- The ring gear in PGTs is generally designed to be thin to reduce the total weight. This facilitates load sharing among the planet gears; however, it inevitably leads to increased elastic deformation under working loads. Consequently, the effect on the dynamics of the thin-walled ring gear becomes significant. Moreover, the excitation force resulting from the interaction between the planet and ring constantly moves along the circumference, further complicating the problem. This characteristic classifies the study of PGT vibrations as moving-force problems. Numerical methods are primarily

employed to investigate moving-force problems due to the complexity of the models. The lack of proper analytical methods and exact solutions has created gaps in the existing literature, necessitating further research.

This dissertation aims to examine those four specific areas pertaining to planetary gearbox systems. PGTs find extensive utilization across various fields, such as helicopters, automobiles, wind turbines, mobile satellite receivers, and turbomachinery blades, among others. Despite the acknowledged importance of PGTs in diverse industries, certain fundamental gaps in existing literature necessitate further investigation. These crucial gaps need to be addressed for a deeper analysis of wind turbine PGT dynamics.

These gaps primarily revolve around comprehensive modeling of PGTs, determining stability regions of the system considering repeated natural frequencies, incorporating the effects of various types of boundary conditions, and examining the behavior of the elastic ring when subjected to a moving force. The objective of this thesis is to identify an appropriate model and methodology that can effectively address those research gaps in modeling a PGT. This research holds immense importance due to its findings and innovative methods, which have implications that extend well beyond the wind power industry. The developed techniques and analyses from this research have wide-ranging applicability, not limited to wind turbines alone, but also benefiting the automation and aviation sectors. The ensuing dissertation endeavors to address the knowledge gaps in current literature by offering a systematic and theoretical analysis.

While those gaps are briefly mentioned in the preceding chapter, it is in Chapter 2 that they are extensively explained. This chapter delves into the specifics and intricacies of each gap,

providing a thorough examination and analysis. This work takes a focused and deliberate approach to address each of these gaps in a targeted manner. In Chapter 2, a meticulous examination is undertaken to elucidate the intricacies of these gaps, providing a thorough understanding of their significance. The chapter not only highlights the shortcomings present in the existing literature but also emphasizes the unique and innovative approach adopted in this research to bridge those gaps. The methodology developed throughout this endeavor can be applied to a majority of engineering industries that deal with ring or planetary gear transmission units.

1.4 Research Contributions

This research aims to investigate the dynamic behavior of a planetary gear train and thin-walled rings in the context of wind turbine applications. More specifically, the contributions of this research to the state of the art can be categorized as follows:

a. Presenting closed-form equations for deriving the natural frequencies of a planetary gearbox with time-varying stiffnesses between the gears.

b. Introducing a methodology to calculate the precise stability regions for PGTs when one or more natural frequencies are degenerated (repeated).

c. Developing the orthogonality relationships between any two distinct mode shapes of a flexible ring in a PGT.

d. Presenting a method for investigating the vibration of a ring subjected to a sinusoidal moving force and analyzing the effects of the moving force on the ring's behaviour.

e. Deriving a closed-form equation for the critical speed of a moving force sweeping across a ring.

f. Introducing a combination of meshing and carrier frequencies as the secondary source of instability for the ring gear of a PGT in the presence of a moving force.

Beyond the aforementioned contributions to PGTs, this research aims to provide further insights into the dynamics of rings. The following items listed below represent additional contributions of this research. A thorough study of PGTs necessitates the consideration of the flexibility of the ring gear. This inclusion of the ring gear's flexibility has opened up new avenues for analyzing the vibration characteristics of both thick- and thin-walled rings. As a result, this research also makes notable advancements in the following areas of the state of the art:

a. Developing an accurate mathematical model to represent an elastic ring gear.

b. Developing an analytical technique to analyze the vibration of a ring under various boundary conditions.

c. Comparing the Euler-Bernoulli and Timoshenko theories for a ring constrained by general boundary conditions.

d. Investigating the individual effects of radial, tangential, and rotational stiffnesses of a support on the vibration of a ring.

1.5 Organization of Thesis

The thesis is organized as below:

- Chapter 1 (the current chapter) encompasses the background information, the research contribution made to the current knowledge in the field, a concise overview of the research structure, and the organization of this dissertation.
- In Chapter 2, an extensive review of previous literature is conducted, with particular emphasis on the following subjects:
    - PGT dynamics models and the solution methods for dynamic equations;
    - The instability of PGTs caused by time-varying nonlinear meshing stiffness;
    - Parametric instabilities for modes with distinct-degenerate (distinct-repeated) and degenerate-degenerate (repeated-repeated) frequencies in a PGT;
    - Ring vibration considering the effect of various boundary conditions;
    - Comparison between Euler-Bernoulli and Timoshenko theories for a ring;
    - Moving force analysis of a PGT ring with the implementation of wind turbines;

This chapter also highlights the gaps in existing literature and positions the current research in relation to previous works.

- In Chapter 3, a non-linear multi-degree-of-freedom planetary gear train with three planet gears is introduced. The chapter considers time-varying gear meshes between each pair of gears. To investigate parametric instabilities, the perturbation method is utilized. Specifically, the emphasis is on instabilities associated with repeated natural

frequencies. The analytical findings obtained from the method proposed in this chapter are subsequently validated using numerical results obtained from the Floquet theory. A version of this chapter was published in the Journal of Vibration Testing and System Dynamics in 2021.

- Chapter 4 centers around the examination of the PGT ring alone, specifically exploring the system's response under two commonly encountered boundary conditions. The chapter addresses the free in-plane vibration problem of the system, presenting the analytical solutions which are subsequently validated by comparing them with numerical results obtained from simulations conducted in the Abaqus package. A version of this chapter was published at the Canadian Society of Mechanical Engineering (CSME) congress in 2020.

- Chapter 5 builds upon the methodology employed in Chapter 4 and introduces a novel technique for analyzing thin-walled rings under general boundary conditions. While there is some overlap in the literature review between this chapter and Chapter 4, Chapter 5 presents a distinct model where the ring is supported by multiple elastic supports. These supports are represented using linear springs in the radial, tangential, and torsional directions to mimic real-world bolt supports. This enhanced model surpasses the one presented in Chapter 4 and is capable of offering solutions for both common and intricate scenarios. Furthermore, the findings from this chapter hold substantial significance beyond PGTs and can be applied to any other engineering structures featuring a ring. A version of this chapter is published in the Springer Journal of Mechanical Science and Technology in 2023.

- Chapter 6 serves as a continuation of Chapter 5, focusing on incorporating the influences of rotary inertia and shear deformation. This chapter presents an analytical approach for determining precise solutions for the natural frequencies and corresponding mode shapes of a ring subjected to general elastic boundary conditions. Both Euler-Bernoulli and Timoshenko theories are utilized in this chapter, allowing for a comparison of their respective results. The findings presented in this chapter provide insights into the feasibility of employing the Euler-Bernoulli theory for modeling PGT rings. A version of this chapter was published and presented at the Canadian Society of Mechanical Engineering (CSME) congress in 2020.

- Chapter 7 offers an analytical examination of the vibration characteristics of an elastic ring in a PGT subjected to a sinusoidal moving force. This moving force arises from the rotational movement of a planet within the ring gear. Given the complexity of this scenario, multiple resonant conditions occur simultaneously. Therefore, this chapter conducts a parametric study to explore the relationship between the excitation frequencies. Additionally, the influence of the critical speed of the moving force is discussed. The results obtained in this chapter were compared with those from the previous literature and the simulation results conducted in Abaqus. A version of this chapter has been under review for publication in the Journal of sound and vibration.

- Chapter 8 summarizes the key novelties of this research, along with providing suggestions for future research directions.

Table 1.1 provides an inclusive inventory of publications that have been generated as a result of this ongoing research.

Table 1.1. List of publications

Chapter	Paper Title	Conference or Journal	Status
3	Stability Analysis of a Planetary Gear Train Having Repeated Natural Frequencies	Journal of Vibration Testing and System Dynamics, 2021	Published
4	Free Vibration Characteristics of a Thin-Walled Ring Under Different Boundary Conditions	CSME Congress, 2020	Published
5	Free In-plane Vibration of Thin-Walled Rings with Elastic Supports	Springer Journal of Mechanical Science and Technology, 2023	Published
6	Vibration Characteristics of a Ring Under General Boundary Conditions using Euler-Bernoulli and Timoshenko Theories	CSME Congress, 2022	Published
7	In-plane Forced Vibration of a Thin-Walled Ring with Hinged Supports Undergoing Sinusoidal Moving Force	Journal of Sound and Vibration	Under Revision

References

[1] S. Mathew, Wind energy: Fundamentals, resource analysis and economics (2007). https://doi.org/10.1007/3-540-30906-3.

[2] T.M. Letcher, Wind Energy Engineering: A Handbook for Onshore and Offshore Wind Turbines (2017).

[3] W. Shepherd, L. Zhang, Electricity generation using wind power, (2011). https://doi.org/10.1142/7703.

[4] https://www.eia.gov/energyexplained/wind/history-of-wind-power.php

[5] M. Zarrabi, N. Valibeig, 3D modelling of an Asbad (Persian windmill): a link between vernacular architecture and mechanical system with a focus on Nehbandan windmill, Herit Sci. 9 (2021). https://doi.org/10.1186/s40494-021-00587-0.

[6] Energy Information Administration (EIA), Short-Term Energy Outlook Forecast highlights (2022), https://www.eia.gov/

[7] U.S. Energy Information Administration, Annual Energy Outlook 2022, With Projections to 2050, (2022).

[8] Energy fact book 2021-2022, Natural Resources Canada, Tech. Rep., (2022).

[9] U.S. Department of Energy (DoE), Energy Efficiency & Renewable Energy (EERE), The Inside of a Wind Turbine (2021), https://www.energy.gov/eere/wind/wind-energy-technologies-office.

[10] M.T. Wright, The Antikythera Mechanism reconsidered, Interdisciplinary Science Reviews. 32 (2007). https://doi.org/10.1179/030801807X163670.

[11] https://meproduction.com/front-page/wind-turbine-gearbox-repair/

[12] S. Sheng, Report on Wind Turbine Subsystem Reliability - A Survey of Various Databases (Presentation), National Renewable Energy Laboratory (2013).

[13] E. Aydin, Determination of best drive train technology for future onshore wind turbines as a function of the output power. Master's thesis, The Department of Electrical Engineering of the Eindhoven University of Technology (2013).

[14] T. L. Krantz, Mechanical Systems Technology Branch Research Summary, NASA Technical Memorandum, 106329 (1993), pp. 1985-1992.

CHAPTER 2

Literature Review

2.1 Introduction

Planetary gear trains (PGTs) offer numerous advantages over parallel gearing systems, rendering them highly prevalent in various applications such as automobiles, helicopters, and wind turbines. Their exceptional characteristics, including a wide range of speed ratios, compactness, and high efficiency, make them a ubiquitous engineering structure across multiple industries. When designing PGTs, dynamics plays a pivotal role, especially in applications involving high speeds and heavy loads. Vibration is another significant concern as it can impact the reliability and fatigue life of a PGT. Moreover, certain elements within PGTs can be more critical than others depending on the specific application. For example, in wind turbine applications, the deformation of the ring gear is of great interest.

A thorough background review is conducted in this chapter, providing a comprehensive understanding of the existing research in the field. An in-depth exploration is undertaken to examine the literature related to the ring gear of PGTs, where the effects of boundary conditions for both Euler-Bernoulli and Timoshenko theories are analyzed. The investigations of those aforementioned topics lay the groundwork for the subsequent analysis of moving loads and provide valuable insights for further research in the field of planetary gear trains.

Finally, at the end of this chapter, the current status of this research in relation to the previous literature has discussed. It is important to note that, due to the manuscript-format nature of this dissertation, there may be some overlap between the literature cited in this chapter and the subsequent chapters. However, such overlap is necessary for maintaining a coherent and thorough analysis of the subject matter.

2.2 Dynamics and Stability of PGTs

The dynamics of gears have been a subject of interest for a considerable period [1-4]. In general, there are three primary categories of models used to showcase the dynamic modeling of PGTs. These include the lumped parameter model, the finite element model, and the hybrid finite element-lumped parameter models. The selection of a particular model depends on the specific research objectives and the level of complexity involved.

Lin and Parker [5] conducted research on the dynamic behaviour of PGTs using a lumped parameter model. Their model represented the carrier and each gear with three degrees of freedom, consisting of two transverse motions and one rotational motion. To

account for the gear meshing between sun-planet and ring-planet pairs, springs were employed. Kahraman [6] utilized the same model to investigate the natural frequency of a PGT. He compared the natural frequencies obtained from a purely torsional model with those from a torsional transverse model. In another study, Kahraman [7] examined the impact of the planet meshing phase on the dynamic response. This particular model considered helical gears, leading to a three-dimensional representation that involved six degrees of freedom for each component; three rotational and three translational degrees of freedom. Wu and Parker [8] employed the perturbation method to solve the dynamic equations of PGTs. Their findings demonstrated that all vibration modes could be categorized into four modes: rotational, translational, planetary, and purely ring modes. Sondkar and Kahraman [9] applied the summation method to study the dynamic responses of a double-helical PGT by solving the dynamic equation. Their model incorporated linear, time-invariant meshing between the gear pairs. Wei et al. [10] employed a numerical precise integration method to solve the dynamic equations of multistage planetary gears. Their approach was particularly suitable for equations with a high degree of freedom. An additional frequently employed method for investigating the dynamics of PGTs involves utilizing the Newmark algorithm in conjunction with the Newton-Raphson method at specified time intervals [11,12].

Studying the dynamics of PGTs in the presence of nonlinear phenomena such as mesh stiffness variation is quite complex because the time-varying stiffness of the gear meshing introduces internal excitation to the system, leading to complex resonances or instability [13-14]. Mesh stiffness variation, caused by changes in the number of teeth involved in a mesh contact, is known as one of the significant sources of nonlinearity. Researchers have introduced different solution methods to overcome this complexity without sacrificing much accuracy. In

early studies, purely linear models were commonly used [15,16]. Kahraman [17], the pioneer in this area, developed a nonlinear dynamic model of planetary gearboxes, considering numerous nonlinear parameters such as mesh stiffness variation. Their work focuses on studying the influence of design parameters on dynamic load sharing factors. Interested readers are directed to the following two review papers [18,19]. Additionally, Ozguven and Houser [20] conducted an extensive bibliography review of early investigations into the modeling of gear systems. Over the past decade, several researchers have conducted studies on nonlinear dynamics modeling [21,22]. One commonly used approach to examine the effects of nonlinearity on system dynamics is the finite element method [23-27]. An excellent example in this area is the research conducted by Schmidt [28], where they studied the vibrations of a gearbox with parametric excitation caused by periodic tooth stiffness changes. Taheri Kahnamouei, and Yang [29] employed an energy-based statistical linearization method to study a nonlinear dynamic model of a spur gear pair, taking into account both backlash and time-varying mesh stiffness. The results demonstrated that nonlinearity has a substantial impact on the system's response, particularly at low input torques. The presence of multiple gear meshes in PGTs further complicates the instability. Numerous researchers have investigated the instability of PGTs caused by the time-varying meshing stiffness [5,6-30]. The inclusion of multiple planet gears in a PGT results in the observation of repeated natural frequencies. Kahraman conducted a concise and insightful analysis of this phenomenon using a pure rotational lumped parameter model [14]. Subsequently, Lin and Parker conducted more comprehensive investigations with refined models [5,30-31]. Some studies extended their analysis to include the effects of ring gear flexibility [32] and viscous damping [33].

Despite the aforementioned research and a few additional articles [34,36,37], the impact of repeated natural frequencies of PGTs has not been adequately addressed to date. Hence, there is a need to develop a new approach to investigate the stability of a PGT when one or more natural frequencies of the system are repeated (degenerate). In the current study, a relatively simple pure rotational lumped parameter model is utilized. The stiffness of each gear mesh (k_{sp}^{i} and k_{rp}^{i}) is assumed to vary with time due to the changing tooth contact. By decomposing the time-varying stiffness into a Fourier series, the governing equations of the model are analytically derived. In light of this, this dissertation utilizes the multiple-scale method to solve those governing equations and derive the closed-form equations that represent the stability regions of a PGT at the presence of repeated natural frequencies.

2.3 Free Vibration of the Ring Gear of a PGT

In the majority of literature studying the dynamics of PGTs, the ring has been modeled as a rigid body. However, thin-walled ring gears exhibit elastic behavior under operating conditions, particularly in heavy load applications such as PGTs used in wind turbines. Therefore, the deformation of the ring gear has a critical effect on the dynamic behavior of the system [38]. The dynamic characteristics of free rings have been investigated in numerous studies [39-44], where closed-form equations for evaluating natural frequencies and associated mode shapes were derived. Hoppe [39] and Love [45] are recognized as pioneers in the study of thin-walled ring vibrations. Building upon their theories, subsequent works have expanded and enriched both theoretical developments and practical applications.

Chidamparam and Leissa [46] conducted a comprehensive literature review on ring vibration prior to 1993.

Generally, analyzing the vibration of a thin-walled ring using beam theory is more complex than similar problems involving straight beams. The complexity arises from the fact that, unlike straight beams, the structural deformations in a ring depend on rotational, radial, and coupled tangential displacements [47]. The extensibility of the arc axle is another significant variable that plays a major role in the analysis of rings. The axial inextensibility impacts the stiffness of the ring and, consequently, the natural frequencies. Notably, according to the study conducted by Chidamparam and Leissa [48] and Chidamparam [49], this effect is particularly pronounced for shallow arches. Structures with ring geometry find applications not only in mechanical systems such as bearings, rotors, and gears but also in interdisciplinary areas such as bioengineering and vibration control. In the application of PGTs, numerous studies have been conducted to examine the impact of ring gear elasticity on the dynamics of the structure. Research in this area has primarily been conducted using either analytical methods [50-52] or finite element methods [53-58]. Kahraman et al. [59,60] employed a semi-analytical approach to investigate the effects of ring thickness. Their work involved examining the stress, deflection, and load-sharing among the planet gears. The results demonstrated that the elasticity of the ring gear significantly influences the load sharing among the components [61]. Yong Hu et al. [62] conducted an analysis on the impact of the ring gear on the load distribution in PGTs. Their findings revealed that the elasticity of the ring gear had a greater influence on the dynamics compared to other components. Their analysis demonstrated that the deformation of the ring significantly affected the meshing between the ring and planet gears, leading to changes in the load distribution within the PGTs.

2.4 Effects of Boundary Conditions

For a free ring without constraints, closed-form expressions for natural frequencies and mode shapes were derived in [41,44,63-68]. Archer [69] was the first to investigate the dynamics of rings using the Euler-Bernoulli beam theory, neglecting axial extensibility. They introduced a damping parameter and modified Love's [45] equations to analyze the in-plane vibration of an incomplete circle. Wu and Parker [41] utilized perturbation and Galerkin methods to investigate the vibrations of a ring with an elastic foundation. Zhang et al. [42] examined the natural frequencies and mode contaminations of a spinning ring. Rao and Sundararajan [64] determined the natural frequencies and associated mode shapes of a ring supported rigidly using a differential equation formulation. However, their numerical results appear to be accurate only within a limited range of radial supports [70]. In cases with a small or large number of radial supports, their method was not entirely satisfactory. Sahay and Sundararajan [71] addressed this issue by presenting a process applicable to rings with numerous supports, although it requires the assumption of cyclic symmetry. The transfer matrix method has been employed by several other researchers [72-74] to yield more accurate results for natural frequencies and modes of a ring supported by multiple radial supports. However, some mode shapes were neglected as they assumed that the overall vibrational mode of the entire ring could be determined by considering the same behavior of one studied segment for all other segments. Malik and Mead [70] employed the wave approach and determined the natural frequencies by analyzing the propagation constants of the ring, treating it as an endless periodic structure. Zakrzhevskii et al. [75] utilized a numerical method to solve a boundary-value problem (BVP) for an elastic ring fixed at a specific point. Eisenberger and

Efraim [76] obtained the natural frequencies of a ring under fixed and hinged boundary conditions, and they compared their results with previous studies.

Despite the extensive body of literature cited above, it is evident that while many researchers have investigated vibration suppression in rings, studies on the effects of boundary conditions are limited to a few published papers, primarily focusing on rings with hinged or fixed supports. Given that the accuracy of any analysis model relies on the correct and appropriate handling of boundary conditions, it is crucial to study the effects of different boundary conditions. In examining the effects of different constraints on rings, various approaches have been employed in the literature, including the complementary transfer matrix method [72], transfer matrix method [73,74], Green's function [71], wave approach [70] and finite element method (FEM) [23,24]. These methods are capable of addressing complex problems involving rings with different support constraints. However, none of the works cited above presented an analytical formulation for mode shapes and natural frequencies of a ring with general elastic boundary conditions. This research addresses this gap as one of its objectives.

2.5 Euler-Bernoulli vs Timoshenko Theory

Three main theories exist in the literature to describe the dynamics of rings: Euler-Bernoulli, Rayleigh, and Timoshenko theories. The Euler-Bernoulli theory dates back to the 18th century. However, due to its simplicity and reasonable engineering approximations, it is still the most commonly used theory for describing ring dynamics. In some literature, this theory has alternatively been referred to as the classical ring theory. In the Euler-Bernoulli theory, the

effects of shear deformation and rotary inertia are neglected, and the strain energy and kinetic energy are assumed as functions of bending and lateral displacement, respectively. This theory intends to overestimate the natural frequencies and is suitable for thin-walled rings. The Rayleigh beam theory considers a rotation of cross section after deformation and provides improvement on the Euler-Bernoulli beam theory by introducing the rotary inertia effect. This theory considers both bending and shear deformation in the deflection equation, providing a more accurate description of beam behavior compared to Euler-Bernoulli. While this theory improved upon the Euler-Bernoulli theory, it was able to fully resolve the problem of overestimating the natural frequencies. Timoshenko [77] focused on bridging this gap and demonstrated that the overestimation of natural frequencies in the Euler-Bernoulli theory can impact the system's response in its higher modes. He developed a comprehensive theory for beams (and rings), in which the effects of shear deformation and rotary inertia were both incorporated into the Euler-Bernoulli model [77,78]. These modifications made the Timoshenko model more appropriate for thick-walled rings and high-frequency responses. Table 2.1 provides a summary of the aforementioned models.

Table 2.1. Four different beam theories [79]

Ring Model / Theory	Lateral Displacement	Bending Moment	Shear Deformation	Rotary Inertia
Euler-Bernoulli	YES	YES	NO	NO
Rayleigh	YES	YES	NO	YES
Timoshenko	YES	YES	YES	YES

Several research papers analyzing rings (or curved beams) [40,42,43,46] have been conducted based on Love's curve shell theory [45]. The governing differential equations

presented in Love's formulae consist of two coupled equations in the radial and tangential directions. These coupled differential equations can be reduced to a sixth-order ordinary differential equation with constant coefficients in the tangential direction. Many researchers have followed this approach, leading to the establishment of the bending theory of thin-walled rings. However, Love's theory does not perform well for thick rings as it does not consider rotary inertia and shear deformation [41,74,80]. Wolf [81] analyzed the free vibration of a circular arch using the straight elements method. In their model, the effect of rotary inertia was included while the effect of shear deformation was neglected. Veletsos et al [65] assumed that the tangential displacement was independent of the radial deformation and considered extensibility in their model, while neglecting the effects of shear deformation and rotary inertia. They developed a model for curved beams that could alternatively be applied to rings. Austin and Veletsos [82] investigated the effects of rotary inertia and shear deformation on a free ring and compared the natural frequencies for both cases. Irie et al. [83] employed the transfer matrix approach to determine the natural frequencies of in-plane vibrations in a thick-walled ring with a uniform cross-section, considering various combinations of conventional boundary conditions. Issa et al. [84] developed a unified theory for a thick-walled ring and derived the general dynamic stiffness matrix. Additionally, their model took into account the extensional effect of the neutral axis. Han et al. [79] examined the aforementioned four theories and demonstrated that the responses of the Euler-Bernoulli and Rayleigh models are very similar. Therefore, in this research, only two well-known theories, namely Euler-Bernoulli and Timoshenko, are considered and compared.

2.6 Moving Load

The dynamics of moving loads were first recognized in the mid-19th century. In PGTs the interaction between the planet and ring gear causes a moving excitation force that travels internally along the ring's circumference at a constant speed. This meshing force induces deflection on the ring gear. Hence, it is essential to incorporate the moving force into the model and examine how it influences various components of a PGT, with particular attention to its effects on the ring gear. One of the early studies on rings subjected to a moving load was conducted by Huang et al. [85]. They presented a problem of a harmonically varying moving load and compared the effects of a concentrated moving load with a distributed load. They also calculated the percentage error if the distributed load was assumed to be a point load. Zhao et al. [86] examined a ring-shaped structure and studied the parametric vibration of the system subjected to a moving load. Similarly, Metrikine and Tochilin [87] investigated the vibration of an elastic ring with moving concentrated forces to model train wheels. Forbes and Randall [88] also explored the response of a circular ring under a moving load. They categorized their solutions into three cases: magnitude-varying moving load, phase-varying moving load, and non-uniform continuous moving load. The ring model in their study was unconstrained, allowing them to avoid the complexity of considering boundary conditions. Joseph and Wilson [89] conducted an experimental study on the vibrations of rings subjected to continuous moving loads. Yau et al. [51] enhanced previous models by analyzing the dynamic response of rings caused by moving forces, including dedicated masses. They investigated both vertical and horizontal moving loads in their research. Finite element analysis is a common method used to analyze moving load problems, and it has gained popularity among many researchers, such as [29,90,91]. Huang et al. [92] investigated the dynamic response of curved beams due to moving

sprung masses. Another valuable method for studying the dynamic response of a beam subjected to a moving load is utilizing the Laplace transform technique. Huang et al. [85] employed this method to develop an accurate solution for the dynamic response of a ring experiencing a moving load. The numerical study conducted by Taherikahnamouei and Yang [29] examined the effect of different supports on the dynamic response of the ring. Canchi and Parker [93,94] modeled the interaction between ring-planet gears in a PGT by representing the system as a circular ring with moving springs. They utilized numerical methods to investigate the parametric instabilities of in-plane bending vibrations, aiming to validate the parametric analytical approach they studied. Their research aimed to uncover the effects of various system parameters on the instability boundaries of the ring. Similar to [88], the model used in [93,94] was also unconstrained, meaning that the effect of boundary conditions was not considered in the calculations. Systematic methods for dealing with dynamics under moving loads are well-documented by Ouyang [95] and Fryba [96].

2.7 Place of Current Research in the Literature

Despite the aforementioned points highlighted in subsection 2.2, the impact of repeated natural frequencies on the stability of PGTs has not been adequately investigated. Recognizing this gap in the existing literature, the present research aims to address this issue in its initial phase. In this work, a pure rotational model with three planet gears is utilized as the basis for the analysis. The research is primarily focused on identifying regions of instability within the system, taking into consideration the time-varying meshing stiffnesses between the gears. To achieve this, the multiple-scale method is employed as an analytical tool, allowing for a

thorough assessment of the system's stability. Additionally, the obtained results from this analytical approach are verified through numerical simulations based on Floquet theory. This analysis is crucial for ensuring the reliable and efficient operation of such systems, particularly in applications where stability is of utmost importance. The inclusion of time-varying meshing stiffnesses adds a realistic aspect to the analysis, as it accounts for the dynamic nature of the gear interactions.

Given the increasing size and load demands placed on PGTs, the ring gears in these systems are typically designed with thinner walls. As a consequence, they exhibit significant deflection when subjected to higher loads. In light of this phenomenon, in the second stage of this research, the focus shifts towards the investigation of ring vibrations. While there have been several works cited in subsections 2.4, it becomes apparent that the studies concerning the effects of boundary conditions are limited and primarily revolve around hinged or fixed rings. Since the accuracy of any model's analysis depends on the correct and appropriate handling of boundary conditions, it is of vital importance to study the effects of different boundary conditions. This research aims to address this gap by introducing a thorough model that can describe each support in a manner that encompasses all the aforementioned scenarios. A further deficiency in the current literature is the absence of a closed-form representation concerning the natural frequencies and mode shapes of a ring. Despite the extensive amount of work conducted in the aforementioned areas, there has been relatively little research on the response of a ring under general boundary conditions. Moreover, most of the existing studies have focused solely on Euler-Bernoulli rings and have relied on various numerical solutions. Therefore, one of the other objectives of this study is to address this gap by developing a

technique to express an analytical closed-form representation for a ring with any desired number of general elastic supports based on both Euler-Bernoulli and Timoshenko theories.

Within a PGT, the meshing force between the ring gear and planet gear is not fixed; rather, it moves along the circumference of the ring at the carrier's angular speed, resulting in a dynamic load excitation. This dissertation extensively examines the dynamics of the ring gear when subjected to such a moving meshing load and offers a theoretical analysis to provide valuable insights into the complex behavior of these systems. The findings of this study will contribute to a better understanding of ring gear dynamics in PGTs and assist in developing more precise models and design guidelines for such systems.

References

[1] E. Buckingham, Dynamic Loads on Gear Teeth: Report of the ASME Special Research Committee on the Strength of Gear Teeth, An Investigation Conducted at the Massachusetts Institute of Technology, Cambridge, Mass. American Society of Mechanical Engineers (1931).

[2] E. Buckingham, Analytical Mechanics of Gears, Angewandte Chemie International Edition, 6(11), 951–952. (1967).

[3] G.H. Marx, L.E. Cutter, Strength of gear system, ASME, Transactions of the American Society of Mechanical Engineers 37 (1915).

[4] L.J. Franklin, C.H. Smith, Effect of inaccuracies on strength of gears, ASME, Transactions of The American Society of Mechanical Engineers, 46 (1924).

[5] J. Lin, R.G. Parker, Analytical characterization of the unique properties of planetary gear free vibration, Journal of Vibration and Acoustics, Transactions of the ASME. 121 (1999). https://doi.org/10.1115/1.2893982.

[6] A. Kahraman, Natural Modes of Planetary Gear Trains, J Sound Vib. 173 (1994). https://doi.org/10.1006/jsvi.1994.1222.

[7] A. Kahraman, Planetary gear train dynamics, Journal of Mechanical Design, Transactions of the ASME. 116 (1994). https://doi.org/10.1115/1.2919441.

[8] X. Wu, R.G. Parker, Modal properties of planetary gears with an elastic continuum ring gear, Journal of Applied Mechanics, Transactions ASME. 75 (2008). https://doi.org/10.1115/1.2839892.

[9] P. Sondkar, A. Kahraman, A dynamic model of a double-helical planetary gear set, Mech Mach Theory. 70 (2013). https://doi.org/10.1016/j.mechmachtheory.2013.07.005.

[10] J. Wei, A. Zhang, D. Qin, T.C. Lim, R. Shu, X. Lin, F. Meng, A coupling dynamics analysis method for a multistage planetary gear system, Mech Mach Theory. 110 (2017). https://doi.org/10.1016/j.mechmachtheory.2016.12.007.

[11] W. Kim, J.Y. Lee, J. Chung, Dynamic analysis for a planetary gear with time-varying pressure angles and contact ratios. Journal of Sound and Vibration (2012), 331(4), pp.883-901.

[12] C. Wang, X. Zhang, J. Zhou, H. Wang, Y. Shen, S. Qiao, Calculation Method of Dynamic Stress of Flexible Ring Gear and Dynamic Characteristics Analysis of Thin-Walled Ring Gear of Planetary Gear Train, Journal of Vibration Engineering and Technologies. 9 (2021). https://doi.org/10.1007/s42417-020-00259-6.

[13] M. Benton, A. Seireg, Simulation of resonances and instability conditions in pinion-gear systems, Journal of Mechanical Design, Transactions of the ASME. 100 (1978). https://doi.org/10.1115/1.3453888.

[14] J. Lin, R.G. Parker, Mesh stiffness variation instabilities in two-stage gear systems, Journal of Vibration and Acoustics, Transactions of the ASME. 124 (2002). https://doi.org/10.1115/1.1424889.

[15] W.A. Tuplin, Dynamic Loads on Gear Teeth. Machine Design (1953) 25 p.203.

[16] J. Zeman, Dynamische Zusatzkrafter in Zahnbradgetrieben. Zeitschrift des Vereines Deutscher Ingiere, (1957) 9 p.244.

[17] A. Kahraman, Load sharing characteristics of planetary transmissions, Mech Mach Theory. 29 (1994). https://doi.org/10.1016/0094-114X(94)90006-X.

[18] Y. Jianming, L. Dai, Survey of dynamics of planetary gear trains, Intl Journal of Materials and Structural Integrity. 1 (2008). https://doi.org/10.1504/IJMSI.2008.019614.

[19] C.G. Cooley, R.G. Parker, A review of planetary and epicyclic gear dynamics and vibrations research, Appl Mech Rev. 66 (2014). https://doi.org/10.1115/1.4027812.

[20] H. Nevzat Özgüven, D.R. Houser, Mathematical models used in gear dynamics—A review, J Sound Vib. 121 (1988). https://doi.org/10.1016/S0022-460X(88)80365-1.

[21] K. Sato, O. Kamada, N. Takatsu, Dynamical distinctive phenomena in gear system, Bulletin of the JSME. 22 (1979). https://doi.org/10.1299/jsme1958.22.1840.

[22] A. Kahraman, G.W. Blankenship, Experiments on nonlinear dynamic behavior of an oscillator with clearance and periodically time-varying parameters, Journal of Applied Mechanics, 64, 217-226 (1997) https://doi.org/10.1115/1.2787276.

[23] J.S. Wu, F.T. Lin, H.J. Shaw, Free in-plane vibration analysis of a curved beam (arch) with arbitrary various concentrated elements, Appl Math Model. 37 (2013). https://doi.org/10.1016/j.apm.2013.02.029.

[24] J.S. Wu, Analytical and Numerical Methods for Vibration Analyses, 2015. https://doi.org/10.1002/9781119137207.

[25] F.M.L. Amirouche, N.H. Shareef, M. Xie, Dynamic analysis of flexible gear trains/transmissions: An automated approach, Journal of Applied Mechanics, Transactions ASME. 59 (1992). https://doi.org/10.1115/1.2894069.

[26] F.M. Amirouche, Computational methods in multibody dynamics. NASA STI/Recon Technical Report A, (1992) 94, p.12550.

[27] J.T. Kahnamouei, J. Yang, Development and verification of a computationally efficient stochastically linearized planetary gear train model with ring elasticity, Mech Mach Theory. 155 (2021). https://doi.org/10.1016/j.mechmachtheory.2020.104061.

[28] G. Schmidt, Application of the theory of nonlinear oscillations: Interaction of self-excited forced and parametrically excited vibrations, 9th International Conference on Non-linear Oscillations, 3 Kiev, Naukowa Dumka (1984).

[29] J. Taheri Kahnamouei, J. Yang, Random vibration analysis of thin-walled elastic rings under multiple moving loads, Proc Inst Mech Eng C J Mech Eng Sci. 236 (2022). https://doi.org/10.1177/0954406221996408.

[30] J. Lin, R.G. Parker, Structured vibration characteristics of planetary gears with unequally spaced planets, J Sound Vib. 233 (2000). https://doi.org/10.1006/jsvi.1999.2581.

[31] J. Lin, R.G. Parker, Sensitivity of planetary gear natural frequencies and vibration modes to model parameters, J Sound Vib. 228 (1999). https://doi.org/10.1006/jsvi.1999.2398.

[32] R.G. Parker, X. Wu, Parametric instability of planetary gears having elastic continuum ring gears, Journal of Vibration and Acoustics, Transactions of the ASME. 134 (2012). https://doi.org/10.1115/1.4005836.

[33] Y. Jianming, D. Liming, Parametric resonance analysis on simplified Planetary Gear Trains, International Journal of Materials and Product Technology. 31 (2008). https://doi.org/10.1504/IJMPT.2008.018025.

[34] A.H. Nayfeh, D.T. Mook, Nonlinear Oscillations, John Wiley & Sons, New York, New York (1979). https://doi.org/10.1177/058310248101300507.

[35] F.C.L. Fu, S. Nemat-Nasser, Response and stability of linear dynamic systems with many degrees of freedom subjected to nonconservative and harmonic forces, J of Applied Mechanics, Transactions ASME. 42 (1975). https://doi.org/10.1115/1.3423599.

[36] Tezak, E. G., Nayfeh, A. H., & Mook, D. T. (1982). Parametrically excited non-linear multi degree-of-freedom systems with repeated natural frequencies. Journal of Sound and Vibration, 85(4). https://doi.org/10.1016/0022-460X(82)90316-9.

[37] X. Qiu, Q. Han, F. Chu, Dynamic modeling and analysis of the planetary gear under pitching base motion, Int J Mech Sci. 141 (2018). https://doi.org/10.1016/j.ijmecsci.2018.03.037.

[38] S. Yimin, L. Xuzhong, L. Hongwu, C. Yan, X. Jin, Efficiency analysis of planetary gear train under ring gear deformation, in: International Conference on Control, Automation and Systems, 2018.

[39] R. Hoppe, The bending vibration of circular ring, Crelle Journal of Mathematics 73, pp. 158-168 (1871).

[40] S.S. Rao, Vib. of continuous systems, (2019). https://doi.org/10.1002/9781119424284.

[41] X. Wu, R.G. Parker, Vibration of rings on a general elastic foundation, J Sound Vib. 295 (2006). https://doi.org/10.1016/j.jsv.2006.01.007.

[42] D. Zhang, S. Wang, J. Liu, Analytical prediction for free response of rotationally ring-shaped periodic structures, Journal of Vibration and Acoustics, Transactions of the ASME. 136 (2014). https://doi.org/10.1115/1.4027630.

[43] T.E. Lang, Vibration of Thin Circular Rings. Part II. Modal Functions and Eigenvalues of Constrained Semicircular Rings, Jet Propulsion Lab., California Inst. of Tech. Pasadena, USA (1962). Document ID: 19630006566.

[44] R.E. Ball, Dynamic Analysis of Rings by Finite Differences, Journal of the Engineering Mechanics Division. 93 (1967). https://doi.org/10.1061/jmcea3.0000823.

[45] A.E.H. Love, A treatise on the mathematical theory of elasticity. Cambridge University Press 4th edition (2013). ISBN-13: 978-1107618091

[46] P. Chidamparam, A.W. Leissa, Vibrations of planar curved beams, rings, and arches, Appl Mech Rev. 46 (1993). https://doi.org/10.1115/1.3120374.

[47] J. Henrych, The Dynamics of Arches and Frames. Amsterdam, Elsevier Sci Co., (1981).

[48] P. Chidamparam, A.W. Leissa, Influence of centerline extensibility on the in-plane free vibrations of loaded circular arches, J Sound Vib. 183 (1995). https://doi.org/10.1006/jsvi.1995.0286.

[49] P. Chidamparam, Free Vibration and Buckling of Curved Beams Subjected to Distributed Loads, Ph.D. Dissertation, The Ohio State University, USA (1993).

[50] S.S. Rao, Effects of transverse shear and rotatory inertia on the coupled twist-bending vibrations of circular rings. Journal of Sound and Vibration, (1971) 16(4), pp.551-566.

[51] J.D. Yau, C.M. Wu, Dynamic response of a horizontally curved beam subjected to vertical and horizontal moving loads, J Sound Vib. 242 (2001). https://doi.org/10.1006/jsvi.2000.3355.

[52] B.K. Lee, S.J. Oh, K.K. Park, Free vibrations of shear deformable circular curved beams resting on elastic foundations, International Journal of Structural Stability and Dynamics. 02 (2002). https://doi.org/10.1142/s0219455402000440.

[53] R. Davis, R.D. Henshell, G.B. Warburton, Curved beam finite elements for coupled bending and torsional vibration, Earthq Eng Struct Dyn. 1 (1972). https://doi.org/10.1002/eqe.4290010205.

[54] R. Dams, R.D. Henshell, G.B. Warburton, Discussion of Effects of transverse shear and rotatory inertia on the coupled twist-bending vibrations of circular rings, J Sound Vib. 21 (1972). https://doi.org/10.1016/0022-460X(72)90910-8.

[55] C.H. Yoo, J.P. Fehrenbach, Natural frequencies of curved girders. Journal of the Engineering Mechanics Division (1981), 107(2), pp.339-354.

[56] A.O. Lebeck, J.S. Knowlton, A finite element for the three-dimensional deformation of a circular ring, Int J Num Meth. 21 (1985). https://doi.org/10.1002/nme.1620210304.

[57] S. Xue, I. Howard, Vibration response from the planetary gear with flexible ring gear, International J of Powertrains. 8 (2019). https://doi.org/10.1504/ijpt.2019.10019419.

[58] J. Liu, R. Pang, S. Ding, X. Li, Vibration analysis of a planetary gear with the flexible ring and planet bearing fault, Measurement (Lond). 165 (2020). https://doi.org/10.1016/j.measurement.2020.108100.

[59] A. Kahraman, A.A. Kharazi, M. Umrani, A deformable body dynamic analysis of planetary gears with thin rims, J Sound Vib. 262 (2003). https://doi.org/10.1016/S0022-460X(03)00122-6.

[60] A. Kahraman, S. Vijayakar, Effect of internal gear flexibility on the quasi-static behavior of a planetary gear set, Journal of Mechanical Design, Transactions of the ASME. 123 (2001). https://doi.org/10.1115/1.1371477.

[61] H. Ge, Y. Shen, Y. Zhu, Y. Xiong, B. Yuan, Z. Fang, Simulation and experimental test of load-sharing behavior of planetary gear train with flexible ring gear, Journal of Mechanical Science and Technology. 35 (2021). https://doi.org/10.1007/s12206-021-1006-1.

[62] Y. Hu, D. Talbot, A. Kahraman, A Gear Load Distribution Model for a Planetary Gear Set with a Flexible Ring Gear Having External Splines, Journal of Mechanical Design, Transactions of the ASME. 141 (2019). https://doi.org/10.1115/1.4041583.

[63] L.L. Philipson, On the Role of Extension in the Flexural Vibrations of Rings, J Appl Mech. 23 (1956). https://doi.org/10.1115/1.4011337.

[64] S.S. Rao, V. Sundararajan, In-plane flexural vibrations of circular rings, Journal of Applied Mechanics, Transactions ASME. 36 (1964). https://doi.org/10.1115/1.3564726.

[65] A.S. Veletsos, W.J Austin, C.A. Lopes Pereira, S.J. Wung, Free in-plane vibrations of circular arches, Journal of Engineering Mechanics: ASCE, (1972) 98: 311-29, https://doi.org/10.1061/JMCEA3.0001585.

[66] C.A.L. Pereia, Free Vibration of Circular Arches, Master Thesis, Rice University, Houston, Texas, USA (1968).

[67] S.J. Wung, Vibration of Hinged Circular Arches, Master Thesis, Rice University, Houston, Texas, USA (1967).

[68] N.M. Auciello, M.A. De Rosa, Free vibrations of circular arches: A review, J Sound Vib. 176 (1994). https://doi.org/10.1006/jsvi.1994.1388.

[69] R.R. Archer, Small vibrations of thin incomplete circular rings, Int J Mech Sci. 1 (1960). https://doi.org/10.1016/0020-7403(60)90029-1.

[70] A.K. Mallik, D.J. Mead, Free vibration of thin circular rings on periodic radial supports, J Sound Vib. 54 (1977). https://doi.org/10.1016/0022-460X(77)90402-3.

[71] K.B. Sahay, V. Sundararajan, Vibration of a stiffened ring considered as a cyclic structure, J Sound Vib. 22 (1972). https://doi.org/10.1016/0022-460X(72)90456-7.

[72] T.J. McDaniel, Dynamics of circular periodic structures, J Aircr. 8 (1971). https://doi.org/10.2514/3.44245.

[73] V.R. Murthy, N.C. Nigam, Dynamic characteristics of stiffened rings by transfer matrix approach, J Sound Vib. 39 (1975). https://doi.org/10.1016/S0022-460X(75)80222-7.

[74] K. Singh, B.L. Dhoopar, Free vibration of circular rings on radial supports, J Sound Vib. 65 (1979). https://doi.org/10.1016/0022-460X(79)90521-2.

[75] A.E. Zakrzhevskii, V.F. Tkachenko, V.S. Khoroshilov, Natural modes and frequencies of in-plane vibrations of a fixed elastic ring, International Applied Mechanics. 46 (2011). https://doi.org/10.1007/s10778-011-0436-3.

[76] M. Eisenberger, E. Efraim, In-plane vibrations of shear deformable curved beams, Int J Numer Methods Eng. 52 (2001). https://doi.org/10.1002/nme.246.

[77] S.P. Timoshenko, On the correction for shear of the differential equation for transverse vibrations of prismatic bars, London, Edinburgh, and Dublin Philosophical Magazine and Journal of Science. 41 (1921). https://doi.org/10.1080/14786442108636264.

[78] S.P. Timoshenko, X. On the transverse vibrations of bars of uniform cross-section , The London, Edinburgh, and Dublin Philosophical Magazine and Journal of Science. 43 (1922). https://doi.org/10.1080/14786442208633855.

[79] S.M. Han, H. Benaroya, T. Wei, Dynamics of transversely vibrating beams using four engineering theories, J Sound Vib. 225 (1999). https://doi.org/10.1006/jsvi.1999.2257.

[80] F.M. Detinko, Free vibration of a thick ring on multiple supports, Int J Eng Sci. 27 (1989). https://doi.org/10.1016/0020-7225(89)90066-9.

[81] J. Wolf, Natural frequencies of circular arches, ASCE J Struct Div. 97 (1971). https://doi.org/10.1061/jsdeag.0002999.

[82] W.J. Austin, A.S. Veletsos, Free vibration of arches flexible in shear, ASCE J Eng Mech Div. 99 (1973). https://doi.org/10.1061/jmcea3.0001782.

[83] T. Irie, G. Yamada, K. Tanaka, Natural frequencies of in-plane vibration of arcs, Journal of Applied Mechanics, Transactions ASME. 50 (1983). https://doi.org/10.1115/1.3167058.

[84] M.S. Issa, T.M. Wang, B.T. Hsiao, Extensional vibrations of continuous circular curved beams with rotary inertia and shear deformation, I: Free vibration, J Sound Vib. 114 (1987). https://doi.org/10.1016/S0022-460X(87)80155-4.

[85] C.S. Huang, Y.P. Tseng, C.L. Hung, An accurate solution for the responses of circular curved beams subjected to a moving load, Int J Numer Methods Eng. 48 (2000).

[86] Z. Zhao, S. Wang, J. Xiu, Parametric vibration of an elastic structure with stationary and rotating rings subjected to traveling loads, J Sound Vib. 358 (2015). https://doi.org/10.1016/j.jsv.2015.07.025.

[87] A. V. Metrikine, M. V. Tochilin, Steady-state vibrations of an elastic ring under a moving load, J Sound Vib. 232 (2000). https://doi.org/10.1006/jsvi.1999.2756.

[88] G.L. Forbes, R.B. Randall, Resonance phenomena of an elastic ring under a moving load, J Sound Vib. 318 (2008). https://doi.org/10.1016/j.jsv.2008.05.021.

[89] T.P. Joseph, J.F. Wilson, Vibrations of curved spans for mass transit, ASCE J Eng Mech Div. 106 (1980). https://doi.org/10.1061/jmcea3.0002583.

[90] K.H. Chu, S.G. Pinjarkar, Analysis of horizontally curved box girder bridges, ASCE J Struct Div. 97 (1971). https://doi.org/10.1061/jsdeag.0003021.

[91] R.O. Rabizadeh, S. Shore, Dynamic Analysis of curved box-girder bridges, ASCE J Struct Div. 101 (1975). https://doi.org/10.1061/jsdeag.0004162.

[92] D. Huang, T. Lo Wang, M. Shahawy, Vibration of horizontally curved box girder bridges due to vehicles, Comput Struct. 68 (1998). https://doi.org/10.1016/S0045-7949(98)00065-0.

[93] S.V. Canchi, R.G. Parker, Parametric instability of a circular ring subjected to moving springs, J Sound Vib. 293 (2006). https://doi.org/10.1016/j.jsv.2005.10.007.

[94] S.V. Canchi, R.G. Parker, Effect of ring-planet mesh phasing and contact ratio on the parametric instabilities of a planetary gear ring, Journal of Mechanical Design, Transactions of the ASME. 130 (2008). https://doi.org/10.1115/1.2803716.

[95] H. Ouyang, Moving-load dynamic problems: A tutorial (with a brief overview), Mech Syst Signal Process. 25 (2011). https://doi.org/10.1016/j.ymssp.2010.12.010.

[96] L. Frýba, Vibration of solids and structures under moving loads (Vol. 1). Springer science & business media (2013) DOI: 10.1007/978-94-011-9685-7.

CHAPTER 3

Stability Analysis of a Planetary Gear Train Having Repeated Natural Frequencies

Authorship Statement.

A version of this chapter was published in the Journal of Vibration Testing and System Dynamics in 2021 (https://doi.org/10.5890/jvtsd.2021.12.001). As the first author, I developed the algorithm and performed numerical validation. Dr. James Yang, as the supervisor, proposed the concept, and reviewed the manuscript. Below is a concise summary outlining the declaration that identifies the authors of this work and describes the authors' contributions.

Javad Abedini: *Investigation, Methodology, Software, Writing - Original Draft, Review & Editing, Validation.*
James Yang: *Conceptualization, Methodology, Visualization, Supervision.*

Abstract – Planetary gear trains (PGTs) are widely used in various engineering fields, including automotive, aerospace, and wind turbines, among others. In dynamic models of geared systems, the time-varying meshing stiffness can lead to parametric resonances or instability. This chapter investigates the instability caused by the time-varying meshing stiffness in PGTs, specifically the instabilities associated with repeated natural frequencies. The current approach yields a conservative solution for the unstable regions, resulting in a slightly larger unstable region than that reported in previous literature. The multiple-scale method is used in this analysis which is numerically validated with Floquet theory.

Keywords: Planetary gear train; Multiple-scale method; Instability; Repeated natural frequencies

3.1 Introduction

Planetary gear trains (PGTs) have several advantages, making them widely used in various applications such as automobiles, helicopters, and wind turbines, among others. Since the late 1970s, extensive research has been conducted on various aspects of PGT dynamics. Hidaka et al. [1,2] investigated the dynamics of a 2K-H type PGT and presented their findings in a series of seven reports from 1976 to 1979. August and Kasuba [3] developed a lumped parameter model and simulated the dynamic response using a computer. The effectiveness of the lumped-parameter model was later studied by Ambarisha et al. [4]. Research on PGT dynamics has continued to flourish since the 1990s.

In gear dynamics, the time-varying stiffness of the gear meshing presents an internal excitation to the system, leading to highly complex resonances and instabilities [5, 6]. Yang et al. [7] used the frequency domain approach and analyzed the vibration behavior of a planetary gearbox with the focus on parametrically excited vibrations and instabilities resulting from time-varying gear mesh stiffness. Mo et al. [8] investigated the load sharing of a herringbone planetary gear train with flexible support and floating sun gear. They developed a mathematical model considering factors like mesh stiffness, tooth profile, and bearing flexibility. The study revealed that the gear train's load distribution is influenced by the support structure and floating sun gear flexibility. Wang et al. [9] studied the effect of planet mesh phasing on the vibration of planetary geartrains. Their results indicated that mesh phasing could effectively suppress many potential resonances, irrespective of any mass or stiffness matrix model. Neufond et al. [10] employed an iterative spectral method to investigate the impacts of multi-mesh excitations on a planetary geartrain, considering the internal excitations. The presence of multiple gear meshes in a PGT amplifies the complexity of these instabilities. Several researchers have investigated the instability of PGTs caused by the time-varying meshing stiffness [11-13]. In a PGT, the multiple planet gears are generally symmetrically arranged around the sun gear, resulting in repeated natural frequencies. Kahraman [11] conducted a concise and insightful analysis of this phenomenon using a pure rotational lumped parameter model. Subsequently, Lin and Parker conducted more comprehensive studies using refined models [12-14]. Some works also considered the effects of the flexibility of the ring gear [15] and viscous damping [16]. Gao et al. [17] analyzed parametric vibrations and instabilities induced in an elliptical gear pair, and evaluated the effects of fundamental parameters on vibration instability by calculating geometric parameters and time-variant mesh stiffness. Qiu

et al. [18] analyzed the instability boundaries for primary and combination instabilities, and examined the effects of speed fluctuations and damping on parametric instability. Beinstingel et al. [19] analyzed the vibration behavior of a planetary gearbox, focusing on parametrically excited vibrations and instabilities resulting from time-varying gear mesh stiffness. Due to space limitations, this chapter does not aim to provide a comprehensive review of all research works. Interested readers are directed to two review papers [20,21].

Despite the aforementioned research efforts and a few additional articles [22-25], the influence of repeated natural frequencies on the instability of a PGT has not been adequately addressed. In light of this, the objective of this chapter is to analyze the instability related to the repeated natural frequencies. For simplicity, a pure rotational model with three planets is used. However, the results obtained from this model can be extended to more complex configurations.

The current chapter is structured as follows: In Section 3.2, a pure rotational model is employed to derive the equation of motion, and closed-form representation of the natural frequencies of the system are presented. In Section 3.3, the method of multiple scales is elucidated. This method is then utilized in Section 3.4 to obtain the instability zones related to the repeated frequencies. In Section 3.5, the Floquet theory is introduced to validate the analytical results acquired from the multiple-scale method. Section 3.6 furnishes a case study based on the parameters of a PGT used in wind turbines. The instability zones attained from this chapter are then compared with the ones from published papers. Finally, Section 3.7 summarizes the conclusions, while Section 3.8 explores future work.

3.2 Dynamic Model and Natural Frequencies

3.2.1 Dynamic Model

A pure rotational lumped-parameter model, as shown in Fig. 3.1, is used in this chapter. It consists of a sun gear, a planet carrier, a ring gear, and three planet gears. The ring is assumed stationary, and the gear meshes between the sun and planets (s-p mesh) and between the ring and planets (r-p mesh) are modeled as elastic springs, represented as k_{sp} and k_{rp}, respectively.

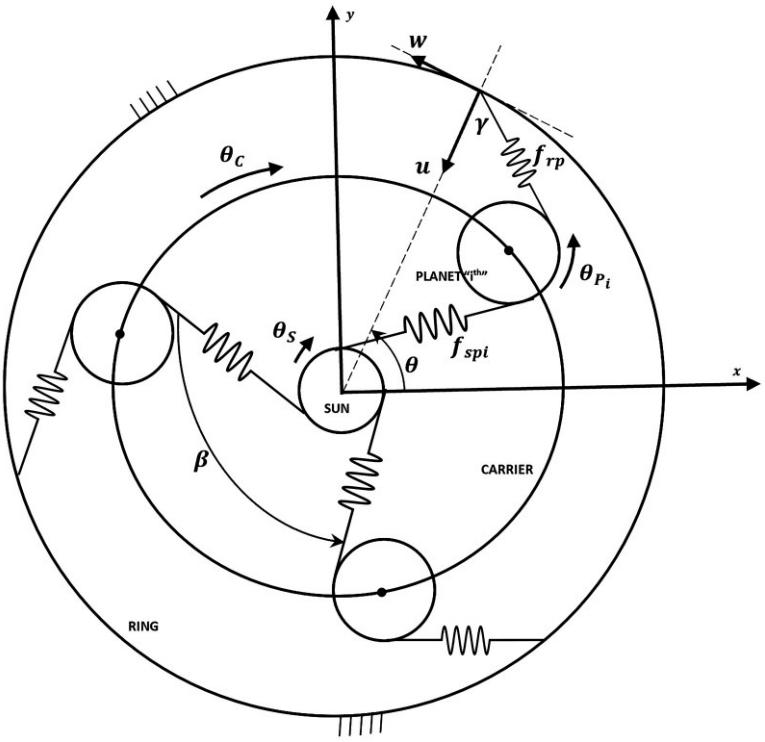

Fig. 3.1 *Planetary Gear Train*

The positive directions of rotation for the sun, planets, and carrier are depicted in Fig. 3.1. The generalized coordinates are chosen as the linear elastic deformation along the line of action of each gear mesh. Therefore, the total generalized coordinates can be represented in

matrix form as $\{U\} = \{u_c \quad u_s \quad u_p^1 \quad u_p^2 \quad u_p^3\}^T$ where $u_c = \mathrm{r_c}\theta_c$, $u_s = \mathrm{r_s}\theta_s$, and $u_p^i = \mathrm{r_p}\theta_p^3$. The equation of motion for each element can be written as follows:

The sun gear:

$$\frac{\mathrm{J_s}}{\mathrm{r_s}^2}\ddot{u}_s - \sum_{i=1}^{3} k_{sp}^i \cos\gamma\, u_c + \sum_{i=1}^{3} k_{sp}^i u_s + \sum_{i=1}^{3} k_{sp}^i u_p^i = 0 \tag{3.1}$$

The carrier:

$$\begin{aligned}\left(\frac{\mathrm{J_c}}{\mathrm{r_c}^2} + 3\mathrm{m_p}\right)\ddot{u}_c + \sum_{i=1}^{3}\left(k_{sp}^i + k_{rp}^i\right)\cos\gamma\, u_c - \sum_{i=1}^{3} k_{sp}^i \cos\gamma\, u_s \\ + \sum_{i=1}^{3}\left(k_{rp}^i - k_{sp}^i\right)\cos\gamma\, u_p^i = 0\end{aligned} \tag{3.2}$$

The planet gears:

$$\frac{\mathrm{J_p}}{\mathrm{r_p}^2}u_p^i + \left(k_{rp}^i - k_{sp}^i\right)u_c + k_{sp}^i u_s + \left(k_{sp}^i + k_{rp}^i\right)u_p^i = 0 \tag{3.3}$$

where $r_k(k = s, p, c)$ represents the radius of the base circles. The subscripts s, p, and c represent the sun, the planet, and the carrier, respectively. In addition, the superscript i (i=1 to 3) is used to differentiate between the three planets for variables associated with the planets. k_{rp}^i and k_{sp}^i are the meshing stiffness of the i^{th} r-p and s-p mesh, respectively. The parameter J denotes the moment of inertia for each part, and its subscripts follow the same convention as defined above. The parameter γ signifies the pressure angle of the gear pair.

The rigid body motion of the system can be eliminated by fixing the mechanism at each time instant. Mathematically, this can be achieved by removing the corresponding row and

column of matrices [M] and [K] that are associated with the ring gear. The dynamic equation for the free vibrations of the system, which consists of Eqs. (3.1) thorough (3.3), can be expressed in the following matrix form:

$$[\mathrm{M}]\{\ddot{U}\} + [K]\{U\} = 0 \tag{3.4}$$

where [M] and [K] are the mass and stiffness matrices, respectively. Assuming that all three planets possess equivalent moment of inertia $\mathrm{J_p}$ and base circle $\mathrm{r_p}$, then the matrices [M] and [K] in Eq. (3.4) can be simplified and expressed as follows:

$$[\mathrm{M}] = diag\,[\mathrm{M}_0 \quad \mathrm{M}_1 \quad \mathrm{M}_2 \quad \mathrm{M}_2 \quad \mathrm{M}_2] \tag{3.5}$$

$$[K] = \begin{bmatrix} K_{11} & K_{12} & K_{13} & K_{14} & K_{15} \\ K_{21} & K_{22} & K_{23} & K_{24} & K_{25} \\ K_{31} & K_{32} & K_{33} & 0 & 0 \\ K_{41} & K_{42} & 0 & K_{44} & 0 \\ K_{51} & K_{52} & 0 & 0 & K_{55} \end{bmatrix} \tag{3.6}$$

The entries for matrices expressed in Eqs. (3.5) and (3.6) are presented in Appendix A:

3.2.2 Natural Frequencies

The stiffness of each gear mesh, denoted as k_{sp}^{i} and k_{rp}^{i} is time-varying due to the changing number of teeth in contact, which can be represented as Fourier series. If only the first harmonic is considered, the stiffness matrix can be approximated as follows:

$$[K] \approx [K]_m + [K]_v(\mathrm{t}) \tag{3.7}$$

where $[K]_m$ and $[K]_v(\mathrm{t})$ represent the constant and time-varying parts of the stiffness matrix, respectively. Eigenvalue analysis can be conducted based on the $[M]$ and $[K]_m$ matrices to

obtain the natural frequencies. In order to simplify the problem, it is assumed that the carrier rotates at a constant speed. This simplification is achieved by eliminating the corresponding row and column for the carrier. As a result, Eq. (3.4) can be expressed in a modified form as:

$$\begin{bmatrix} \mathrm{M}_1 & 0 & 0 & 0 \\ 0 & \mathrm{M}_2 & 0 & 0 \\ 0 & 0 & \mathrm{M}_2 & 0 \\ 0 & 0 & 0 & \mathrm{M}_2 \end{bmatrix} \begin{Bmatrix} \ddot{u}_s \\ \ddot{u}_p^1 \\ \ddot{u}_p^2 \\ \ddot{u}_p^3 \end{Bmatrix} + \begin{bmatrix} K_{22} & K_{23} & K_{24} & K_{25} \\ K_{32} & K_{33} & 0 & 0 \\ K_{42} & 0 & K_{44} & 0 \\ K_{52} & 0 & 0 & K_{55} \end{bmatrix} \begin{Bmatrix} u_s \\ u_p^1 \\ u_p^2 \\ u_p^3 \end{Bmatrix} = 0 \tag{3.8}$$

Closed-form equations for natural frequencies of such system can be derived by solving:

$$|[K]_m - \omega^2[\mathrm{M}]| = 0 \tag{3.9}$$

Plugging the corresponding entries from Appendix A into Eq. (3.9) will result in:

$$\omega_1 = \omega_2 = \sqrt{\frac{k_{sp} + k_{rp}}{\mathrm{J_p}/{\mathrm{r_p}}^2}} \tag{3.10}$$

$$\omega_3 = \sqrt{\frac{\Re - \sqrt{\Re^2 - 12k_{sp}k_{rp}(\mathrm{J_s}/{\mathrm{r_s}}^2)(\mathrm{J_p}/{\mathrm{r_p}}^2)}}{2(\mathrm{J_s}/{\mathrm{r_s}}^2)(\mathrm{J_p}/{\mathrm{r_p}}^2)}} \tag{3.11}$$

$$\omega_4 = \sqrt{\frac{\Re + \sqrt{\Re^2 - 12k_{sp}k_{rp}(\mathrm{J_s}/{\mathrm{r_s}}^2)(\mathrm{J_p}/{\mathrm{r_p}}^2)}}{2(\mathrm{J_s}/{\mathrm{r_s}}^2)(\mathrm{J_p}/{\mathrm{r_p}}^2)}} \tag{3.12}$$

where:

$$\Re = (k_{sp} + k_{rp})(\mathrm{J_s}/{\mathrm{r_s}}^2) + 3k_{sp}(\mathrm{J_p}/{\mathrm{r_p}}^2) \tag{3.13}$$

Eq. (3.10) indicates the repetition of two of the natural frequencies in this case. According to linear algebra, the equations of motion can be transformed into the following

forms through the transformation of $\{U\} = [\emptyset]\{X\}$ where $[\emptyset]$ is a matrix consisting of the eigenvectors of Eq. (3.4). Matrix $[\emptyset]$ can be obtained by solving the eigenvalue problem of $\left[[K]_m - \Lambda_r[\mathrm{M}]\right]\{U\} = 0$ where Λ_r are the eigenvalues of the system. Substituting $\{U\} = [\emptyset]\{X\}$ into Eq. (3.8) will result in:

$$[\mathrm{M}][\emptyset]\begin{Bmatrix}\ddot{x}_1\\ \ddot{x}_2\\ \ddot{x}_3\\ \ddot{x}_4\end{Bmatrix} + [K]_m[\emptyset]\begin{Bmatrix}x_1\\ x_2\\ x_3\\ x_4\end{Bmatrix} + [K]_v[\emptyset]\begin{Bmatrix}x_1\\ x_2\\ x_3\\ x_4\end{Bmatrix} = 0 \tag{3.14}$$

By pre-producting the transpose of vibration modes in Eq. (3.14), the following equation can be obtained.

$$[\emptyset]^T[\mathrm{M}][\emptyset]\begin{Bmatrix}\ddot{x}_1\\ \ddot{x}_2\\ \ddot{x}_3\\ \ddot{x}_4\end{Bmatrix} + [\emptyset]^T[K]_m[\emptyset]\begin{Bmatrix}x_1\\ x_2\\ x_3\\ x_4\end{Bmatrix} + [\emptyset]^T[K]_v[\emptyset]\begin{Bmatrix}x_1\\ x_2\\ x_3\\ x_4\end{Bmatrix} = 0 \tag{3.15}$$

The vibration mode shapes $\emptyset_n$ is normalized. Thus, $[\emptyset]^T[\mathrm{M}][\emptyset] = \mathrm{I}$. Due to the degenerated frequencies in the system, the transformed stiffness matrix $[\emptyset]^T[K]_m[\emptyset]$ will be changed into a non-diagonal Jordan canonical form. $[K]_v(\mathrm{t})$ can be considered as $\cos(\Omega \mathrm{t})$ where Ω is the gear meshing frequency. Expanding Eq. (3.15), and introducing a small parameter ϵ to differentiate the time-varying stiffness from the main constant part will result in:

$$\ddot{\mathrm{x}}_1 + \omega_1{}^2\,\mathrm{x}_1 + \epsilon\sum_{\mathrm{i}=1}^{4}\mathrm{f}_{1\mathrm{i}}\cos(\Omega \mathrm{t})\,\mathrm{x}_\mathrm{i} = 0 \tag{3.16}$$

$$\ddot{\mathrm{x}}_2 + \omega_1{}^2\,\mathrm{x}_2 + \mathrm{x}_1 + \epsilon\sum_{\mathrm{i}=1}^{4}\mathrm{f}_{2\mathrm{i}}\cos(\Omega \mathrm{t})\,\mathrm{x}_\mathrm{i} = 0 \tag{3.17}$$

$$\ddot{\mathrm{x}}_3 + \omega_3{}^2\,\mathrm{x}_3 + \epsilon\sum_{\mathrm{i}=1}^{4}\mathrm{f}_{3\mathrm{i}}\cos(\Omega \mathrm{t})\,\mathrm{x}_\mathrm{i} = 0 \tag{3.18}$$

$$\ddot{\mathrm{x}}_4 + \omega_4{}^2\,\mathrm{x}_4 + \epsilon\sum_{\mathrm{i}=1}^{4}\mathrm{f}_{4\mathrm{i}}\cos(\Omega \mathrm{t})\,\mathrm{x}_\mathrm{i} = 0 \tag{3.19}$$

3.3 Multiple-Scale Method

The multiple-scale method is commonly used to obtain the response of nonlinear systems. It approximates the solution using a combination of different time scales. In order to solve Eq. (3.8), the multiple-scale method is used in this chapter. Generally, this method applies to weak nonlinear problems. One of the limitation of this method is that it may not always be accurate for systems with highly nonlinear behavior, as it relies on the assumption that the perturbation parameter is small [26]. The other limitation is that it does not provide an accurate solution for rapidly changing parameters [27]. In the case of analyzing planetary geartrain vibrations, using the multiple-scale method is acceptable since the system does not have large nonlinearities. Thus, the inaccuracy coming from the limitations of this method is insignificant.

3.4 Instability Analysis

In the absence of parametric excitation, the system is unstable due to the presence of a secular term in x_2. The introduction of parametric excitation can stabilize the motion. However, the assumption of x_2 being much larger than x_1 is expected, while no information is available about x_3 and x_4. Thus, x_1 through x_4 can be formulated, as follows:

$$x_1 = V_1 \tag{3.20}$$

$$x_2 = \epsilon^{-\lambda_2} V_2 \tag{3.21}$$

$$x_3 = \epsilon^{-\lambda_3} V_3 \tag{3.22}$$

$$x_4 = \epsilon^{-\lambda_4} V_4 \tag{3.23}$$

where λ_i $(i = 2,3,4)$ are constants to be determined. Furthermore, the time scales can be formulated by following the procedures outlined in the method of multiple scales [28].

$$\mathrm{T}_0 = \mathrm{t} \tag{3.24}$$

$$T_1 = \epsilon^{\lambda_1} t \tag{3.25}$$

$$T_2 = \epsilon^{2\lambda_1} t \tag{3.26}$$

where λ_1 is another constant to be determined. The responses i.e., V_i $(i = 1\ to\ 4)$ can be expanded into the following form.

$$V_i(t,\epsilon) = V_{i0}(T_0, T_1, \dots) + \epsilon^{\lambda_1} V_{i1}(T_0, T_1, \dots) + \epsilon^{2\lambda_1} V_{i2}(T_0, T_1, \dots) + \cdots \tag{3.27}$$

The time derivatives in the multiple-scale method can be represented as follows:

$$\frac{d}{dt} = D_0 + \epsilon^{\lambda_1} D_1 + \epsilon^{2\lambda_1} D_2 + \cdots \tag{3.28}$$

$$\frac{d^2}{dt^2} = {D_0}^2 + 2\epsilon^{\lambda_1} D_0 D_1 + \epsilon^{2\lambda_1}({D_1}^2 + 2D_0 D_2) + \cdots \tag{3.29}$$

where D_0 and D_1 are the first and second partial derivative operators with respect to T_0 and T_1, respectively. By substituting Eqs. (3.20) through (3.29) into Eqs. (3.16) through (3.19), the following four equations can be obtained.

$$\begin{aligned}&(D_0^2 V_{10} + {\omega_1}^2 V_{10}) + \left[\epsilon^{\lambda_1}(D_0^2 V_{11} + {\omega_1}^2 V_{11} + 2D_0 D_1 V_{10}) + \epsilon^{2\lambda_1}(D_0^2 V_{12} + {\omega_1}^2 V_{12} + \right.\\ &\left. 2D_0 D_2 V_{10} + D_1^2 V_{10} + 2D_0 D_1 V_{11})\right] + \cos(\Omega t)\left[(\varepsilon f_{11} V_{10} + \varepsilon^{1-\lambda_2} f_{12} V_{20} + \right.\\ &\left. \varepsilon^{1-\lambda_3} f_{13} V_{30} + \varepsilon^{1-\lambda_4} f_{14} V_{40} + \varepsilon^{1+\lambda_1} f_{11} V_{11} + \varepsilon^{1+\lambda_1-\lambda_2} f_{12} V_{21} + \varepsilon^{1+\lambda_1-\lambda_3} f_{13} V_{31} + \right.\\ &\left. \varepsilon^{1+\lambda_1-\lambda_4} f_{14} V_{41}) + \cdots\right] = 0\end{aligned} \tag{3.30}$$

$$(D_0^2V_{20} + \omega_1^2V_{20}) + \left[\epsilon^{\lambda_1}(D_0^2V_{21} + \omega_1^2V_{21} + 2D_0D_1V_{20})\right] + \left[\epsilon^{2\lambda_1}(D_0^2V_{22} + \omega_1^2V_{22} + 2D_0D_1V_{21} + D_1^2V_{20} + 2D_0D_2V_{20})\right] + \epsilon^{\lambda_2}V_{10} + \cos(\Omega t)\left[(\varepsilon^{1+\lambda_2}f_{21}V_{10} + \varepsilon f_{22}V_{20} + \varepsilon^{1+\lambda_2-\lambda_3}f_{23}V_{30} + \varepsilon^{1+\lambda_2-\lambda_4}f_{24}V_{40} + \varepsilon^{1+\lambda_1}f_{22}V_{21} + \varepsilon^{1+\lambda_1+\lambda_2-\lambda_3}f_{23}V_{31} + \varepsilon^{1+\lambda_1+\lambda_2-\lambda_4}f_{24}V_{41}) + \cdots\right] = 0 \quad (3.31)$$

$$(D_0^2V_{30} + \omega_3^2V_{30}) + \epsilon^{\lambda_1}(D_0^2V_{31} + \omega_3^2V_{31} + 2D_0D_1V_{30}) + \epsilon^{2\lambda_1}(D_0^2V_{32} + \omega_3^2V_{32} + 2D_0D_1V_{31} + D_1^2V_{30} + 2D_0D_2V_{30}) + \cos(\Omega t)\,(\varepsilon^{1+\lambda_3}f_{31}V_{10} + \varepsilon^{1-\lambda_2+\lambda_3}f_{32}V_{20} + \varepsilon f_{33}V_{30} + \varepsilon^{1+\lambda_3-\lambda_4}f_{34}V_{40} + \varepsilon^{1+\lambda_1-\lambda_2+\lambda_3}f_{32}V_{21} + \varepsilon^{1+\lambda_1}f_{33}V_{31} + \varepsilon^{1+\lambda_1+\lambda_3-\lambda_4}f_{34}V_{41}) + \cdots = 0 \quad (3.32)$$

$$(D_0^2V_{40} + \omega_4^2V_{40}) + \epsilon^{\lambda_1}(D_0^2V_{41} + \omega_4^2V_{41} + 2D_0D_1V_{40}) + \epsilon^{2\lambda_1}(D_0^2V_{42} + \omega_4^2V_{42} + 2D_0D_1V_{41} + D_1^2V_{40} + 2D_0D_2V_{40}) + \cos(\Omega t)\,(\varepsilon^{1+\lambda_4}f_{41}V_{10} + \varepsilon^{1-\lambda_2+\lambda_4}f_{42}V_{20} + \varepsilon^{1\pm+\lambda_4}f_{43}V_{30} + \epsilon f_{44}V_{40} + \varepsilon^{1+\lambda_1-\lambda_2+\lambda_3}f_{42}V_{21} + \varepsilon^{1+\lambda_1-\lambda_3+\lambda_4}f_{43}V_{31} + \varepsilon^{1+\lambda_1}f_{44}V_{41}) + \cdots = 0 \quad (3.33)$$

In the following, the focus is on the instability zones related to repeated natural frequencies. Specifically, this study examines two categories of resonance: repeated-repeated case of $\Omega \approx 2\,\omega_1$ and repeated-distinct case of $\Omega \approx \omega_1 + \omega_3$ or $\Omega \approx \omega_1 + \omega_4$. The resonances related to distinct-distinct cases of $\Omega \approx 2\,\omega_3$, $\Omega \approx 2\,\omega_4$, or $\Omega \approx \omega_3 + \omega_4$ are not discussed here as they have been explored in previous publications [13, 14].

3.4.1 Case of $\Omega \approx 2\,\omega_1$

To represent the closeness of Ω to $2\omega_1$, a detuning parameter σ and a to-be-determined constant λ_5 are introduced.

$$\Omega = 2(\omega_1 + \epsilon^{\lambda_5}\sigma) \tag{3.34}$$

To keep the interaction between x_1 and x_2, the effect of V_{20} in Eq. (3.30) i.e., $\varepsilon^{1-\lambda_2}$, and V_{10} in Eq. (3.31) i.e., ϵ^{λ_2} must be retained. Otherwise, x_1 would be unrelated from x_2. Moreover, these two terms must have the same scale. This process can be mathematically satisfied by equating the power of both terms into λ_1. Eq. (3.35) sets the scale of effect of V_{20} into $\lambda_1$and similarly, Eq. (3.36) sets the scale of effect of V_{10} into λ_1.

$$1 - \lambda_2 = \lambda_1 \tag{3.35}$$

$$\lambda_2 = \lambda_1 \tag{3.36}$$

Solving Eqs. (3.35) and (3.36) simultaneously gives:

$$\lambda_1 = \lambda_2 = 0.5 \tag{3.37}$$

Since x_3 and x_4 have no interaction with x_1 and x_2, the stability of the motion is independent of the values λ_3 and λ_4. Thus, it is accepted to set

$$\lambda_3 = \lambda_4 = 0 \tag{3.38}$$

Also, the resonance appears as the first perturbation terms of V_{i1}. Thus, λ_5 in Eq. (3.34) can take the same value as what it was calculated in Eq. (3.37):

$$\lambda_5 = \lambda_1 = 0.5 \tag{3.39}$$

To arrive at a concise form, it is possible to group the terms that contain equivalent powers of ϵ from Eqs. (3.30) through (3.33):

Order of ϵ^0:

$$D_0^2 V_{10} + \omega_1^2 V_{10} = 0 \tag{3.40}$$

$$D_0^2 V_{20} + \omega_1^2 V_{20} = 0 \tag{3.41}$$

$$D_0^2 V_{30} + \omega_3^2 V_{30} = 0 \tag{3.42}$$

$$D_0^2 V_{40} + \omega_4^2 V_{40} = 0 \tag{3.43}$$

Order of $\epsilon^{1/2}$:

$$D_0^2 V_{11} + \omega_1^2 V_{11} + 2 D_0 D_1 V_{10} + f_{12} V_{20} \cos(\Omega T_0) = 0 \tag{3.44}$$

$$D_0^2 V_{21} + \omega_1^2 V_{21} + 2 D_0 D_1 V_{20} + V_{10}(t) = 0 \tag{3.45}$$

$$D_0^2 V_{31} + \omega_3^2 V_{31} + 2 D_0 D_1 V_{30} + f_{32} V_{20} \cos(\Omega T_0) = 0 \tag{3.46}$$

$$D_0^2 V_{41} + \omega_4^2 V_{41} + 2 D_0 D_1 V_{40} + f_{42} V_{20} \cos(\Omega T_0) = 0 \tag{3.47}$$

The general solutions for Eqs. (3.40) through (3.43) can be expressed as:

$$V_{10} = A_1(T_1)\, e^{i\,\omega_1 T_0} + \bar{A}_1(T_1) e^{-i\omega_1 T_0} \tag{3.48}$$

$$V_{20} = A_2(T_1)\, e^{i\,\omega_1 T_0} + \bar{A}_2(T_1) e^{-i\omega_1 T_0} \tag{3.49}$$

$$V_{30} = A_3(T_1)\, e^{i\,\omega_3 T_0} + \bar{A}_3(T_1) e^{-i\omega_3 T_0} \tag{3.50}$$

$$V_{40} = A_4(T_1)\, e^{i\,\omega_4 T_0} + \bar{A}_4(T_1) e^{-i\omega_4 T_0} \tag{3.51}$$

Substituting Eqs. (3.48) and (3.49) into Eq. (3.44) will result in:

$$D_0^2\, V_{11} + \omega_1^2\, V_{11} + 2i\omega_1\left(A_1' e^{i\omega_1 T_0} + \bar{A}_1{}'\, e^{-i\omega_1 T_0}\right) + f_{12}\left[A_2(T_1)\, e^{i\,\omega_1 T_0} + \bar{A}_2(T_1) e^{-i\omega_1 T_0}\right]\cos(\Omega T_0) = 0 \tag{3.52}$$

where the overbars denote the complex conjugate and the prime represents the derivatives with respect to T_1. By using the trigonometrical properties and using the exponential representation for $\cos(\Omega T_0)$, and use of Eq. (3.34), the following equation can be obtained.

$$\cos(\Omega T_0) = \frac{e^{i\Omega T_0} + e^{-i\Omega T_0}}{2} = \frac{e^{2i(\omega_1 T_0 - \sigma T_1)} + e^{-2i(\omega_1 T_0 - \sigma T_1)}}{2} \tag{3.53}$$

Inserting Eq. (3.53) into Eq. (3.52) yields:

$$D_0^2\, V_{11} + \omega_1^2\, V_{11} + \left(2i\omega_1 A_1' + \frac{f_{12}}{2}\bar{A}_2\, e^{2i\sigma T_1}\right) e^{i\omega_1 T_0} = 0 \tag{3.54}$$

Similarly, Eqs. (3.48) through (3.51) can be plugged into Eqs. (3.45) through (3.47) and compose the following equations:

$$D_0^2\, V_{21} + \omega_1^2\, V_{21} + (2i\omega_1 A_2' + A_1)\, e^{i\omega_1 T_0} = 0 \tag{3.55}$$

$$D_0^2\, V_{31} + \omega_3^2\, V_{31} + 2i\omega_3 A_3'\, e^{i\omega_3 T_0} + f_{32} V_{20}\cos(\Omega T_0) = 0 \tag{3.56}$$

$$D_0^2\, V_{41} + \omega_4^2\, V_{41} + 2i\omega_4 A_4'\, e^{i\omega_1 T_0} + f_{42} V_{20}\cos(\Omega T_0) = 0 \tag{3.57}$$

To eliminate the secular terms in Eqs. (3.54) through (3.57), the following conditions should be met.

$$2i\omega_1 A_1' + \frac{f_{12}}{2}\bar{A}_2\, e^{2i\sigma T_1} = 0 \tag{3.58}$$

$$2i\omega_1 A_2' + A_1 = 0 \tag{3.59}$$

$$2i\omega_3 A_3' = 0 \tag{3.60}$$

$$2i\omega_4 A_4' = 0 \tag{3.61}$$

Clearly, there is only interaction between A_1 and A_2. From Eqs. (3.53) and (3.54), one can eliminate A_1, and get a second-order ODE as below:

$$4\omega_1^2 A_2'' + \frac{f_{12}}{2}\bar{A}_2\, e^{2i\sigma T_1} = 0 \tag{3.62}$$

Assuming:

$$A_2 = (A_2^R + iA_2^I)e^{i\,\sigma\, T_1} \tag{3.63}$$

The superscripts R and I in Eq. (3.63) represent the real and imaginary parts, respectively. Substituting this equation into Eq. (3.62) and separating the real and imaginary parts, gives:

$$4\omega_1^2[(A_2^R)'' - 2\sigma(A_2^I)' - \sigma^2 A_2^R] + \frac{f_{12}}{2}A_2^R = 0 \tag{3.64}$$

$$4\omega_1^2[(A_2^I)'' - 2\sigma(A_2^R)' - \sigma^2 A_2^I] + \frac{f_{12}}{2}A_2^I = 0 \tag{3.65}$$

These two second-order ODEs possess nontrivial solutions, which can be represented as $A_2^R = B_1\, e^{\eta T_1}$ and $A_2^I = B_2\, e^{\eta T_1}$. The requirement for the existence of a solution is given by:

$$\begin{vmatrix} \eta^2 - \sigma^2 + \dfrac{f_{12}}{8\omega_1^2} & -2\eta\sigma \\ -2\eta\sigma & \eta^2 - \sigma^2 - \dfrac{f_{12}}{8\omega_1^2} \end{vmatrix} = 0 \tag{3.66}$$

Solving Eq. (3.66) leads to:

$$\eta^2 = -\sigma^2 \pm \frac{f_{12}}{8\omega_1^2} \tag{3.67}$$

By setting $\eta = 0$, it is possible to differentiate between the stable and unstable regions. Consequently, by solving Eq. (3.67), one can derive the following:

$$\sigma = \pm \sqrt{\frac{f_{12}}{8\omega_1^2}} \tag{3.68}$$

Substituting Eq. (3.68) into Eq. (3.34) gives:

$$\Omega = 2\omega_1 \pm 2\epsilon^{1/2} \sqrt{\frac{f_{12}}{8\omega_1^2}} \tag{3.69}$$

Eq. (3.69) serves as the demarcation curve that distinguishes the stable and unstable regions originating from the point of $2\omega_1$. It delineates the boundaries that separate these two zones.

3.4.2 Cases of $\boldsymbol{\Omega \approx \omega_1 + \omega_3}$ and $\boldsymbol{\Omega \approx \omega_1 + \omega_4}$

When the value of Ω is in proximity to the summation of two distinct natural frequencies, such as $\Omega \approx \omega_1 + \omega_3$ or $\Omega \approx \omega_1 + \omega_4$, the system experiences resonance, as well. The approach to handling these two cases is identical. In this section, we will focus on the case of $\Omega \approx \omega_1 + \omega_3$. It should be noted that the same methodology can be employed for the case of $\Omega \approx \omega_1 + \omega_4$. Assuming:

$$\Omega = \omega_1 + \omega_3 + \epsilon^{\lambda_5}\sigma \tag{3.70}$$

To keep the interaction between x_1 and x_3, one should at least retain the term of V_{30} in Eq. (3.30), the terms of V_{10} in Eq. (3.31), and the term of V_{20} in Eq. (3.32). Thus, it can be obtained that:

$$1 - \lambda_3 = 2\lambda_1 \tag{3.71}$$

$$\lambda_2 = 2\lambda_1 \tag{3.72}$$

$$1 - \lambda_2 + \lambda_3 = 2\lambda_1 \tag{3.73}$$

Solving these equations simultaneously gives:

$$\lambda_1 = \frac{1}{3} \quad ; \quad \lambda_2 = \frac{2}{3} \quad ; \quad \lambda_3 = \frac{1}{3} \tag{3.74}$$

Equating the terms of the same power of ϵ yields:

Order of ϵ^0:

$$D_0^2 V_{10} + \omega_1^2 V_{10} = 0 \tag{3.75}$$

$$D_0^2 V_{20} + \omega_1^2 V_{20} = 0 \tag{3.76}$$

$$D_0^2 V_{30} + \omega_3^2 V_{30} = 0 \tag{3.77}$$

$$D_0^2 V_{40} + \omega_4^2 V_{40} = 0 \tag{3.78}$$

Order of $\epsilon^{1/3}$:

$$D_0^2 V_{11} + \omega_1^2 V_{11} + 2 D_0 D_1 V_{10} + f_{12} V_{20} \cos(\Omega T_0) = 0 \tag{3.79}$$

$$D_0^2 V_{21} + \omega_1^2 V_{21} + 2 D_0 D_1 V_{20} = 0 \tag{3.80}$$

$$D_0^2\, V_{31} + \omega_3^2\, V_{31} + 2\, D_0 D_1 V_{30} = 0 \tag{3.81}$$

$$D_0^2\, V_{41} + \omega_4^2\, V_{41} + 2\, D_0 D_1 V_{40} + f_{42} V_{20} \cos(\Omega T_0) = 0 \tag{3.82}$$

Order of $\epsilon^{2/3}$:

$$D_0^2\, V_{12} + \omega_1^2\, V_{12} + 2\, D_0 D_1 V_{11} + 2\, D_0 D_2 V_{10} + D_1^2\, V_{10} + (f_{13} V_{30} + f_{21} V_{21}) \cos(\Omega T_0) = 0 \tag{3.83}$$

$$D_0^2\, V_{22} + \omega_1^2\, V_{22} + 2\, D_0 D_1 V_{21} + 2\, D_0 D_2 V_{20} + D_1^2\, V_{20} + V_{10} = 0 \tag{3.84}$$

$$D_0^2\, V_{32} + \omega_3^2\, V_{32} + 2\, D_0 D_1 V_{31} + 2\, D_0 D_2 V_{30} + D_1^2\, V_{30} + f_{32} V_{20} \cos(\Omega T_0) = 0 \tag{3.85}$$

$$D_0^2\, V_{42} + \omega_4^2\, V_{42} + 2\, D_0 D_1 V_{41} + 2\, D_0 D_2 V_{40} + D_1^2\, V_{40} + f_{43} V_{30} \cos(\Omega T_0) + f_{42} V_{21} \cos(\Omega T_0) = 0 \tag{3.86}$$

The solutions of Eqs. (3.75) through (3.78) can be expressed as:

$$V_{10} = A_1(T_1, T_2)\, e^{i\,\omega_1 T_0} + cc \tag{3.87}$$

$$V_{20} = A_2(T_1, T_2)\, e^{i\,\omega_1 T_0} + cc \tag{3.88}$$

$$V_{30} = A_3(T_1, T_2)\, e^{i\,\omega_3 T_0} + cc \tag{3.89}$$

$$V_{40} = A_4(T_1, T_2)\, e^{i\,\omega_4 T_0} + cc \tag{3.90}$$

Substituting Eqs. (3.87) through (3.90) into Eqs. (3.79) through (3.82), and eliminating the secular terms, one can obtain:

$$D_1(A_j) = 0 \qquad (j = 1 - 4) \tag{3.91}$$

This means that the solution is not dependent on T_1. Thus, the resonance appears in the V_{i2}, and λ_5 can be set to $\lambda_5 = \frac{2}{3}$. In this part, only A_1 to A_3 are need to be considered. Hence, it can be assumed that:

$$A_j = \left(A_j^R + iA_j^I\right)e^{i\sigma T_2} \quad (j = 1 - 3) \tag{3.92}$$

The solution of Eqs. (3.79) through (3.81) can be written as follows:

$$V_{11} = \frac{f_{12}}{2}\left\{\frac{A_2\, e^{i(\Omega+\omega_1)T_0}}{\Omega\,(\Omega + 2\omega_1)} + \frac{\overline{A_2}\, e^{i(\Omega-\omega_1)t}}{\Omega\,(\Omega - 2\omega_1)}\right\}\left(A_j\right) = 0 \qquad (j = 1 - 4) \tag{3.93}$$

$$V_{21} = V_{31} = 0 \tag{3.94}$$

By substituting all these results into Eqs. (3.83) through (3.85), and eliminating the secular terms, the following equations can be derived:

$$2i\omega_1(A_1^R + i\, A_1^I)(i\sigma) + f_{13}(A_3^R - i\, A_3^I) = 0 \tag{3.95}$$

$$2i\omega_1(A_2^R + i\, A_2^I)(i\sigma) + (A_1^R + i\, A_1^I) = 0 \tag{3.96}$$

$$2i\omega_3(A_3^R + i\, A_3^I)(i\sigma) + f_{32}(A_2^R - i\, A_2^I) = 0 \tag{3.97}$$

The aforementioned set of Eqs. (3.95) through (3.97) can be partitioned into a pair of components, of a real and an imaginary part. To solve this, the following determinant must be set to zero:

$$\begin{vmatrix} -2\omega_1\sigma & 0 & f_{13} \\ 1 & -2\omega_1\sigma & 0 \\ 0 & f_{32} & -2\omega_3\sigma \end{vmatrix} = 0 \tag{3.98}$$

The solution of Eq. (3.98) is as follows:

$$\sigma = \pm \sqrt[3]{\frac{f_{13}\, f_{32}}{8\omega_1^2 \omega_3}} \tag{3.99}$$

Thus, the transition curves for this case $\Omega \approx \omega_1 + \omega_3$ can be represented as:

$$\Omega = \omega_1 + \omega_3 \pm \epsilon^{2/3} \left(\frac{f_{13}\, f_{32}}{8\omega_1^2 \omega_3} \right)^{1/3} \tag{3.100}$$

By employing the same methodology, it is not hard to obtain the transition curves that delineate the boundaries separating the stable and unstable regions stemming from the natural frequency of $\Omega \approx \omega_1 + \omega_4$.

$$\Omega = \omega_1 + \omega_4 \pm \epsilon^{2/3} \left(\frac{f_{14}\, f_{42}}{8\omega_1^2 \omega_4} \right)^{1/3} \tag{3.101}$$

3.5 Case Study

A PGT with three symmetrically arranged planet gears in a wind turbine is considered. Table 3.1 presents the parameters of this sample PGT. Following the procedure elaborated in section 3.1, the natural frequencies of this system can be determined by using Eqs. (3.10) through (3.12). Table 3.2 lists these natural frequencies. One set of repeated natural frequencies is observed for this system as expected.

Table 3.1. Parameters of a Planetary Gear Train

Parameter	Value	Unit
r_s	202×10^{-3}	m
r_{p_i}	329×10^{-3}	m
J_s	7.41	kg-m^2
J_p	12.34	kg-m^2
k_{sp}	3.55×10^7	N/m
k_{rp}	4.56×10^7	N/m

Table 3.2. Natural Frequencies of the Studied Planetary Gear Train

Frequency	Value	Unit
ω_1	843.45	rad/s
ω_2	843.45	rad/s
ω_3	465.88	rad/s
ω_4	1039.62	rad/s

The transition curves corresponding to this particular system are displayed separately in Figs. 3.2 through 3.4 to facilitate comparison. In instances of sum-type responses, where $\Omega \approx 2\omega_1$, Eq. (3.69) is employed to generate the instability zone plot. Similarly, for situations with distinct-repeated natural frequencies, Eqs. (3.100) and (3.101) are utilized to construct the instability zone plot. Due to the considerably high natural frequencies of PGTs utilized in wind turbines, the unstable regions are relatively narrow. The stars in each figure represent the unstable conditions derived from the Floquet theory. This method is explained in Section 3.6.

The numerical outcomes generated from the Floquet theory serve to corroborate the analytical results obtained through the method implemented in this study.

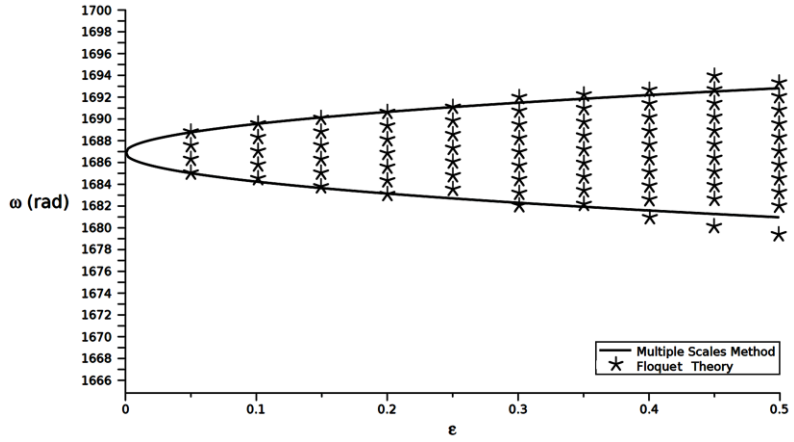

Fig. 3.2 *Instability region for the repeated-repeated mode when* $\Omega \approx 2\omega_1$

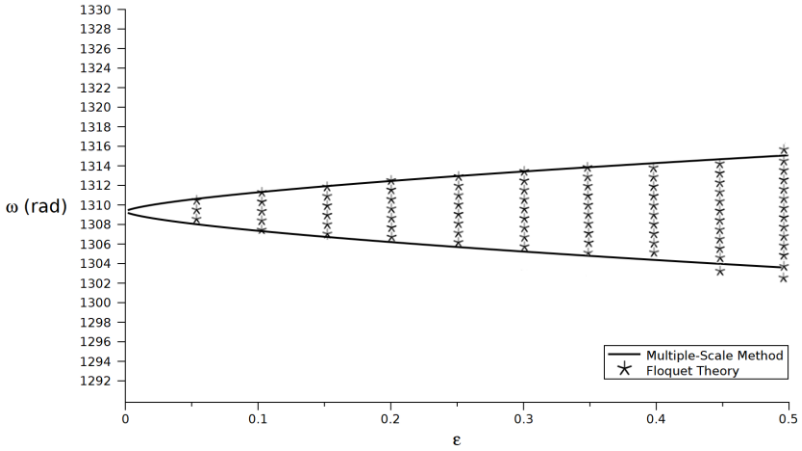

Fig. 3.3 *Instability region for the distinct-repeated mode when* $\Omega \approx \omega_1 + \omega_3$

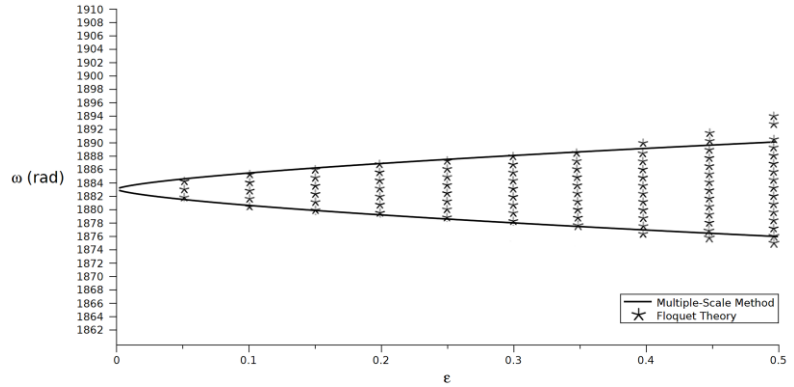

Fig. 3.4 *Instability region for the distinct-repeated mode when* $\Omega \approx \omega_1 + \omega_4$

The magnitude of the mesh frequency has a linear relationship with the f_{ij}(i,j=1-4) coefficients that appear in Eqs. (3.30) and (3.31) for the repeated-repeated modes, and in Eqs. (3.32) and (3.33) for the distinct-repeated modes.

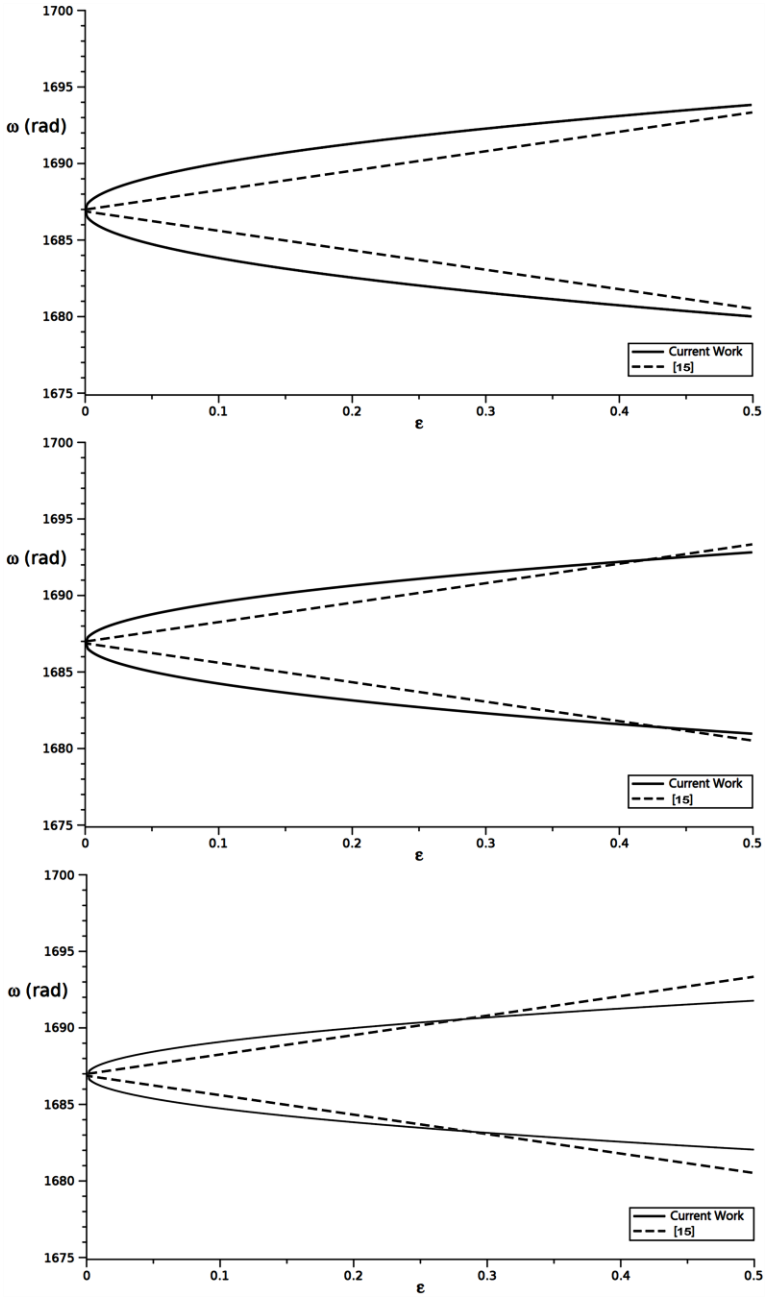

Fig. 3.5 *Comparison between transition curves for the repeated-repeated natural frequencies for different magnitudes when top: 0.1f_{12}, middle: f_{12}, bottom: 10f_{12}*

To further verify the results, the results obtained from this method are compared to the results from the published work [16], as shown in Figs 3.5 and 3.6. When the magnitude of the mesh frequency is much smaller than the non-linear magnitude, the solutions from both methods cover almost the same region. However, for very small or large f_{13} and f_{32}, there is a noticeable difference between the regions. The reason for this is that the power of the ϵ-term is unified in [16], which is different from the results from the current work.

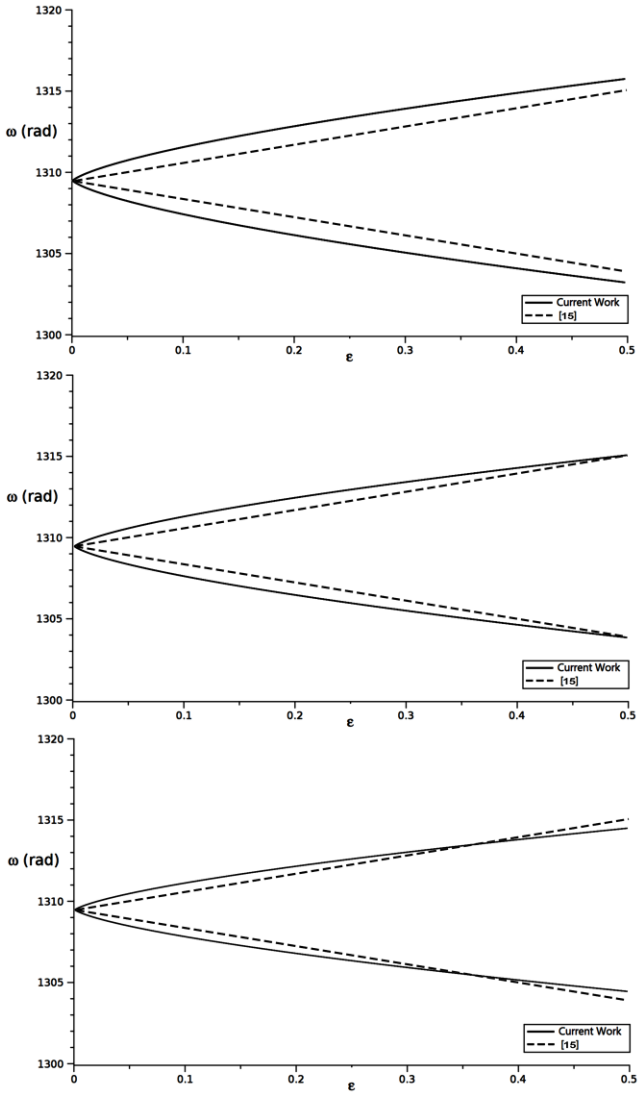

Fig. 3.6 *Comparison between transition curves for the repeated-distinct natural frequencies for different magnitudes when top: $0.1f_{13}$, middle: f_{13}, bottom: $10f_{13}$*

When analyzing the behavior of a system near its thresholds, it can be challenging to distinguish between stable and unstable behavior by simply comparing the plotted responses of two candid points. Floquet theory offers a powerful means of overcoming this challenge by providing mathematical expressions that reveal the behavior of the system at each point.

For researchers and scientists studying systems near their thresholds, this information is essential in gaining a deeper understanding of the system's behavior, facilitating the development of effective control strategies, and making accurate predictions. Furthermore, for cases located within the region and far enough from the separating lines, the instability growth of the responses is fast.

3.6 Floquet Theory

The Floquet theory is used to verify the above analysis. Eqs. (3.16) through (3.19) are second-order linear homogenous equations, and each of them possesses two linearly independent solutions denoted by $x_q(t)$ and $x_r(t)$ which satisfy any initial conditions considered. If $x_i(t)$ is a solution of, for instance Eq. (3.16), then, $x_i(t + \mathrm{T}_P)$ is also a solution; where T_P is the period of the equation. Hence, $x_i(t + \mathrm{T}_P)$ must be linearly dependent on $x_q(t)$ and $x_r(t)$. This relationship can be shown mathematically as follows:

$$\begin{cases} x_q(t + \mathrm{T}_P) = B_{qq}\, x_q(t) + B_{qr}\, x_r(t) \\ x_r(t + \mathrm{T}_P) = B_{rq}\, x_q(t) + B_{rr}\, x_r(t) \end{cases} \tag{3.102}$$

Once $x_q(t)$ and $x_r(t)$ are known, the coefficients B_{qr} can be uniquely determined after applying the boundary conditions, and results can be represented in matrix formations. Each of Eqs. (3.16) through (3.19) can be alternatively presented in matrix form as follows:

$$[\ddot{x}_n]_{4\times1} + [g_n(t)]_{4\times4}[x_n]_{4\times1} = 0 \tag{3.103}$$

where $g_n(t)$ is periodic with the period of T_P. By changing the variable such as

$$\begin{bmatrix} y_1 \\ y_2 \\ y_3 \\ y_4 \\ y_5 \\ y_6 \\ y_7 \\ y_8 \end{bmatrix} = \begin{bmatrix} x_1 \\ \dot{x}_1 \\ x_2 \\ \dot{x}_2 \\ x_3 \\ \dot{x}_3 \\ x_4 \\ \dot{x}_4 \end{bmatrix} \tag{3.104}$$

Once these solutions are obtained, their values and first derivatives can be calculated at a specific point in time. Based on these values and derivatives, it is possible to calculate the characteristic exponents [28]. This method offers a reliable way to determine the characteristic exponents of Eqs. (3.16) through (3.19), Using the values and first derivates of these solutions at $t=T_P$, one can calculate the discriminant ∇ [28]:

$$\nabla = \frac{1}{2}\left(x_q(T_P) + \dot{x}_r(T_P)\right) \tag{3.105}$$

In the next step, for each set, the following κ_i's can be calculated based on ∇, as follows:

$$\kappa_1 = \nabla + \sqrt{\nabla^2 - 1} \quad , \quad \kappa_2 = \nabla - \sqrt{\nabla^2 - 1} \tag{3.106}$$

These values need to be used to derive $\gamma_i = \frac{1}{\pi}(\ln \kappa_i)$. Thus, for each pair of K/M values and ϵ, the aforementioned procedure needs to be repeated. If any of the κ_i's absolute value is

greater than unity, the solution will become unbounded over time, and these specific points are marked with stars in Figs. 3.2 – 3.5. This phenomenon is demonstrated in Eq. (3.107).

$$\begin{cases} \text{Stable} & if \quad |\kappa_i| < 1 \\ \text{Borderline} & if \quad |\kappa_i| = 1 \\ \text{Unstable} & if \quad |\kappa_i| > 1 \end{cases} \tag{3.107}$$

3.7 Summary and Conclusion

This analysis focuses on a PGT with three planet gears, where pure rotational motion is assumed for all components. The multiple-scale method is employed to simplify the governing equations and eliminate secular terms from the responses, resulting in the stability regions of the system. The system is found to exhibit two different behaviors depending on the scenario, which are categorized as:

- Repeated-repeated mode.
- Distinct-repeated mode

In both cases, the unstable regions expand with increasing nonlinearity. However, the growth power in the latter case is slightly larger than in the first case, as deduced by examining the power of the ϵ-parameter in Eqs. (3.69) and (3.100). From Figs. 3.5 and 3.6, it can be deduced that the current method is conservative for a typical PGT, as the unstable region is slightly larger. This difference is mainly due to considering the off-diagonal terms that exist in the Jordan canonical matrix. The main conclusions of this work can be summarized as follows:

- The study concludes that when a PGT consists of three or more planet gears, some of the natural frequencies of the system will degenerate, resulting in possible parametric instabilities. These instabilities can be classified as repeated-repeated and distinct-repeated. The closed-form expressions for presenting the instability regions for each of the above scenarios are evaluated using the multiple-scale method and modal analysis to simplify the Jordan canonical matrix of the system.

- When the mesh frequency is close to the summation of two repeated natural frequencies, the separation curves take the form of parabolic functions with a power of ½, and the distinction between stable and unstable regions is not represented by lines. This is a novelty in the previous literature where it has considered lines.

- Repeating natural frequencies in the system results in slightly different behavior between the distinct-repeated and distinct-distinct modes, as compared to the case without repeated frequencies.

- The multiple-scale and perturbation techniques used in this study provide consistent results that can help to clarify previous disputed studies in this area, making it a valuable contribution to the field of mechanical engineering.

3.8 Future Work

In this study, the scenario analyzed was limited to repeated frequencies of order 2. To expand on this research, it is recommended to investigate cases with higher order where one or more natural frequencies are repeated more than two times. Additionally, it would be advantageous to examine the influence of viscous damping on the stabilization of the system.

References

[1] Hidaka, T., Terauchi, Y., Dynamic Behavior of Planetary Gear: 1st Report Load Distribution in Planetary Gear, Bulletin of JSME. 19 (1976). https://doi.org/10.1299/jsme1958.19.690.

[2] Hidaka, T., Terauchi, Y., & Nagamura, K. (1979). Dynamic behavior of planetary gear - 7th report, influence of the thickness of the ring gear. bulletin of the JSME, 22(170). https://doi.org/10.1299/jsme1958.22.1142.

[3] August, R., & Kasuba, R. (1986). Torsional vibrations and dynamic loads in a basic planetary gear system. Journal of Vibration and Acoustics, Transactions of the ASME, 108(3), https://doi.org/10.1115/1.3269349.

[4] Ambarisha, V. K., & Parker, R. G. (2007). Nonlinear dynamics of planetary gears using analytical and finite element models. Journal of Sound and Vibration, 302(3). https://doi.org/10.1016/j.jsv.2006.11.028

[5] Benton, M., & Seireg, A. (1978). Simulation of resonances and instability conditions in pinion-gear systems. Journal of Mechanical Design, Transactions of the ASME, 100(1). https://doi.org/10.1115/1.3453888.

[6] Lin, J., & Parker, R. G. (2002). Mesh stiffness variation instabilities in two-stage gear systems. Journal of Vibration and Acoustics, Transactions of the ASME, 124(1). https://doi.org/10.1115/1.1424889.

[7] J. Yang, R. Zhu, H.P. Lee, M. Li, X. Yin, Experimental and numerical dynamic analysis of marine herringbone planetary gearbox supported by journal bearings, J Sound Vib. 545 (2023). https://doi.org/10.1016/j.jsv.2022.117426.

[8] M. Shuai, Z. Ting, J. Guo-guang, C. Xiao-lin, G. Han-jun, Analytical investigation on load sharing characteristics of herringbone planetary gear train with flexible support and floating sun gear, Mech Mach Theory. 144 (2020). https://doi.org/10.1016/j.mechmachtheory.2019.103670.

[9] C. Wang, B. Dong, R.G. Parker, Impact of planet mesh phasing on the vibration of three-dimensional planetary/epicyclic gears, Mech Mach Theory. 164 (2021). https://doi.org/10.1016/j.mechmachtheory.2021.104422.

[10] J. Neufond, E. Denimal, E. Rigaud, J. Perret-Liaudet, A. Carbonelli, Whining noise computation of a planetary gear set induced by the multi-mesh excitations, Proc Inst Mech Eng C J Mech Eng Sci. 233 (2019). https://doi.org/10.1177/0954406219853313.

[11] Kahraman, A. (1994). Planetary gear train dynamics. Journal of Mechanical Design, Transactions of the ASME, 116(3). https://doi.org/10.1115/1.2919441.

[12] Lin, J., & Parker, R. G. (1999a). Analytical characterization of the unique properties of planetary gear free vibration. Journal of Vibration and Acoustics, Transactions of the ASME, 121(3). https://doi.org/10.1115/1.2893982.

[13] Lin, J., & Parker, R. G. (2000). Structured vibration characteristics of planetary gears with unequally spaced planets. In Journal of Sound and Vibration (Vol. 233, Issue 5). https://doi.org/10.1006/jsvi.1999.2581.

[14] Lin, J., & Parker, R. G. (1999b). Sensitivity of planetary gear natural frequencies and vibration modes to model parameters. Journal of Sound and Vibration, 228(1). https://doi.org/10.1006/jsvi.1999.2398.

[15] Parker, R. G., & Wu, X. (2012). Parametric instability of planetary gears having elastic continuum ring gears. Journal of Vibration and Acoustics, Transactions of the ASME, 134(4). https://doi.org/10.1115/1.4005836.

[16] Jianming, Y., & Liming, D. (2008). Parametric resonance analysis on simplified Planetary Gear Trains. International Journal of Materials and Product Technology, 31(2–4). https://doi.org/10.1504/IJMPT.2008.018025.

[17] N. Gao, C. Meesap, S. Wang, D. Zhang, Parametric vibrations and instabilities of an elliptical gear pair, JVC Journal of Vibration and Control. 26 (2020). https://doi.org/10.1177/1077546320902543.

[18] X. Qiu, Q. Han, F. Chu, Investigation of Parametric Instability of the Planetary Gear under Speed Fluctuations, Shock and Vibration. 2017 (2017). https://doi.org/10.1155/2017/6851903.

[19] A. Beinstingel, R.G. Parker, S. Marburg, Experimental measurement and numerical computation of parametric instabilities in a planetary gearbox, J Sound Vib. 536 (2022). https://doi.org/10.1016/j.jsv.2022.117160.

[20] Jianming, Y., & Dai, L. (2008). Survey of dynamics of planetary gear trains. International Journal of Materials and Structural Integrity, 1(4). https://doi.org/10.1504/IJMSI.2008.019614.

[21] Cooley, C. G., & Parker, R. G. (2014). A review of planetary and epicyclic gear dynamics and vibrations research. In Applied Mechanics Reviews (Vol. 66, Issue 4). https://doi.org/10.1115/1.4027812.

[22] A.H. Nayfeh and D.T. Mook (1979), Nonlinear Oscillations: John Wiley & Sons, New York, Shock and Vibration Digest, 13(5). https://doi.org/10.1177/058310248101300507.

[23] Fu, F. C. L., & Nemat-Nasser, S. (1975). Response and stability of linear dynamic systems with many degrees of freedom subjected to nonconservative and harmonic forces. J. Applied Mechanics, Transactions ASME, 42(2). https://doi.org/10.1115/1.3423599.

[24] Tezak, E. G., Nayfeh, A. H., & Mook, D. T. (1982). Parametrically excited non-linear multi degree-of-freedom systems with repeated natural frequencies. Journal of Sound and Vibration, 85(4). https://doi.org/10.1016/0022-460X(82)90316-9.

[25] J. Yang, P. Yang, Random Vibration and Dynamic Analysis of a Planetary Gear Train in a Wind Turbine. Shock and Vibration (2016). https://doi.org/10.1155/2016/6292953.

[26] R.E. O'Malley, Jr., Introduction to Perturbation Methods (M. H. Holmes), SIAM Review. 38 (1996). https://doi.org/10.1137/1038098.

[27] V.I. Arnold, Mathematical Methods of Classical Mechanics, 2012, DOI: 10.1007/978-1-4757-6051-9.

[28] A.H. Nayfeh, (2011). Introduction to perturbation techniques. John Wiley & Sons, ISBN 9780471310134

CHAPTER 4

Free Vibration Characteristics of a Thin-Walled Ring Under Different Boundary Conditions

Authorship Statement.

A version of this chapter was published in the Canadian Society of Mechanical Engineers (CSME) congress in Prince Edward Island in 2020 (https://doi.org/10.32393/csme.2020.1164). As the first author, I developed the algorithm and performed numerical validation. Dr. James Yang, as the supervisor, proposed the concept, and reviewed the manuscript. Below is a concise summary outlining the declaration that identifies the authors of this work and describes the authors' contributions.

Javad Abedini: *Investigation, Methodology, Software, Writing - Original Draft, Review & Editing, Validation.*

James Yang: *Conceptualization, Methodology, Visualization, Supervision.*

Abstract – In this chapter, an analytical approach is employed to investigate the natural frequencies of a thin-walled ring with various boundary conditions. The analytical method utilized in this research involves solving the eigenvalue problem associated with the governing differential equations of the system. Subsequently, the obtained analytical solutions are compared to numerical solutions obtained through simulations conducted in the Abaqus software package. This study's findings reveal a strong correlation between the natural frequencies of the system and the boundary conditions. Notably, the fixed supports condition leads to significantly higher natural frequencies in comparison to the hinged supports condition. This observation is consistently supported by both the analytical and Finite Element Method (FEM) approaches, highlighting their mutual agreement.

Keywords: Free Vibration; Mode Shape; Natural Frequency; Euler-Bernoulli Beam; Ring Vibration.

4.1 Introduction

Thin-walled rings find extensive application in diverse engineering systems, such as automotive, helicopters, and wind turbine systems. Notably, one crucial application lies in planetary gear trains, where the ring gear is typically classified as thin-walled. In these systems, the inherent vibrational behavior of the ring plays a pivotal role in shaping the overall dynamics

of the entire system. Extensive research has been conducted on the free vibration of rings, and several studies have been dedicated to this topic [1-8]. However, the majority of these investigations have focused on the behavior of free, pinned, and fixed rings, along with the development of closed-form equations [9-11].

The vibration behavior of thin-walled rings has been the subject of extensive research over the years. One particularly noteworthy study was undertaken by Rao [2], who thoroughly examined the free vibration of unconstrained thin-walled rings. Wu and Parker [3] applied perturbation and Galerkin methods on a ring supported by an elastic foundation. Their analysis extensively explored the dynamic response of the ring under various loading and boundary conditions. Moreover, Zhang et al. [4] conducted an investigation into the influence of rotation speed and mass distribution on the vibrational behavior of the ring. In a more recent study, Rao et al. [12] focused on determining the natural frequencies and associated mode shapes of a ring that is rigidly supported in the radial direction, employing a differential equation formulation. They meticulously analyzed the vibrational behavior of the ring under diverse loading and boundary conditions. Their study provided valuable insights into the vibration characteristics of thin-walled rings and can aid in the design and optimization of ring-shaped structures. Sahay et al. [13] addressed the same issue but adopted a distinct method, presenting a solution specifically tailored for scenarios involving a significant number of radial supports. In a separate line of investigation, multiple researchers [9, 14-15] utilized the transfer matrix method to obtain more precise outcomes concerning the natural frequencies and modes of a ring supported by numerous radial supports. However, it should be noted that this method neglects certain mode shapes, as it assumes that the overall vibrational mode of the entire ring can be determined by considering the behavior of one studied segment for all other segments.

This assumption is only valid for a specific set of boundary conditions. Malik et al. [16] utilized the wave approach to determine the natural frequencies of a ring by assuming it to be an endless periodic structure and calculating the propagation constants. On the other hand, Zakrzhevskii et al. [17] employed a numerical method to solve a boundary-value problem (BVP) for an elastic ring fixed at a specific point. However, neither of these studies was able to provide a concise closed-form expression for the mode shapes of a ring with different types of radial supports.

This chapter aims to fill a knowledge gap by investigating the free vibration of a ring under different support conditions, including hinged and fixed supports. In prior research, the problem was examined through numerical techniques or analytical approaches that were limited to specific ranges of support numbers. In contrast, this study introduces an analytical method capable of addressing the problem for a ring structure, regardless of the number of supports it possesses.

The following is the organizational structure of this chapter. Section 4.2 introduces the in-plane vibrational equations. Sections 4.3 and 4.4 outline the discussion of mode shapes and boundary conditions for various supports. A case study is presented in Section 4.5. Section 4.6 explains the Abaqus simulation, and finally, Section 4.7 draws the conclusions.

4.2 Dynamic Model

Fig. 4.1 depicts a thin-walled ring represented by its centerline. To simplify the governing equations, it is assumed that the rigidity of the ring, EI, is constant, and both rotary

inertia and shear deformation effects are ignored. The ring is supported by n supports, as illustrated below:

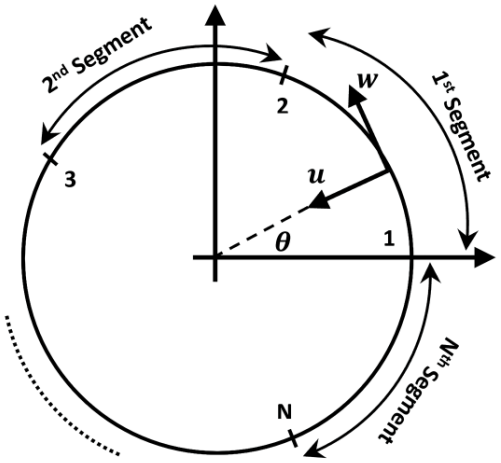

Fig. 4.1 *A thin-walled ring and the location of each support*

4.2.1. System Equations

To obtain the governing equations, a typical element located at an arbitrary position θ is selected. The forces and moments acting on this element can be expressed as functions of the deformation components. By disregarding the negligible higher-order terms, one can derive the equilibrium equations in three axes of tangential displacement w, radial displacement u, and the rotation of the cross-section φ.

$$\frac{\partial Q}{\partial \theta} + N = \rho \mathrm{AR}\, \ddot{u} \tag{4.1}$$

$$\frac{\partial N}{\partial \theta} - Q = \rho \mathrm{AR}\, \ddot{w} \tag{4.2}$$

$$\frac{\partial M}{\partial \theta} + \mathrm{R}Q = \rho \mathrm{IR}\, \ddot{\varphi} \tag{4.3}$$

Where R is the radius of the ring centerline, ρ is the mass density, A is the cross-sectional area, and I is the moment of inertia of the area A about the axis perpendicular to the middle plane of the ring and passing through the centroid. The normal force N is considered positive when in tension, the shear force Q is considered positive when acting in a radially inward direction on a positive face, and the in-plane bending moment M is considered positive when it tends to reduce the curvature of the ring. In addition, the relationships between the displacement functions can be expressed as follows:

$$\varphi = \frac{1}{\mathrm{R}}\left(\frac{\partial u}{\partial \theta} + w\right) \tag{4.4}$$

$$N = \frac{\mathrm{EA}}{\mathrm{R}}\left(\frac{\partial w}{\partial \theta} - u\right) - \frac{M}{\mathrm{R}} \tag{4.5}$$

$$M = \frac{\mathrm{EI}}{\mathrm{R}}\left(\frac{\partial \varphi}{\partial \theta}\right) \tag{4.6}$$

By substituting Eq. (4.4) into Eq. (4.6), a new relationship can be derived, as shown in Eq. (4.7).

$$M = \frac{\mathrm{EI}}{\mathrm{R}^2}\left(\frac{\partial^2 u}{\partial \theta^2} + \frac{\partial w}{\partial \theta}\right) \tag{4.7}$$

The strain ε can be represented in relation to the radial and tangential displacements in the following manner [2].

$$\varepsilon = \frac{1}{R}\left(\frac{\partial w}{\partial \theta} - u + \frac{x}{R}\frac{\partial}{\partial \theta}\left(w + \frac{\partial u}{\partial \theta}\right)\right) \tag{4.8}$$

where x is the distance from the ring centerline. Given the assumption that the centerline remains unstretched, it can be said that ε=0 for the centerline. By neglecting the effects of small product terms in Eq. (4.8), the tangential and radial displacements can be related as follows:

$$u = \frac{\partial w}{\partial \theta} \tag{4.9}$$

Eq. (4.9) is referred to as the inextensibility condition.

The in-plane flexural classical vibration equation for a thin-walled ring can be obtained by combining Eqs. (4.1)-(4.5), (4.7), and (4.9) into a single equation, which is given as follows:

$$\frac{\partial^6 w(\theta,t)}{\partial \theta^6} + 2\frac{\partial^4 w(\theta,t)}{\partial \theta^4} + \frac{\partial^2 w(\theta,t)}{\partial \theta^2} + \frac{\mathrm{R}^4 \rho\, \mathrm{A}}{\mathrm{E\, I}} \frac{\partial^2}{\partial t^2}\left(\frac{\partial^2 w(\theta,t)}{\partial \theta^2} - w(\theta,t)\right) = 0 \tag{4.10}$$

By applying the form presented in Eq. (4.11) to separate the variables, the overall solution can be expressed as the product of a mode shape function *Ψ(θ)* and a time-varying harmonic function *q(t)*, as follows:

$$w(\theta,t) = \sum_{j=1}^{\infty} \Psi_j(\theta)\, \mathrm{q}_j(t) \simeq \Psi(\theta)\, q(t) \tag{4.11}$$

$$\mathrm{q}_j(t) = B_j \exp(\hat{\imath}\omega_j t) \tag{4.12}$$

where $\hat{\imath}$ is the imaginary unit $\hat{\imath}=\sqrt{-1}$. For simplicity in future substitutions, only the first order (j=1) is considered throughout this chapter. Eq. (4.11) can be inserted into the governing vibrational Eq. (4.10). This substitution yields the following result:

$$\frac{\partial^6}{\partial \theta^6}\Psi(\theta)q(t) + 2\frac{\partial^4}{\partial \theta^4}\Psi(\theta)q(t) + \frac{\partial^2}{\partial \theta^2}\Psi(\theta)q(t) + \frac{\mathrm{R}^4 \rho\, \mathrm{A}}{\mathrm{E\, I}}\left(\frac{\partial^2 \Psi(\theta)}{\partial \theta^2} - \Psi(\theta)\right)\ddot{q}(t) = 0 \tag{4.13}$$

By substituting Eq. (4.12) into Eq. (4.13), Eq. (4.14) can be derived, as follows:

$$\left(\frac{\partial^6 \Psi(\theta)}{\partial \theta^6} + 2\frac{\partial^4 \Psi(\theta)}{\partial \theta^4} + \frac{\partial^2 \Psi(\theta)}{\partial \theta^2}\right)\exp(i\omega t) - \frac{\mathrm{R}^4 \rho\, \mathrm{A}\, \omega^2}{\mathrm{E\, I}}\left(\frac{\partial^2 \Psi(\theta)}{\partial \theta^2} - \Psi(\theta)\right)\exp(i\omega t) = 0 \tag{4.14}$$

Eq. (4.15) represents a simplified form of Eq. (4.14) after eliminating the time-variable exponential terms from all of its terms.

$$\frac{\partial^6 \Psi(\theta)}{\partial \theta^6} + a \frac{\partial^4 \Psi(\theta)}{\partial \theta^4} + b \frac{\partial^2 \Psi(\theta)}{\partial \theta^2} + c = 0 \tag{4.15}$$

where:

$$a = 2 \tag{4.16}$$

$$b = 1\text{-}\Omega^2 \tag{4.17}$$

$$c = \Omega^2 \tag{4.18}$$

$$\Omega = R^2 \sqrt{\rho A / E I}\, \omega \tag{4.19}$$

The expression that relates the radial and tangential mode shapes can be obtained from Eq. (4.9) and is as follows:

$$U = \frac{\partial \Psi}{\partial \theta} \tag{4.20}$$

4.3 Mode Shape Determination

The general solution of Eq. (4.15) takes the form of:

$$\Psi(\theta) = Z\, e^{\Upsilon \theta} \tag{4.21}$$

Eq. (4.21) can be further simplified as:

$$\Upsilon^6 + a\, \Upsilon^4 + b\, \Upsilon^2 + c = 0 \tag{4.22}$$

Eq. (4.23) represents a simplified form of the aforementioned equation, which can be expressed as a cubic equation:

$$\lambda^3 + a\,\lambda^2 + b\,\lambda + c = 0 \tag{4.23}$$

where $\lambda = \Upsilon^2$. Thus, the six roots of Eq. (4.22) can be found after determining the three roots of Eq. (4.23), i.e., λ_r(r=1-3). To solve a standard cubic equation, a discriminant parameter Δ needs to be defined, as follows [18].

$$\Delta = \bar{Q}^3 + \bar{R}^2 \tag{4.24}$$

where:

$$\bar{Q} = \frac{1}{9}(3b - a^2) \tag{4.25}$$

$$\bar{R} = \frac{1}{54}(9ab - 27c - 2a^3) \tag{4.26}$$

Once Δ has been defined, the roots of Eq. (4.23) can be expressed in the following manner:

$$\lambda_1 = S + T - \frac{a}{3} \tag{4.27}$$

$$\lambda_2 = -\frac{1}{2}(S + T) - \frac{a}{3} + i\left(\frac{\sqrt{3}}{2}(S - T)\right) \tag{4.28}$$

$$\lambda_3 = -\frac{1}{2}(S + T) + \frac{a}{3} + i\left(\frac{\sqrt{3}}{2}(S - T)\right) \tag{4.29}$$

where:

$$S = \sqrt[3]{\bar{R} + \sqrt{\Delta}} \tag{4.30}$$

$$T = \sqrt[3]{\bar{R} - \sqrt{\Delta}} \tag{4.31}$$

According to Eq. (4.21), the following can be obtained:

$$\Psi(\theta) = \sum_{i=1}^{6} A_i \, e^{\Upsilon_i \theta} = A_1 e^{\Upsilon_1 \theta} + A_2 e^{\Upsilon_2 \theta} + A_3 e^{\Upsilon_3 \theta} + A_4 e^{\Upsilon_4 \theta} + A_5 e^{\Upsilon_5 \theta} + A_6 e^{\Upsilon_6 \theta} \tag{4.32}$$

Or alternatively as:

$$\Psi(\theta) = A_1 e^{\sqrt{\lambda_1}\theta} + A_2 e^{-\sqrt{\lambda_1}\theta} + A_3 e^{\sqrt{\lambda_2}\theta} + A_4 e^{-\sqrt{\lambda_2}\theta} + A_5 e^{\sqrt{\lambda_3}\theta} + A_6 e^{-\sqrt{\lambda_3}\theta} \tag{4.33}$$

The roots of Eq. (4.23), denoted as λ_r (r=1,2,3) can take on different forms depending on the value of the discriminant Δ.

- If Δ>0, there will be one real root, and the other two roots will be complex conjugates.
- In the case of Δ=0, all three roots will be real, but two of them will be identical, resulting in a set of repeated roots in the system. In this scenario, the corresponding terms of Eq. (4.33) associated with the repeated roots will take the form of $\left(A_{rep}+A_{rep+1}\theta\right)e^{\sqrt{\lambda_{rep}}\theta}$.
- Finally, when Δ<0, all roots will be real and distinct. The value of the discriminant for this system is expressed below:

$$\Delta = -\frac{c^3}{27} + \frac{71\,c^2}{108} - \frac{2\,c}{27} \tag{4.34}$$

4.4 Boundary Conditions

To verify the method, two simple cases, namely hinged and fixed, are examined here. Firstly, the scenario assumes that the ring is hinged to its frame at n distinct points. Secondly, n fixed supports are employed to secure the ring along its rim. Assuming equal lengths for all segments, the angle ζ between any two connected segments can be expressed in the following manner:

$$\zeta = \frac{2\pi}{n} \quad (rad) \tag{4.35}$$

4.4.1 Hinged Supports

The slope and bending moment of the ring can be expressed as $\frac{\partial^2 w}{\partial \theta^2}$ and $\frac{\partial^3 w}{\partial \theta^3}$, respectively. At each support, the normal and tangential deflections are zero (i.e., u=w=0). In this case, for an arbitrary support i, the boundary conditions can be expressed as:

$$u_i(\theta_i) = 0 \tag{4.36}$$

$$w_i(\theta_i) = 0 \tag{4.37}$$

$$\left.\frac{\partial^2 w}{\partial \theta^2}\right]_{\theta=\theta_i} = 0 \tag{4.38}$$

In this step, Eqs. (4.36) through (4.38) need to be substituted into Eq. (4.33). The resulting equations for a candidate segment are shown as follows.

Zero tangential deflection at each support of a candid segment:

$$\Psi(0) = A_1 + A_2 + A_3 + A_4 + A_5 + A_6 = 0 \tag{4.39}$$

$$\Psi(\zeta) = A_1 e^{\sqrt{\lambda_1}\zeta} + A_2 e^{-\sqrt{\lambda_1}\zeta} + A_3 e^{\sqrt{\lambda_2}\zeta} + A_4 e^{-\sqrt{\lambda_2}\zeta} + A_5 e^{\sqrt{\lambda_3}\zeta} + A_6 e^{-\sqrt{\lambda_3}\zeta} = 0 \tag{4.40}$$

Zero radial deflection at each support of a candid segment:

$$\left.\frac{d\Psi(\theta)}{d\theta}\right]_{\theta=0} = \sqrt{\lambda_1}A_1 - \sqrt{\lambda_1}A_2 + \sqrt{\lambda_2}A_3 - \sqrt{\lambda_2}A_4 + \sqrt{\lambda_3}A_5 - \sqrt{\lambda_3}A_6 = 0 \tag{4.41}$$

$$\begin{aligned}\left.\frac{d\Psi(\theta)}{d\theta}\right]_{\theta=\zeta} &= \sqrt{\lambda_1}A_1 e^{\sqrt{\lambda_1}\zeta} - \sqrt{\lambda_1}A_2 e^{-\sqrt{\lambda_1}\zeta} + \sqrt{\lambda_2}A_3 e^{\sqrt{\lambda_2}\zeta} - \sqrt{\lambda_2}A_4 e^{-\sqrt{\lambda_2}\zeta} \\ &+ \sqrt{\lambda_3}A_5 e^{\sqrt{\lambda_3}\zeta} - \sqrt{\lambda_3}A_6 e^{-\sqrt{\lambda_3}\zeta} = 0\end{aligned} \tag{4.42}$$

Zero moment at each support of a candid segment:

$$\left.\frac{d^3\Psi(\theta)}{d\theta^3}\right]_{\theta=0} = \sqrt{{\lambda_1}^3}A_1 - \sqrt{{\lambda_1}^3}A_2 + \sqrt{{\lambda_2}^3}A_3 - \sqrt{{\lambda_2}^3}A_4 + \sqrt{{\lambda_3}^3}A_5 - \sqrt{{\lambda_3}^3}A_6 = 0 \tag{4.43}$$

$$\begin{aligned}\left.\frac{d^3\Psi(\theta)}{d\theta^3}\right]_{\theta=\zeta} &= \sqrt{{\lambda_1}^3}A_1 e^{\sqrt{\lambda_1}\zeta} - \sqrt{{\lambda_1}^3}A_2 e^{-\sqrt{\lambda_1}\zeta} + \sqrt{{\lambda_2}^3}A_3 e^{\sqrt{\lambda_2}\zeta} - \sqrt{{\lambda_2}^3}A_4 e^{-\sqrt{\lambda_2}\zeta} \\ &+ \sqrt{{\lambda_3}^3}A_5 e^{\sqrt{\lambda_3}\zeta} - \sqrt{{\lambda_3}^3}A_6 e^{-\sqrt{\lambda_3}\zeta} = 0\end{aligned} \tag{4.44}$$

Eqs. (4.39) through (4.44) form a homogeneous system of equations that can be represented in matrix form as shown below:

$$\begin{bmatrix} 1 & 1 & 1 & 1 & 1 & 1 \\ \sqrt{\lambda_1} & -\sqrt{\lambda_1} & \sqrt{\lambda_2} & -\sqrt{\lambda_2} & \sqrt{\lambda_3} & -\sqrt{\lambda_3} \\ \sqrt{{\lambda_1}^3} & -\sqrt{{\lambda_1}^3} & \sqrt{{\lambda_2}^3} & -\sqrt{{\lambda_2}^3} & \sqrt{{\lambda_3}^3} & -\sqrt{{\lambda_3}^3} \\ e^{\sqrt{\lambda_1}\zeta} & e^{-\sqrt{\lambda_1}\zeta} & e^{\sqrt{\lambda_2}\zeta} & e^{-\sqrt{\lambda_2}\zeta} & e^{\sqrt{\lambda_3}\zeta} & e^{-\sqrt{\lambda_3}\zeta} \\ \sqrt{\lambda_1}e^{\sqrt{\lambda_1}\zeta} & -\sqrt{\lambda_1}e^{-\sqrt{\lambda_1}\zeta} & \sqrt{\lambda_2}e^{\sqrt{\lambda_2}\zeta} & -\sqrt{\lambda_2}e^{-\sqrt{\lambda_2}\zeta} & \sqrt{\lambda_3}e^{\sqrt{\lambda_3}\zeta} & -\sqrt{\lambda_3}e^{-\sqrt{\lambda_3}\zeta} \\ \sqrt{{\lambda_1}^3}e^{\sqrt{\lambda_1}\zeta} & -\sqrt{{\lambda_1}^3}e^{-\sqrt{\lambda_1}\zeta} & \sqrt{{\lambda_2}^3}e^{\sqrt{\lambda_2}\zeta} & -\sqrt{{\lambda_2}^3}e^{-\sqrt{\lambda_2}\zeta} & \sqrt{{\lambda_3}^3}e^{\sqrt{\lambda_3}\zeta} & -\sqrt{{\lambda_3}^3}e^{-\sqrt{\lambda_3}\zeta} \end{bmatrix} \begin{Bmatrix} A_1 \\ A_2 \\ A_3 \\ A_4 \\ A_5 \\ A_6 \end{Bmatrix} = \{0\} \quad (4.45)$$

If the determinant of the coefficient matrix in Eq. (4.45) is equal to zero, it indicates the existence of a non-trivial solution. To achieve this, first, λ_r(r=1-3) in Eq (4.45) need to be replaced by their ω-based representations using Eqs. (4.27) through (4.29). Consequently, the determinant of the coefficient matrix in Eq. (4.45) will become a function solely dependent on ω. By equating this determinant to zero, the natural frequencies of the system can be determined, and the constants A_i(i=1-6) can be derived accordingly.

4.4.2 Fixed Supports

In this scenario, at each node, the radial and tangential deflections are both zero, represented as u=w=0. The slope and bending moment for the ith support must be identical when calculated based on either the ith or (i+1)th segment. Therefore, the boundary conditions regarding the slope and bending moment must be continuous along the rim. Mathematically, this is expressed in Eqs. (4.46) through (4.49) for k = 1, 2, ..., n-1.

$$u_i(\theta_i) = 0 \quad (4.46)$$

$$w_i(\theta_i) = 0 \quad (4.47)$$

$$\left(\frac{\partial^2 w_{k+1}}{\partial\theta^2}+w_{k+1}\right)\Big]_{\theta=\theta_i}=\left(\frac{\partial^2 w_k}{\partial\theta^2}+w_k\right)\Big]_{\theta=\theta_i+\zeta} \tag{4.48}$$

$$\left(\frac{\partial^3 w_{k+1}}{\partial\theta^3}+\frac{\partial w_{k+1}}{\partial\theta}\right)\Big]_{\theta=\theta_i}=\left(\frac{\partial^3 w_k}{\partial\theta^3}+\frac{\partial w_k}{\partial\theta}\right)\Big]_{\theta=\theta_i+\zeta} \tag{4.49}$$

Zero tangential deflection at the beginning of a candid segment at θ=0:

$$\sum_{i=1}^{6} A_{k,i} = A_{k,1}+A_{k,2}+A_{k,3}+A_{k,4}+A_{k,5}+A_{k,6}=0 \tag{4.50}$$

Zero tangential deflection at the end of a candid segment at θ=ζ:

$$\sum_{i=1}^{6} A_{k,i}e^{\Upsilon_i\zeta} = A_{k,1}e^{\Upsilon_1\zeta}+A_{k,2}e^{\Upsilon_2\zeta}+A_{k,3}e^{\Upsilon_3\zeta}+A_{k,4}e^{\Upsilon_4\zeta}+A_{k,5}e^{\Upsilon_5\zeta}+A_{k,6}e^{\Upsilon_6\zeta}=0 \tag{4.51}$$

Zero radial deflection at the beginning of a candid segment at θ=0:

$$\sum_{i=1}^{6} \Upsilon_i A_{k,i} = \Upsilon_1 A_{k,1}+\Upsilon_2 A_{k,2}+\Upsilon_3 A_{k,3}+\Upsilon_4 A_{k,4}+\Upsilon_5 A_{k,5}+\Upsilon_6 A_{k,6}=0 \tag{4.52}$$

Zero radial deflection at the end of a candid segment at θ=ζ:

$$\begin{aligned}\textstyle\sum_{i=1}^{6}\Upsilon_i A_{k,i}e^{\Upsilon_i\zeta} &= \Upsilon_1 A_{k,1}e^{\Upsilon_1\zeta}+\Upsilon_2 A_{k,2}e^{\Upsilon_2\zeta}+\Upsilon_3 A_{k,3}e^{\Upsilon_3\zeta}+\Upsilon_4 A_{k,4}e^{\Upsilon_4\zeta}+\\ &\Upsilon_5 A_{k,5}e^{\Upsilon_5\zeta}+\Upsilon_6 A_{k,6}e^{\Upsilon_6\zeta}=0\end{aligned} \tag{4.53}$$

Continuous slope at the studied node:

$$\sum_{i=1}^{6}\left(\Upsilon_i{}^2+1\right)\left(A_{k,i}e^{\Upsilon_i\zeta}-A_{k,i+1}\right)=0 \tag{4.54}$$

Continuous bending moment at the studied node:

$$\sum_{i=1}^{6}\left(\Upsilon_i{}^3+1\right)\left(A_{k,i}e^{\,\Upsilon_i\zeta}-A_{k,i+1}\right)=0 \tag{4.55}$$

Eqs. (4.50) through (4.55) can be represented in matrix form by multiplying the parameter matrix by the coefficient matrix. The parameter matrix has an order of 6n×6n, where n is the number of segments.

$$[G(\omega)]\,\{A_{11}\;A_{12}\;A_{13}\;A_{14}\;A_{15}\;A_{16}\;\cdots\;A_{n1}\;\;A_{n2}\;\;A_{n3}\;\;A_{n4}\;\;A_{n5}\;\;A_{n6}\}^T=\{0\} \tag{4.56}$$

A non-trivial solution of Eq. (4.56) exists if the determinant of matrix G(ω) is zero. By setting the determinant of this matrix to zero, the natural frequencies of the system can be derived. The associated constants A_{ki} (k=1-n, i=1-6) for the mode shape function can be evaluated corresponding to each natural frequency. For instance, for the natural frequency ω_r, there will be 6n mode shape constants A_{ki} of which 6n-1 can be expressed based on the remaining one.

4.5 Case Study

A symmetrically supported thin-walled ring with a rectangular cross-section is studied in this section. The parameters of the ring for Cobalt (CAS number 7440-48-4) are given in Table 4.1.

Table 4.1. Parameters of a thin-walled ring

Definition		Value	Unit
Radius	R	0.484	m
Thickness	h	0.008	m
Width	b	0.032	m
Density	ρ	8800	kg/m^3
Cross-sectional area	A	2.56×10^{-4}	m^2
Poisson's ratio	ν	0.32	-
Young's modulus	E	211	GPa

4.6 Finite Element Verification

In order to confirm the outcomes achieved via the analytical approach employed in this study, the utilization of Abaqus software was implemented. An isotropic and homogeneous thin-walled ring, characterized by the values outlined in Table 4.1, was simulated within the Abaqus software. The vibrational analysis required the definition of material properties such as Young's modulus, Poisson's ratio, and density.

In this analysis, the frequency increment using the linear perturbation approach has been opted for. This method is well-suited for deriving natural frequencies and modal patterns. Within Abaqus software, two options for eigenvalue extraction are available: the Lanczos

method and the subspace iteration method. For this particular procedure, the Lanczos method was selected with a maximum of 35 steps and a block size of 7. The Lanczos method is notably efficient when dealing with systems characterized by numerous degrees of freedom that demand a substantial number of eigenmodes, making it a suitable choice for the present study. The upper limit for the frequency of interest or the count of eigenvalues was configured at 20.

In the present model, two distinct boundary conditions are taken into account: hinged and fixed. These conditions have been simulated within the Abaqus software. The count of supports is systematically altered, ranging from 3 to 5. In all instances, these supports are uniformly distributed around the circumference of the ring.

Within Abaqus software, numerous mesh element types are available, each appropriate for analyzing the vibration of slender beams. The selection of the most suitable element type hinges on the unique attributes and demands of the analysis. Properly assigning the appropriate element type stands as a pivotal facet of the meshing process. Linear elements employing complete integration might encounter shear locking issues and demonstrate greater stiffness when contrasted with quadratic elements.

Within the system under investigation, the circumference is notably greater than the cross-sectional measurements, rendering the utilization of beam elements feasible. Abaqus offers a range of beam element options that prove highly suitable for the analysis of slender beams. These elements are characterized by one-dimensional attributes and are exceptionally well-suited for representing structures with pronounced aspect ratios. Beam elements are commonly used to model slender structures like beams. These elements simplify the analysis by assuming that the cross-section of the beam remains constant along its length. The beam

element represents the beam's behavior in terms of bending, axial, and shear deformations. Beam elements are suitable for capturing the global bending behavior and fundamental vibration modes of a circular beam. In many finite element analysis (FEA) software packages such as Abaqus, beam elements are readily available and can be defined by specifying the beam's geometry, material properties, and boundary conditions. They require fewer computational resources compared to solid elements and can be efficient for many vibration analyses.

Nonetheless, it's important to note the rationale underlying the preference for beam elements in lieu of shell elements. Shell elements encompass both bending and membrane distortions, rendering them apt for scrutinizing intricate vibration modes and stress dispersions. However, the usage of shell elements necessitates a finer mesh in comparison to beam elements due to their capacity to capture fluctuations in circular beam thickness and curvature. While they do incur greater computational demands, shell elements yield heightened precision in vibration analysis outcomes for curved structures. The choice between beam elements and shell elements depends on the specific requirements of the analysis. If capturing the fundamental vibration modes and global behavior of the circular beam is the primary point of interest, then beam elements are the better choice due to their computational efficiency. On the other hand, if a more detailed analysis considering complex vibration modes or stress distributions is needed, shell elements would be more appropriate, albeit at the cost of increased computational resources.

Hence, within the scope of this chapter, beam element B33 is utilized. B33 represents a cubic beam element that disregards shear flexibility and assumes minor axial strain, while still

accommodating substantial displacements and rotations of the beams. As such, this element proves appropriate for the simulation of thin-walled rings.

4.6.1 Mesh Convergency

The process of mesh convergence involves refining the finite element mesh to achieve accurate and reliable results in numerical simulations. Mesh convergence analysis entails systematically increasing the mesh density and assessing the changes in the computed solution.

Fig. 4.2 illustrates the convergence of the mesh as the total degrees of freedom (DOF) within the model increase. Typically, reducing the mesh size leads to an augmentation in total DOF, thereby enhancing the precision of solutions by better capturing the representation of designs across physical domains. Nevertheless, this compromise implies that greater accuracy corresponds to larger simulations, leading to extended solution times.

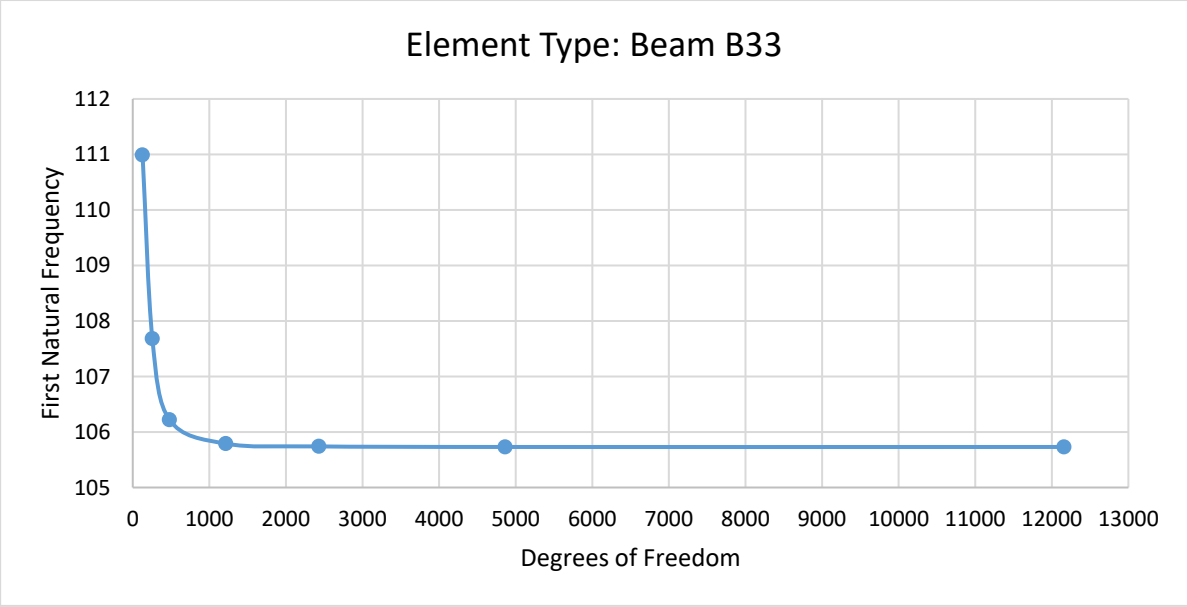

Fig. 4.2 *Mesh convergency for a thin-walled ring with four hinged supports*

Based on what was discussed above and the findings presented in Fig. 4.2, the choice for the model entails utilizing the B33 element with dimensions of 0.005 m in all directions.

4.7 Results and Conclusion

The current study focuses on examining the dynamic behavior of a symmetrically supported thin-walled ring. The analysis considers two types of boundary conditions: hinged and fixed supports. Numerical examples using the Abaqus package were conducted to verify the accuracy of the analytical solutions. Table 4.2 displays the first three natural frequencies for both cases. The slight variations between the analytical and FEM results can be attributed to simplifications made in the mathematical model, such as the neglect of rotary inertia and shear deformations.

Table 4.2. Comparison of natural frequencies obtained from analytical method and FEM

Type and Number of Supports		ω_1 (Hertz)		ω_2 (Hertz)		ω_3 (Hertz)	
		Analytical	FEM	Analytical	FEM	Analytical	FEM
Hinged	3	53.18	53.24	145.45	147.06	256.76	259.35
	4	105.59	105.73	246.89	248.51	470.03	474.18
	5	174.01	174.20	406.24	408.31	745.21	749.72
Fixed	3	89.87	89.96	177.92	179.18	322.65	326.31

4	173.48	173.53	327.43	329.58	593.52	598.13
5	281.03	281.16	516.64	519.16	944.98	949.88

Fig. 4.3 displays the deflected ring for selected scenarios from the aforementioned table. Both analytical and FEM methods confirm that the natural frequencies are significantly higher for the case with fixed supports, compared to the case with hinged supports. This behavior aligns with the physical model of the problem and can be predicted accordingly.

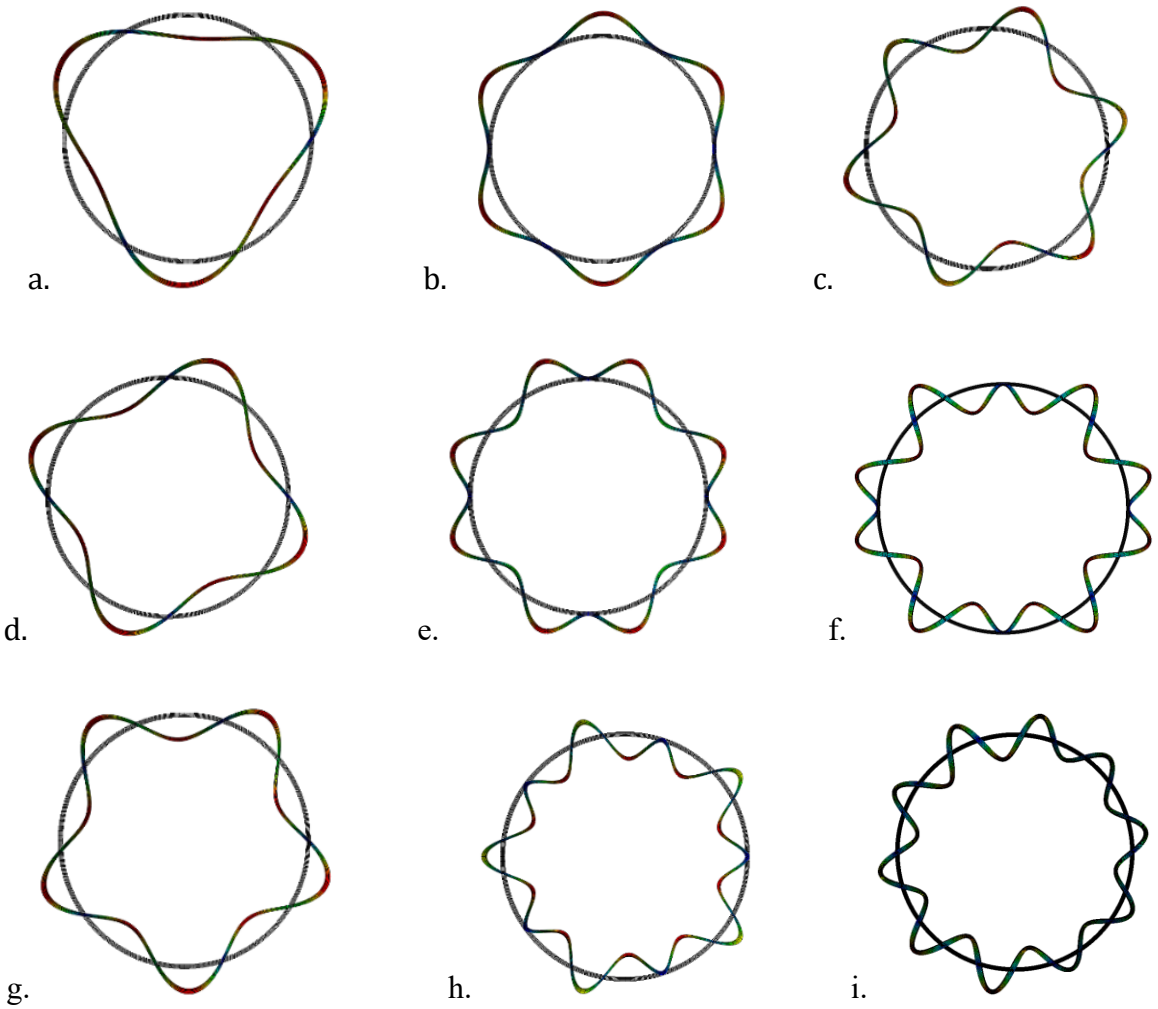

Fig. 4.3 *Mode shapes for a thin-walled ring having 3 (a-c), 4 (d-f), and 5 (g-i) hinged supports*

The natural frequencies derived from the formulation in the present study show a high level of accuracy when compared to the FEM results, particularly for lower frequencies. However, slight differences were observed for higher natural frequencies due to the simplifying assumptions made in the governing equations. Nevertheless, the analysis results obtained in this study exhibit excellent agreement with the FEM results obtained using Abaqus software.

The other notable result is that, as observed in Table 4.2, a ring with a fixed support exhibits higher natural frequencies compared to a ring with a hinged support. The fixed support imposes greater constraints on the ring's motion, leading to increased stiffness and higher natural frequencies.

When considering the natural frequency spectrum of the ring, the frequencies of the modes are generally higher in the fixed support case. This is because the fixed supports increase the overall stiffness of the system, resulting in higher natural frequencies compared to the hinged support case. Additionally, the frequency spacing between the modes varies depending on the number of supports. As observed in Table 4.2, when the number of supports increases, the spacing between the mode shapes also increases. The information presented in this table can assist operational engineers in determining the optimal count of supports for a system, aiming to prevent resonances and potential failures.

References

[1] R. Hoppe, The bending vibration of circular ring, Crelle Journal of Mathematics 73, pp. 158-168 (1871).

[2] S.S. Rao, Vib. of continuous systems, (2019). https://doi.org/10.1002/9781119424284.

[3] X. Wu, R.G. Parker, Vibration of rings on a general elastic foundation, J Sound Vib. 295 (2006). https://doi.org/10.1016/j.jsv.2006.01.007.

[4] D. Zhang, S. Wang, J. Liu, Analytical prediction for free response of rotationally ring-shaped periodic structures, Journal of Vibration and Acoustics, Transactions of the ASME. 136 (2014). https://doi.org/10.1115/1.4027630.

[5] T.E. Lang, Vibration of thin circular rings, Part II. Modal functions and eigenvalues of constrained semicircular rings No. JPL-TR-32-261 (1963).

[6] R.E. Ball, Dynamic Analysis of Rings by Finite Differences, Journal of the Engineering Mechanics Division. 93 (1967). https://doi.org/10.1061/jmcea3.0000823.

[7] M. Jočković, G. Radenković, M. Nefovska-Danilović, M. Baitsch, Free vibration analysis of spatial Bernoulli–Euler and Rayleigh curved beams using isogeometric approach, Appl Math Model. 71 (2019). https://doi.org/10.1016/j.apm.2019.02.002.

[8] P. Zhang, H. Qing, Free vibration analysis of Euler–Bernoulli curved beams using two-phase nonlocal integral models, JVC Journal of Vibration and Control. 28 (2022). https://doi.org/10.1177/10775463211022483.

[9] K. Singh, B.L. Dhoopar, Free vibration of circular rings on radial supports, J Sound Vib. 65 (1979). https://doi.org/10.1016/0022-460X(79)90521-2.

[10] F.M. Detinko, Free vibration of a thick ring on multiple supports, Int J Eng Sci. 27 (1989). https://doi.org/10.1016/0020-7225(89)90066-9.

[11] D. Allaei, W. Soedel, T.Y. Yang, Natural frequencies and modes of rings that deviate from perfect axisymmetry, J Sound Vib. 111 (1986). https://doi.org/10.1016/S0022-460X(86)81419-5.

[12] S.S. Rao, V. Sundararajan, In-plane flexural vibrations of circular rings, Journal of Applied Mechanics, Transactions ASME. 36 (1964). https://doi.org/10.1115/1.3564726.

[13] K.B. Sahay, V. Sundararajan, Vibration of a stiffened ring considered as a cyclic structure, J Sound Vib. 22 (1972). https://doi.org/10.1016/0022-460X(72)90456-7.

[14] T.J. McDaniel, Dynamics of circular periodic structures, J Aircr. 8 (1971). https://doi.org/10.2514/3.44245.

[15] V.R. Murthy, N.C. Nigam, Dynamic characteristics of stiffened rings by transfer matrix approach, J Sound Vib. 39 (1975). https://doi.org/10.1016/S0022-460X(75)80222-7.

[16] A.K. Mallik, D.J. Mead, Free vibration of thin circular rings on periodic radial supports, J Sound Vib. 54 (1977). https://doi.org/10.1016/0022-460X(77)90402-3.

[17] A.E. Zakrzhevskii, V.F. Tkachenko, V.S. Khoroshilov, Natural modes and frequencies of in-plane vibrations of a fixed elastic ring, International Applied Mechanics. 46 (2011). https://doi.org/10.1007/s10778-011-0436-3.

[18] J.W. W., M.R. Spiegel, Mathematical Handbook of Formulas and Tables 5e Scham's outlines, (2018). ISBN: 978-1260010534.

CHAPTER 5

Free In-plane Vibration of Thin-Walled Rings with Elastic Supports

Authorship Statement.

A version of this chapter was published in the Springer Journal of Mechanical Science and Technology in 2023 (https://doi.org/10.1007/s12206-022-1203-6). As the first author, I developed the algorithm and performed numerical validation. Dr. James Yang, as the supervisor, proposed the concept, and reviewed the manuscript. Below is a concise summary outlining the declaration that identifies the authors of this work and describes the authors' contributions.

Javad Abedini: *Investigation, Methodology, Software, Writing - Original Draft, Review & Editing, Validation.*

James Yang: *Conceptualization, Methodology, Visualization, Supervision.*

Abstract – This study investigates the free in-plane vibration of a thin-walled ring with elastic supports. These supports are represented as linear springs in the radial, tangential, and torsional directions to simulate bolt supports. The natural frequency and mode shape of the system are determined by employing the Euler-Bernoulli theory and assuming inextensibility for the ring. Furthermore, the influence of model parameters, such as the radius-to-thickness ratio and support stiffness, is examined. The model is validated by comparing the results with those obtained from FEM analysis and existing publications that consider simpler boundary conditions.

Keywords: Euler-Bernoulli Beam; Free Vibration; Mode Shape; Natural Frequency; Ring Vibration.

5.1 Introduction

Thin-walled rings find extensive applications in various fields. One example is the ring (annulus) gear in a planetary gear train (PGT) [1]. The vibration behavior of rings has captivated the attention of numerous researchers since the 19th century. Hoppe [2] and Love [3] are recognized as early pioneers in the study of thin-walled ring vibrations. Their theories laid the foundation for subsequent works that expanded and enriched both theoretical advancements and practical applications. Chidamparam and Leissa [4] conducted a comprehensive literature review on ring vibration prior to 1993.

The purpose of free vibration analysis is to determine natural frequencies and mode shapes of a system. Several methods have been developed for this purpose, such as the finite element method (FEM) [5,6,7], iso-geometric approach [8], and the transfer matrix method [9,10]. These numerical techniques are capable of handling complex scenarios involving rings with various types of constraints. However, in some cases, a closed-form representation of the mode shapes is needed. Closed-form solutions for natural frequencies and mode shapes of unconstrained rings were obtained in previous works [11-14]. Lacarbonara et al. [15] extended the analysis to incorporate nonlinear material properties. Zakrzhevskii et al. [16] investigated the free vibration of an elastic ring with one fixed point. Rao and Sundararajan [12] determined the natural frequencies and mode shapes of a ring with multiple rigid radial supports, including hinged and fixed supports. Their findings indicated that the method yielded satisfactory results when the number of supports was low. However, as the number of supports increased, the results became less accurate. Sahay and Sundararajan [17] examined a ring with equally spaced supports using Green's function and Galerkin's technique. Malik and Mead [18] employed a wave approach based on the propagation constants of the ring, assuming it to be an endless periodic structure. Luo et al. [19] studied the impact of bolt constraint on a planetary gearbox's ring gear vibration. They used a test rig, performed experiments, and analyzed results using frequency response functions and spectral analysis. Their findings revealed that bolt constraint strongly influences ring gear vibration.

In spite of the numerous references mentioned earlier, it is evident that while researchers have extensively explored vibration suppression in rings, there has been limited attention given to studying the effects of various boundary conditions. The existing studies have primarily focused on rings with either hinged or fixed supports. However, accurate

analysis of any model relies on appropriately addressing boundary conditions, making it crucial to investigate the impact of different conditions. This research aims to fill this gap by introducing a model that can encompass the aforementioned scenarios and even more complicated situations.

Another deficiency in the existing literature pertains to the insufficient availability of analytical methodologies compared to those mentioned earlier, such as Galerkin, wave approach, transfer matrix, and other FEM techniques. Specifically, the absence of a closed-form expression for mode shapes in a ring with general elastic supports remains a challenge. Therefore, a primary goal of this study is to address this gap by devising a technique that allows for an analytical closed-form representation of mode shapes in a ring supported by any desired number of general supports.

Furthermore, another important aim of this study is to examine the impact of the system's support stiffness. Given the broad appeal of this research topic to individuals from diverse backgrounds, the results obtained from this analysis can be valuable in aiding users across various disciplines.

This chapter aims to address those three gaps in the literature and is organized as follows: Section 5.2 presents the modeling of the in-plane vibration of the ring and provides the equation of motion. The solution technique is introduced in Section 5.3, followed by a discussion on the boundary conditions in Section 5.4. Section 5.5 presents a case study that is examined, and the conclusions are drawn in Section 5.6.

5.2 Dynamic Model

Fig. 5.1 depicts a thin-walled elastic ring that is attached to a frame using multiple bolts. These bolts are represented by three linear springs to account for the radial, tangential, and torsional rigidity. For simplification, the centerline is used to represent the ring as shown in Fig. 5.2. To develop the mathematical model, the following assumptions are made:

- The bending rigidity of the ring, EI, is constant.
- The rotary inertia and shear deformation are neglected.
- The supports are equally distributed circumferentially.
- The centerline of the ring remains inextensible.

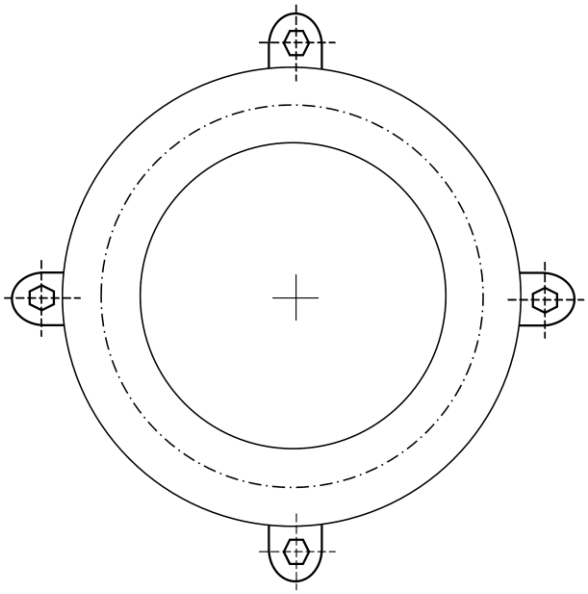

Fig. 5.1 *A thin-walled ring with bolted supports*

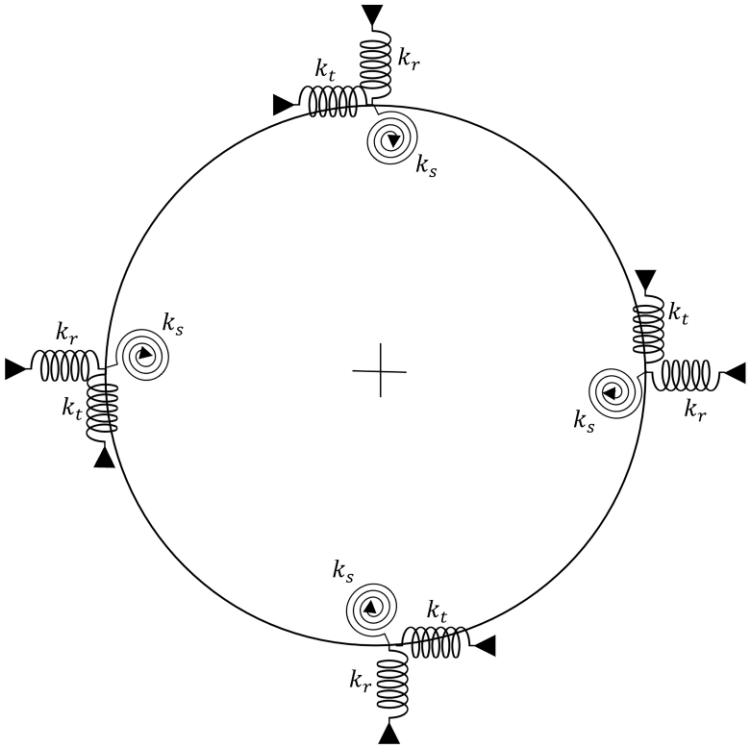

Fig. 5.2 *Mathematical representation of flexible supports*

5.2.1 System Equations

The ring under investigation is connected to the frame by n bolts. The segments between the adjacent supports are sequentially numbered, as shown in Fig. 5.3. Any point on the centerline experiences both radial displacement (u) and tangential displacement (w). To derive the equation, a differential element of the ring is extracted at an arbitrary position of θ, as illustrated in Fig. 5.4. The internal forces and moments acting on this element include the normal force (N), the shear force (Q), and the in-plane bending moment (M). The positive directions of these forces and moment are indicated in Fig 5.4.

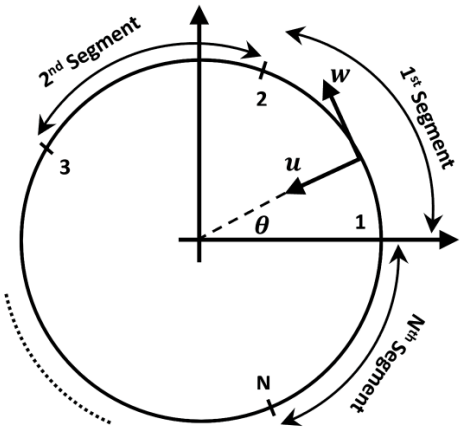

Fig. 5.3 *Ring segment*

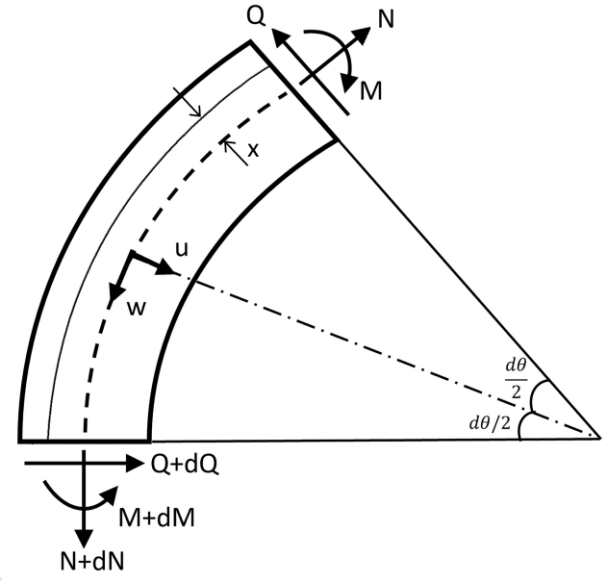

Fig. 5.4 *Ring element*

By neglecting higher-order terms, the in-plane vibration equation of the ring can be expressed in the following form. A detailed derivation can be found in various publications, such as [11], and is not provided here for the sake of brevity.

$$\frac{\partial^6 w(\theta,t)}{\partial\theta^6} + 2\frac{\partial^4 w(\theta,t)}{\partial\theta^4} + \frac{\partial^2 w(\theta,t)}{\partial\theta^2} + \frac{\mathrm{R}^4 \rho\, \mathrm{A}}{\mathrm{E\,I}} \frac{\partial^2}{\partial t^2}\left(\frac{\partial^2 w(\theta,t)}{\partial\theta^2} - w(\theta,t)\right) = 0 \qquad (5.1)$$

where *w(θ,t)* is the tangential displacement of the ring centerline, R is the radius of the ring centerline, ρ is the mass density, A is the cross-sectional area, and I is the moment of inertia of the cross-sectional area A. The rotation of a cross-section, denoted as φ, as well as the moment *M* and the normal force *N*, are expressed as follows [9,10,17]:

$$\varphi = \frac{1}{\mathrm{R}}\left(\frac{\partial u}{\partial \theta} + w\right) \tag{5.2}$$

$$M = \frac{\mathrm{EI}}{\mathrm{R}}\left(\frac{\partial \varphi}{\partial \theta}\right) \tag{5.3}$$

$$N = \frac{\mathrm{EA}}{\mathrm{R}}\left(\frac{\partial w}{\partial \theta} - u\right) - \frac{M}{\mathrm{R}} = \frac{\mathrm{EA}}{\mathrm{R}}\left(\frac{\partial w}{\partial \theta} - u\right) - \frac{\mathrm{EI}}{\mathrm{R}^2}\left(\frac{\partial \varphi}{\partial \theta}\right) \tag{5.4}$$

Given that the centerline is assumed inextensible, the following relation is held [9]:

$$u = \frac{\partial w}{\partial \theta} \tag{5.5}$$

Eq. (5.5) represents the inextensibility condition. Under this condition, the following relation can be obtained:

$$\mathrm{Q} = -\frac{1}{\mathrm{R}}\frac{\partial \mathrm{M}}{\partial \theta} = -\frac{\mathrm{EI}}{\mathrm{R}^2}\left(\frac{\partial^2 \varphi}{\partial \theta^2}\right) \tag{5.6}$$

5.3 Solution Strategy

Eq. (5.1) can be solved by employing separation-of- variable technique, assuming the following.

$$w(\theta,t)=\sum_{j=1}^{\infty}\Psi_j(\theta)\,\mathrm{q}_j(t)\simeq\Psi(\theta)\,q(t) \tag{5.7}$$

$$\mathrm{q}_j(t)=B_j\exp(\hat{\imath}\omega_j t) \tag{5.8}$$

where $\Psi(\theta)$ is the mode shape and$\hat{\imath}$ is the imaginary unit number $\hat{\imath}=\sqrt{-1}$. Substituting Eq. (5.7) into Eq. (5.1) gives:

$$\frac{\partial^6}{\partial\theta^6}\Psi(\theta)q(t)+2\frac{\partial^4}{\partial\theta^4}\Psi(\theta)q(t)+\frac{\partial^2}{\partial\theta^2}\Psi(\theta)q(t)+\frac{\mathrm{R}^4\rho\,\mathrm{A}}{\mathrm{E\,I}}\left[\frac{\partial^2\Psi(\theta)}{\partial\theta^2}-\Psi(\theta)\right]\ddot{q}(t)=0 \tag{5.9}$$

Upon substituting Eq. (5.8) into Eq. (5.9), the subsequent equation can be derived.

$$\left[\frac{\partial^6\Psi(\theta)}{\partial\theta^6}+2\frac{\partial^4\Psi(\theta)}{\partial\theta^4}+\frac{\partial^2\Psi(\theta)}{\partial\theta^2}\right]\exp(\hat{\imath}\omega t)-\frac{\mathrm{R}^4\rho\,\mathrm{A}\,\omega^2}{\mathrm{E\,I}}\left[\frac{\partial^2\Psi(\theta)}{\partial\theta^2}-\Psi(\theta)\right]\exp(\hat{\imath}\omega t)=0 \tag{5.10}$$

The following must be true if the above holds.

$$\frac{\partial^6\Psi(\theta)}{\partial\theta^6}+\mathrm{a}\,\frac{\partial^4\Psi(\theta)}{\partial\theta^4}+\mathrm{b}\,\frac{\partial^2\Psi(\theta)}{\partial\theta^2}+\mathrm{c}=0 \tag{5.11}$$

where:

$$\mathrm{a}=2 \tag{5.12}$$

$$\mathrm{b}=1-\Omega^2 \tag{5.13}$$

$$\mathrm{c}=\Omega^2 \tag{5.14}$$

$$\Omega=\mathrm{R}^2\sqrt{\rho\,\mathrm{A}/\mathrm{E\,I}}\,\omega \tag{5.15}$$

Assuming Eq. (5.11) has a solution of the following form:

$$\Psi(\theta) = A\, e^{\Upsilon \theta} \tag{5.16}$$

Substituting Eq. (5.16) into Eq. (5.11) yields the following algebraic equation.

$$\Upsilon^6 + a\,\Upsilon^4 + b\,\Upsilon^2 + c = 0 \tag{5.17}$$

Eq. (5.17) can be simplified by letting $\lambda = \Upsilon^2$

$$\lambda^3 + a\,\lambda^2 + b\,\lambda + c = 0 \tag{5.18}$$

In order to solve Eq. (5.18), a discriminant parameter Δ is defined as follows [20].

$$\Delta = \bar{H}^3 + \bar{R}^2 \tag{5.19}$$

where:

$$\bar{H} = \frac{1}{9}(3b - a^2) \tag{5.20}$$

$$\bar{R} = \frac{1}{54}(9ab - 27c - 2a^3) \tag{5.21}$$

Eq. (5.16) can be reformulated as follows:

$$\Psi(\theta) = A_1 e^{\sqrt{\lambda_1}\theta} + A_2 e^{-\sqrt{\lambda_1}\theta} + A_3 e^{\sqrt{\lambda_2}\theta} + A_4 e^{-\sqrt{\lambda_2}\theta} + A_5 e^{\sqrt{\lambda_3}\theta} + A_6 e^{-\sqrt{\lambda_3}\theta} \tag{5.22}$$

λ_r $(r = 1,2,3)$ takes different forms based on the discriminant Δ. This is discussed below:

- $\Delta > 0$: There are one real root and two complex roots, which are complex conjugates.
- $\Delta = 0$: All three roots are real; however, two of them are repeated, meaning there is a set of repeated roots in the system. Consequently, the corresponding terms in Eq. (5.22) associated with the repeated roots will assume the form of $\left(A_{rep} + A_{rep+1}\theta\right)e^{\sqrt{\lambda_{rep}}\theta}$.

- $\Delta < 0$: All roots are real and distinct. For this case, the discriminant is expressed below:

$$\Delta = -\frac{c^3}{27} + \frac{71\,c^2}{108} - \frac{2\,c}{27} \tag{5.23}$$

Based on the three aforementioned cases, the mode shape will exhibit different forms, which will be discussed in the following section.

5.4 Compatibility and Equilibrium Conditions

Assuming the n bolts are evenly distributed, as depicted in Fig. 5.3, the angle ζ between any two adjacent supports is given by the following expression:

$$\zeta = \frac{2\pi}{n} \tag{5.24}$$

The radial displacement u and rotational motion φ can be determined once the tangential displacement w is found. They can be expressed as follows:

$$u(\theta, t) = \sum_{j=1}^{\infty} D_j\, U_j(\theta)\, q_j(t) \simeq U(\theta)\, q(t) \tag{5.25}$$

$$\varphi(\theta, t) = \sum_{j=1}^{\infty} E_j\, \Phi_j(\theta)\, q_j(t) \simeq \Phi(\theta)\, q(t) \tag{5.26}$$

The boundary conditions for a general support can be represented as follows:

$$\Psi_i(\theta_i) = \Psi_{i+1}(\theta_i) \tag{5.27}$$

$$U_i(\theta_i) = U_{i+1}(\theta_i) \tag{5.28}$$

$$\Phi_i(\theta_i) = \Phi_{i+1}(\theta_i) \tag{5.29}$$

$$\overline{N}_i(\theta_i) = \overline{N}_{i+1}(\theta_i) - k_t \Psi_i(\theta_i) \tag{5.30}$$

$$\overline{Q}_i(\theta_i) = \overline{Q}_{i+1}(\theta_i) - k_r U_i(\theta_i) \tag{5.31}$$

$$\overline{M}_i(\theta_i) = \overline{M}_{i+1}(\theta_i) - k_s \Phi_i(\theta_i) \tag{5.32}$$

Where subscript i represent the number of the studied segment. Eqs. (5.27) through (5.29) express the continuity of tangential, radial, and rotational displacements across the support. The variables Φ, $\bar{N}$, $\bar{Q}$, and $\bar{M}$ represent the rotation angle, normal force, shear force, and bending moment of the cross-section at the support. These variables are calculated based on Eqs. (5.2) through (5.4), and (5.6) as follows:

$$\Phi = \frac{1}{\mathrm{R}}\left(\frac{\partial U}{\partial \theta} + \Psi\right) \tag{5.33}$$

$$\overline{N} = \frac{\mathrm{EA}}{\mathrm{R}}\left(\frac{\partial \Psi}{\partial \theta} - U\right) - \frac{\mathrm{EI}}{\mathrm{R}^2}\left(\frac{\partial \Phi}{\partial \theta}\right) \tag{5.34}$$

$$\overline{Q} = -\frac{\mathrm{EI}}{\mathrm{R}^2}\left(\frac{d^2 \Phi}{d\theta^2}\right) \tag{5.35}$$

$$\overline{M} = \frac{\mathrm{EI}}{\mathrm{R}}\left(\frac{d\Phi}{d\theta}\right) \tag{5.36}$$

Due to Eq. (5.5), Eq. (5.34) can be simplified as follows:

$$\overline{N} = -\frac{\mathrm{EI}}{\mathrm{R}^2}\left(\frac{\partial \Phi}{\partial \theta}\right) \tag{5.37}$$

By substituting Eqs. (5.22) and (5.33)-(5.36) into Eqs. (5.27) through (5.32), the following equations can be obtained.

$$\sum_{k=1}^{6}\left(A_{i,k}-A_{i+1,k}\right) e^{\Upsilon_k \beta_s}=0 \tag{5.38}$$

$$\sum_{k=1}^{6}\left(A_{i,k}-A_{i+1,k}\right) \Upsilon_k e^{\Upsilon_k \beta_s}=0 \tag{5.39}$$

$$\sum_{k=1}^{6}\left(A_{i,k}-A_{i+1,k}\right) \left(1+\Upsilon_k^{\,2}\right) e^{\Upsilon_k \beta_s}=0 \tag{5.40}$$

$$\sum_{k=1}^{6}\left[\left(-\frac{EI}{R^3}\left(\Upsilon_k^{\,3}+\Upsilon_k\right)+k_t\right) A_{i,k}+\frac{EI}{R^3}\left(\Upsilon_k^{\,3}+\Upsilon_k\right) A_{i+1,k}\right] e^{\Upsilon_k \beta_s}=0 \tag{5.41}$$

$$\sum_{k=1}^{6}\left[\left(-\frac{EI}{R^3}\left(\Upsilon_k^{\,3}+\Upsilon_k\right)+k_r\right) A_{i,k}+\frac{EI}{R^3}\left(\Upsilon_k^{\,3}+\Upsilon_k\right) A_{i+1,k}\right] \Upsilon_k e^{\Upsilon_k \beta_s}=0 \tag{5.42}$$

$$\sum_{k=1}^{6}\left[\left(\frac{EI}{R^2}\Upsilon_k+\frac{k_s}{R}\right) A_{i,k}-\left(\frac{EI}{R^2}\Upsilon_k\right) A_{i+1,k}\right] \left(1+\Upsilon_k^{\,2}\right) e^{\Upsilon_k \beta_s}=0 \tag{5.43}$$

where β_s is the position of the selected node (or the support). For each support, a set of six equations, Eqs. (5.38) through (5.43), can be formulated. Consequently, the entire ring is described by 6n equations, which can be reorganized into a concise matrix form as:

$$[G(\omega)]\left\{A_{1,1}\ A_{1,2}\ A_{1,3}\ A_{1,4}\ A_{1,5}\ A_{1,6}\cdots A_{n,1}\ \ A_{n,2}\ \ A_{n,3}\ \ A_{n,4}\ \ A_{n,5}\ \ A_{n,6}\right\}^{T}=\{0\} \tag{5.44}$$

where $G(\omega)$ is a 6n×6n matrix. In the specific case of four supports (n=4), the matrix $G(\omega)$ is provided in Appendix B. A non-trivial solution of Eq. (5.44) exists when the determinant of $G(\omega)$ is zero. By solving:

$$|G(\omega)|=0\ , \tag{5.45}$$

the natural frequencies ω will be obtained. Subsequently, the mode shape can be obtained using Eq. (5.22). The complexity of Eq. (5.45) varies depending on the number of supports, as the size of the matrix is influenced by this factor. Eq. (5.45) can be solved analytically or numerically through various methods, such as the modified Newton-Raphson method.

5.5 Case Study

A ring with rectangular cross section is investigated in this section. The ring is supported by four bolts that are equally spaced (n=4). The parameters of both the ring and the supports are presented in Table 5.1.

Table 5.1. Parameters of a thin-walled ring

Definition		Value	Unit
Radius	R	0.484	m
Thickness	h	0.008	m
Width	b	0.032	m
Density	ρ	8800	kg/m^3
Cross-sectional area	A	2.56×10^{-4}	m^2
Poisson's ratio	ν	0.32	-
Young's modulus	E	211	GPa

Tangential spring constant	k_t	7.263×10^7	N/m
Radial spring constant	k_r	7.263×10^7	N/m
Rotational spring constant	k_s	4.315×10^8	N-m/rad

5.5.1 Natural Frequencies and Mode Shapes

Following the methodology outlined in Section 5.4, Eq. (5.44) is derived. The detailed entries of this matrix are provided and explained in Appendix B. Eq. (5.45) is solved numerically in Maple package by using the modified Newton-Raphson and Bisection methods. The first four natural frequencies are presented in Table 5.2 and validated against FEM results. The details about the Abaqus model is explained in subsection 5.5.2.

Table 5.2. System natural frequencies

	1st natural frequency	2nd natural frequency	3rd natural frequency	4th natural frequency
	ω_1 (Hertz)	ω_2 (Hertz)	ω_3 (Hertz)	ω_4 (Hertz)
Current Study	25.72	121.80	269.23	469.29
FEM (Abaqus)	25.718	122.03	266.13	450.17

The corresponding mode shapes are depicted in Figs 5.5 through 5.8. In these figures, the undeformed shapes are shown as dashed lines, while the solid lines represent the mode

shapes with deformation. It is important to note that only the radial displacement is visible in these illustrations.

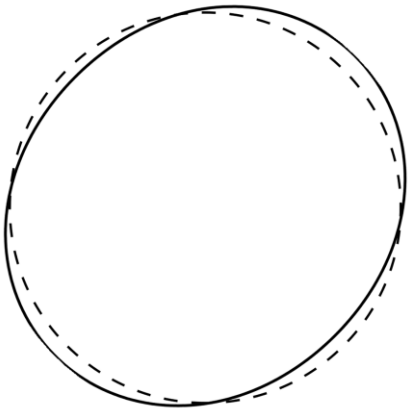

Fig. 5.5 *1st order mode shape*

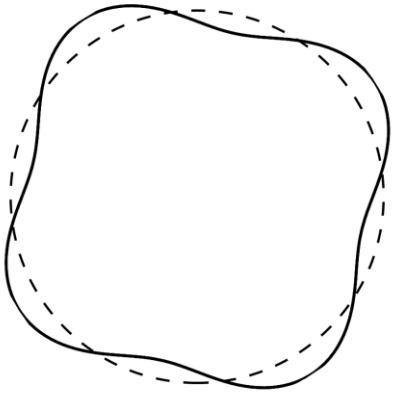

Fig. 5.6 *2nd order mode shape*

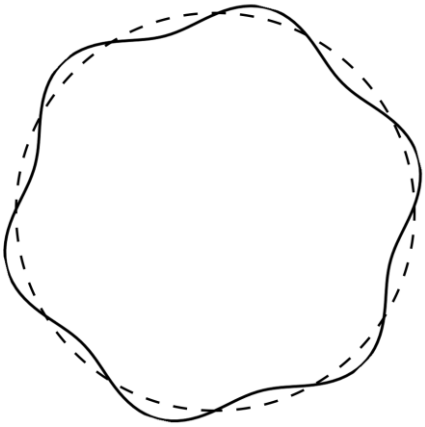

Fig. 5.7 *3rd order mode shape*

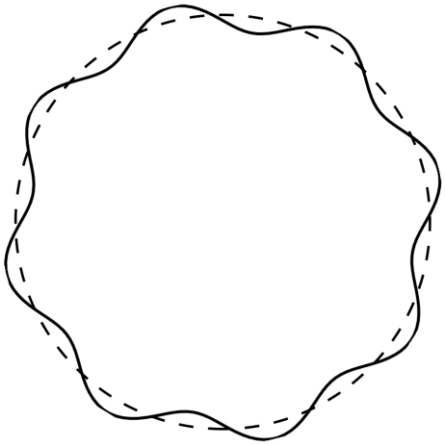

Fig. 5.8 *4th order mode shape*

5.5.2 Verification Methods

To substantiate the aforementioned findings, a validation process was carried out through Finite Element Analysis (FEA) using the Abaqus software. To execute this

validation, a homogenous and isotropic thin-walled ring made from Cobalt, with dimensions and properties provided in Table 5.1, was simulated within the Abaqus software environment.

Within this analysis framework, the linear perturbation approach was employed to progressively increment the frequency. The Lanczos method, with its default settings, was selected as the analytical technique to ascertain the natural frequencies and mode shapes of the system. Notably, the Lanczos method proves highly effective when dealing with systems marked by a multitude of degrees of freedom, demanding a considerable count of eigenmodes. This suitability drove the choice of this method for the current investigation. The frequency of interest was capped at 20, determining the count of eigenvalues to be considered.

To simulate the system, the ring was supported by four equally spaced bolt supports. These supports were modeled in Abaqus as springs acting in radial, tangential, and torsional directions. The springs were assumed to be massless and were defined using the dedicated "Springs/Dashpots" tab within the Engineering Features module of the software. The process of setting up these springs is elaborated in the Abaqus Documentation [21]. Nevertheless, Abaqus also provides more specialized methods for defining springs that can be directly accessed.

Given the high aspect ratio of the ring, beam elements were chosen as the appropriate elements for this simulation. Following the methodology outlined in sub-section 4.6.1, a mesh convergence analysis was performed, leading to the determination of a mesh size of 0.005 m in all directions.

Another approach to validate the results obtained in this study is by comparing them with the findings from previous literature. However, it is important to note that the previous literature primarily focused on simple boundary conditions, such as hinged and fixed supports. Therefore, in order to ensure a meaningful comparison, the methodology used in this study needs to be simplified and aligned with the approaches discussed in the previous literature. The specifications for hinged and fixed supports are summarized below for reference:

- **Hinged:** In this particular scenario, the displacements along the radial and tangential directions, as well as the moment, are all zero. Consequently, the following equations can be obtained:

$$U_i(\theta_i) = 0 \tag{5.46}$$

$$\Psi_i(\theta_i) = 0 \tag{5.47}$$

$$\left.\frac{\partial^2 \Psi}{\partial \theta^2}\right|_{\theta=\theta_i} = 0 \tag{5.48}$$

- **Fixed:** In this case, it is expected that the moment and the slope remain continuous across the support. Additionally, the displacements in both the radial and tangential directions are assumed to be zero. This particular scenario can be simplified to that of a curved beam with fixed supports. The boundary conditions are as follows:

$$U_i(\theta_i) = 0 \tag{5.49}$$

$$\Psi_i(\theta_i) = 0 \tag{5.50}$$

$$\left(\frac{\partial^2 \Psi_{k+1}}{\partial \theta^2} + \Psi_{k+1}\right)\Big|_{\theta=\theta_i} = \left(\frac{\partial^2 \Psi_k}{\partial \theta^2} + \Psi_k\right)\Big|_{\theta=\theta_i+\zeta} \tag{5.51}$$

$$\left(\frac{\partial^3 \Psi_{k+1}}{\partial \theta^3} + \frac{\partial \Psi_{k+1}}{\partial \theta}\right)\Big|_{\theta=\theta_i} = \left(\frac{\partial^3 \Psi_k}{\partial \theta^3} + \frac{\partial \Psi_k}{\partial \theta}\right)\Big|_{\theta=\theta_i+\zeta} \tag{5.52}$$

The results for these two special cases are compared against relevant findings from previously published papers [12, 22-24]. The comparison and discussion of these results are presented below.

Hinged and fixed supports can be incorporated into the methodology presented in this chapter by adjusting the stiffness parameters, denoted as k_r, k_t, and k_s. To mimic the infinite stiffness, a very large number such as $1x10^{20}$ is used in the simulation. A comparison of the first two natural frequencies is presented in Table 5.3, while the corresponding mode shapes are depicted in Figs. 5.9 and 5.10. It is important to note that the mode shapes in [12] were not originally plotted. Hence, for the sake of comparison, they have been reconstructed and included in Figs. 5.9 and 5.10. Both the natural frequencies in Table 5.3 and the mode shapes in Figs. 5.9 and 5.10 demonstrate a high level of agreement between the results obtained using the methodology presented in this chapter and those reported in the referenced publications.

Table 5.3. System natural frequencies comparison

Boundary Conditions Type	Current work ω_1 (Hertz)	Ref. [12] ω_1 (Hertz)
Hinged Supports	105.58	105.62
Fixed Supports	173.46	173.51

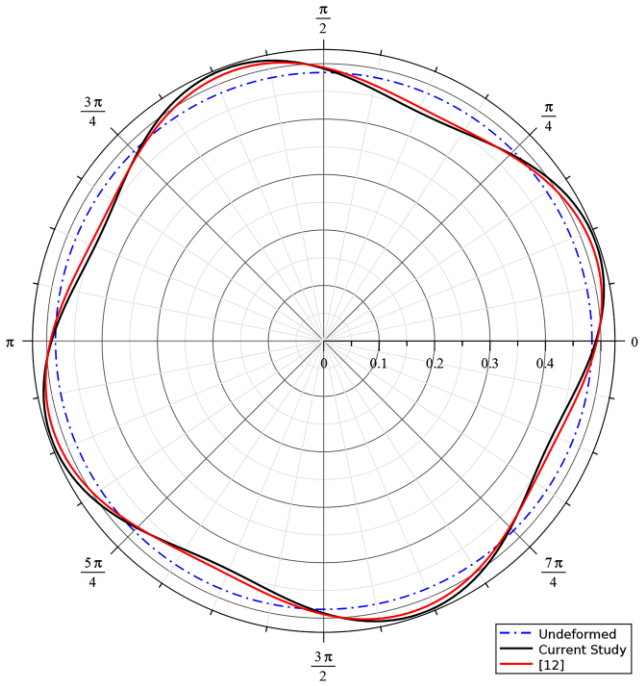

Fig. 5.9 *Ring with four hinged supports*

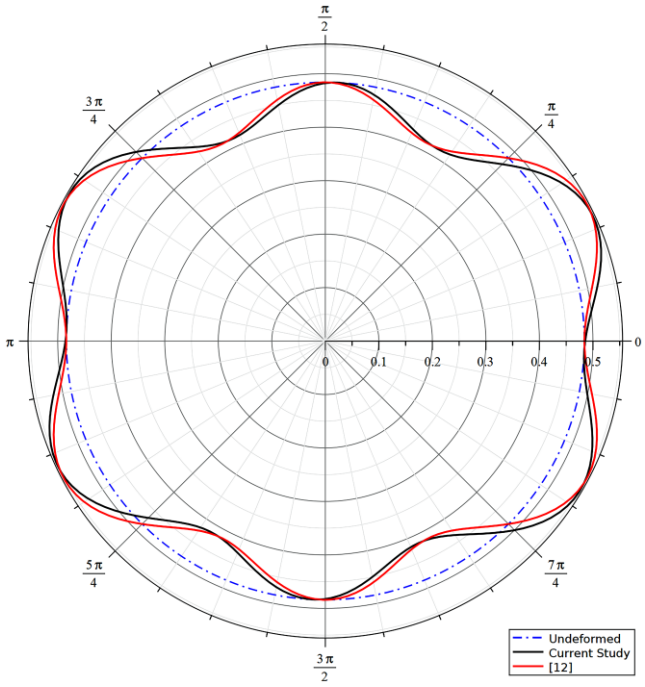

Fig. 5.10 *Ring with four fixed supports*

5.5.3 Parametric Study

The natural frequencies and mode shapes of the system are notably influenced by the stiffness of both the supports and the ring itself. This section provides a brief discussion on these aspects.

5.5.3.1 Radius-to-Thickness Aspect Ratio

The stiffness of the ring can be assessed by considering its radius-to-thickness ratio, denoted as R/t. This ratio holds significance as a design parameter in practical applications. Table 5.4 presents the first two natural frequencies for varying values of the R/t ratio within the range of 10-80.

Table 5.4. Effect of R/t ratio on the system's natural frequencies

R/t ratio	ω_1 (rad/s)	ω_2 (rad/s)
10	145.87	572.70
20	83.46	342.05
50	39.23	142.43
80	18.86	96.43

Clearly, as the R/t ratio increases, both natural frequencies decrease. This relationship is reasonable since a larger R/t ratio corresponds to lower stiffness, resulting in lower natural frequencies.

5.5.3.2 Support Stiffness

To examine the effect of the support stiffness, the following 4 cases are considered:

[1] $k_r = 7 \times 10^9$ (N/m), $k_s = k_t = 0$

[2] $k_s = 7 \times 10^9$ (N·m/rad), $k_r = k_t = 0$

[3] $k_t = 7 \times 10^9$ (N/m), $k_r = k_s = 0$

[4] $k_r = k_s = k_t$ varies from 7×10^8 to 7×10^{10} (N/m, N·m/rad)

The results are presented in Table 5.5.

Table 5.5. System's natural frequencies

Boundary conditions		ω_1 (Hertz)	ω_2 (Hertz)
$k_s = k_t = 0$	$k_r = 7 \times 10^8$ (N/m)	99.91	202.88
	$k_r = 7 \times 10^9$ (N/m)	110.45	263.12
	$k_r = 7 \times 10^{10}$ (N/m)	119.53	307.15
$k_r = k_t = 0$	$k_s = 7 \times 10^8$ (N-m/rad)	100.75	205.50
	$k_s = 7 \times 10^9$ (N-m/rad)	112.03	265.74
	$k_s = 7 \times 10^{10}$ (N-m/rad)	121.46	310.54
$k_r = k_s = 0$	$k_t = 7 \times 10^8$ (N/m)	124.43	245.75
	$k_t = 7 \times 10^9$ (N/m)	**144.98**	**307.65**

	k_t=7×10^{10} (N/m)	166.36	366.64
k_s=7×10^{8}(N-m/rad)	k_r=k_t=7×10^{8} (N/m)	118.60	247.36
k_s=7×10^{9}(N-m/rad)	k_r=k_t=7×10^{9} (N/m)	**145.46**	**298.76**
k_s=7×10^{10}(N-m/rad)	k_r=k_t=7×10^{10} (N/m)	159.06	345.60

The physical interpretation of these springs revolves around their capacity to represent the resistance to the deformation at the bolt supports. As observed from the bolded values in Table 5.5, the tangential stiffness k_t has a more pronounced influence on the results compared to the radial stiffness k_r and rotational stiffness k_s. This behavior can be explained by the significant differences in the contributions of circumferential rigidity (EA) and flexural rigidity (EI) to the overall response. Similar observations have been made in previous research on bridges and curved beams [5,6].

5.6 Conclusions

This chapter focuses on the analysis of free vibration in a thin-walled ring with general supports. Verification is made by comparing the results against that of FEM and previous literature [12, 22-24]. The impact of key parameters on the free vibration behavior is investigated. The findings reveal that the tangential spring stiffness k_t has a more substantial influence on the free vibration characteristics compared to the radial stiffness k_r and torsional stiffness k_t for the specific case studied. The tangential stiffness primarily affects the deformation of the ring in its plane. This mode involves stretching or compressing the ring

along its circumference. Since the thin-walled ring is naturally more flexible in its plane, the tangential stiffness plays a significant role in determining the deformation and, consequently, the natural frequencies associated with this mode.

Additionally, the R/t ratio which represents the ratio of the radius (R) of the ring to its thickness (t) is studied. Results showed that as the R/t ratio of a ring increases, the natural frequencies of the structure decreases. This relationship is reasonable because a larger R/t ratio corresponds to a thinner and more flexible ring, allowing for easier bending and greater vibrational motion.

References

[1] A. Kahraman, A.A. Kharazi, M. Umrani, A deformable body dynamic analysis of planetary gears with thin rims, J Sound Vib. 262 (2003). https://doi.org/10.1016/S0022-460X(03)00122-6.

[2] R. Hoppe, The bending vibration of circular ring, Crelle Journal of Mathematics 73, pp. 158-168 (1871).

[3] A.E.H. Love, A treatise on the mathematical theory of elasticity. Cambridge University Press 4th edition (2013). ISBN-13: 978-1107618091.

[4] P. Chidamparam, A.W. Leissa, Vibrations of planar curved beams, rings, and arches, Appl Mech Rev. 46 (1993). https://doi.org/10.1115/1.3120374.

[5] J.S. Wu, F.T. Lin, H.J. Shaw, Free in-plane vibration analysis of a curved beam (arch) with arbitrary various concentrated elements, Appl Math Model. 37 (2013). https://doi.org/10.1016/j.apm.2013.02.029.

[6] J.S. Wu, Analytical and Numerical Methods for Vibration Analyses, (2015). https://doi.org/10.1002/9781119137207.

[7] R.M. Corrêa, M. Arndt, R.D. Machado, Free in-plane vibration analysis of curved beams by the generalized/extended finite element method, European Journal of Mechanics, A/Solids. 88 (2021). https://doi.org/10.1016/j.euromechsol.2021.104244.

[8] M. Jočković, G. Radenković, M. Nefovska-Danilović, M. Baitsch, Free vibration analysis of spatial Bernoulli–Euler and Rayleigh curved beams using isogeometric approach, Appl Math Model. 71 (2019). https://doi.org/10.1016/j.apm.2019.02.002.

[9] T.J. McDaniel, Dynamics of circular periodic structures, J Aircr. 8 (1971). https://doi.org/10.2514/3.44245.

[10] V.R. Murthy, N.C. Nigam, Dynamic characteristics of stiffened rings by transfer matrix approach, J Sound Vib. 39 (1975). https://doi.org/10.1016/S0022-460X(75)80222-7.

[11] S.S. Rao, Vib. of continuous systems, (2019). https://doi.org/10.1002/9781119424284.

[12] S.S. Rao, V. Sundararajan, In-plane flexural vibrations of circular rings, Journal of Applied Mechanics, Transactions ASME. 36 (1964). https://doi.org/10.1115/1.3564726.

[13] T.E. Lang, Vibration of Thin Circular Rings. Part II. Modal Functions and Eigenvalues of Constrained Semicircular Rings, Jet Propulsion Lab., California Inst. of Tech. Pasadena, USA (1962). Document ID: 19630006566

[14] L.L. Philipson, On the Role of Extension in the Flexural Vibrations of Rings, J Appl Mech. 23 (1956). https://doi.org/10.1115/1.4011337.

[15] W. Lacarbonara, A. Arena, S.S. Antman, Flexural vibrations of nonlinearly elastic circular rings, Meccanica. 50 (2015). https://doi.org/10.1007/s11012-014-0038-3.

[16] A.E. Zakrzhevskii, V.F. Tkachenko, V.S. Khoroshilov, Natural modes and frequencies of in-plane vibrations of a fixed elastic ring, International Applied Mechanics. 46 (2011). https://doi.org/10.1007/s10778-011-0436-3.

[17] K.B. Sahay, V. Sundararajan, Vibration of a stiffened ring considered as a cyclic structure, J Sound Vib. 22 (1972). https://doi.org/10.1016/0022-460X(72)90456-7.

[18] A.K. Mallik, D.J. Mead, Free vibration of thin circular rings on periodic radial supports, J Sound Vib. 54 (1977). https://doi.org/10.1016/0022-460X(77)90402-3.

[19] Y. Luo, L. Cui, J. Ma, Effect of bolt constraint of ring gear on the vibration response of the planetary gearbox, Mech Mach Theory. 159 (2021). https://doi.org/10.1016/j.mechmachtheory.2021.104260.

[20] J.W. W., M.R. Spiegel, Mathematical Handbook of Formulas and Tables 5e Scham's outlines, (2018). ISBN: 978-1260010534.

[21] M. Smith, ABAQUS/Standard User's Manual, Version 6.9, Abaqus Documentation, https://classes.engineering.wustl.edu/2009/spring/mase5513/abaqus/docs/v6.6/books/usi/default.htm?startat=pt04ch20s04hlb01.html.

[22] C.P. Filipich, M.B. Rosales, In-plane vibration of symmetrically supported circumferential rings, J Sound Vib. 136 (1990). https://doi.org/10.1016/0022-460X(90)90858-W.

[23] M.J. Abedinilaksar, J. Yang, Free Vibration Characteristics of a Thin-Walled Ring Under Different Boundary Conditions, (2020). https://doi.org/10.32393/csme.2020.1164.

[24] S. Azimi, In-Plane Vibration of Simply Supported-Simply Supported Circular Ring Segments. Proceedings of the ASME Design Technical Conferences. 13th Biennial Conference on Mechanical Vibration and Noise: Machinery Dynamics and Element Vibrations. Miami, USA. pp. 147-151 (2021). https://doi.org/10.1115/DETC1991-0287.

CHAPTER 6

Vibration Characteristics of a Ring Under General Boundary Conditions using Euler-Bernoulli and Timoshenko Theories

Authorship Statement.

A version of this chapter was published in the Canadian Society of Mechanical Engineers (CSME) congress in Edmonton in 2022 (https://doi.org/10.7939/r3-tp76-1w54). As the first author, I developed the algorithm and performed numerical validation. Dr. James Yang, as the supervisor, proposed the concept, and reviewed the manuscript. Below is a concise summary outlining the declaration that identifies the authors of this work and describes the authors' contributions.

Javad Abedini: *Investigation, Methodology, Software, Writing - Original Draft, Review & Editing, Validation.*
James Yang: *Conceptualization, Methodology, Visualization, Supervision.*

Abstract – Vibration analysis of rings is more challenging compared to that of straight beams. In straight beams, structural deformations are dependent on rotational and translational displacements. However, in rings, in addition to these displacements, there is also a coupled tangential displacement arising from the curvature of the structures. This study addresses the problem of free in-plane vibration for rings, providing explicit relationships between radial, tangential, and rotational displacements. This chapter presents an analytical method for obtaining exact solutions for the natural frequencies and associated mode shapes of a ring under general boundary conditions. Both the Euler-Bernoulli and Timoshenko theories are utilized in this work, and the corresponding results are compared.

Keywords: Ring Vibration; Mode Shape; Natural Frequency; Euler-Bernoulli; Timoshenko Theory.

6.1 Introduction

Rings and curved beams find extensive application in various engineering fields. The vibration analysis of rings has captured the attention of researchers since the 19th century. Hoppe [1] is recognized as a pioneer in the study of thin-walled ring vibrations. The early theoretical work in this area is summarized in the classical theory formulated by Love [2]. Many subsequent research papers on ring and curved-beam analysis [3-6] have been based on Love's

shell theory. For thin-walled rings, Euler-Bernoulli theory can be applied. In this case, the governing equations can be derived using Love's formulation. Love's formulation consist of two coupled equations in the radial and tangential directions. Through mathematical simplification, these coupled differential equations can be reduced to a sixth-order ordinary differential equation with constant coefficients in the tangential direction. Numerous researchers have followed this approach, establishing the bending theory of thin-walled rings, commonly known as Euler-Bernoulli rings. However, for thick-walled rings, Love's formulation is not applicable as it neglects rotatory inertia and shear deformation [7-10]. In this case, Timoshenko theory needs to be used. This type of ring is alternatively referred to as a Timoshenko ring.

The free vibration behavior of unconstrained thin-walled and thick-walled rings has been extensively studied by numerous researchers using various approaches [9,11-17]. The analysis of free vibration in rings becomes inherently more complex when the ring is constrained with elastic supports. Regarding this matter, there have been existing research works [8, 9, 18, 25]. The methods employed in these studies encompass transfer matrix, Galerkin, perturbation, and finite element techniques.

However, the majority of existing works primarily employed the Euler-Bernoulli theory and concentrated on rings with specific constraints such as being free, hinged, or fixed. Conversely, there is a limited number of studies on thick-walled rings with general elastic constraints. For this reason, this chapter will address a ring with general elastic constraints using both the Euler-Bernoulli and Timoshenko theories.

This chapter is organized as follows: Section 6.2 presents the derivation of in-plane vibrational equations for both theories. Mode shapes are discussed in Section 6.3, while Section

6.4 focuses on boundary conditions. In Section 6.5, the details about Abaqus simulation are provided. Section 6.6 conducts a case study under both Euler-Bernoulli and Timoshenko theories. Finally, Section 6.7 draws the conclusions.

6.2 Dynamic Model

Fig. 6.1 depicts a ring that is mounted to its frame with several bolts, while Fig. 6.2 illustrates the ring represented by its centerline. To facilitate the derivation of the governing equations and minimize complexity, the following assumptions are employed:

- The rigidity of the ring, EI, is assumed constant.
- The bolts (elastic supports) are distributed equally.

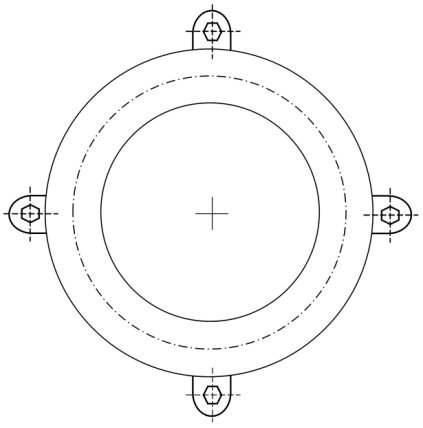

Fig. 6.1 *A ring and the graphical location of each support*

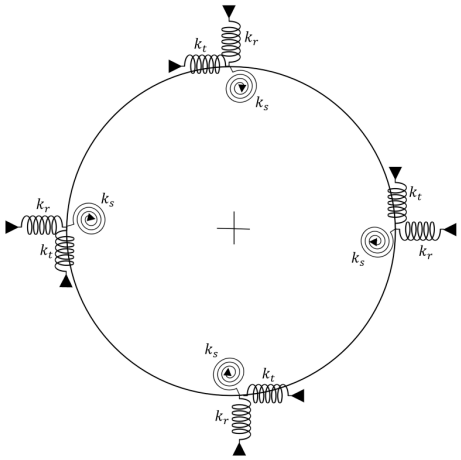

Fig. 6.2 *Representation of each support with three springs*

An element of the ring positioned at an arbitrary angle θ is depicted in Fig. 6.3. The internal forces and moments for this element, as well as their positive directions are indicated in Fig. 6.4.

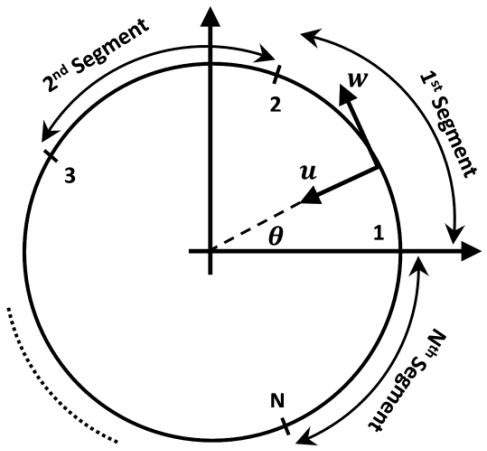

Fig. 6.3 *Ring centerline*

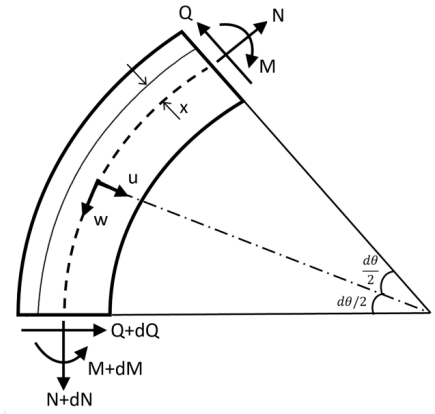

Fig. 6.4 *Element of a ring*

By disregarding the negligible higher-order terms, one can derive the equilibrium equations in three axes of tangential displacement *w*, radial displacement *u*, and the rotation of the cross-section *φ*.

$$\frac{\partial Q}{\partial \theta} + N = \rho A R\, \ddot{u} \tag{6.1}$$

$$\frac{\partial N}{\partial \theta} - Q = \rho A R\, \ddot{w} \tag{6.2}$$

$$\frac{\partial M}{\partial \theta} + RQ = \rho I R\, \ddot{\varphi} \tag{6.3}$$

where R is the radius of ring centerline, ρ is the total mass density, A is the cross-sectional area, and I is the moment of inertia of the cross-sectional area A.

6.2.1 Timoshenko Theory

In Timoshenko beam theory, the contributions of rotary inertia and shear deformation are both taken into account. In order to solve Eqs. (6.1) through (6.3), the following parameters need to be defined: the rotation of a cross-section φ, the moment M, and the normal force N, which are expressed as follows [3, 25, 27]:

$$\varphi = \frac{1}{\mathrm{R}}\left(\frac{\partial u}{\partial \theta} + w - \mathrm{R}\gamma\right) \tag{6.4}$$

$$M = \frac{\mathrm{EI}}{\mathrm{R}}\left(\frac{\partial \varphi}{\partial \theta}\right) = \frac{\mathrm{EI}}{\mathrm{R}^2}\left(\frac{\partial^2 u}{\partial \theta^2} + \frac{\partial w}{\partial \theta} - \mathrm{R}\frac{\partial \gamma}{\partial \theta}\right) \tag{6.5}$$

$$N = \frac{\mathrm{EA}}{\mathrm{R}}\left(\frac{\partial w}{\partial \theta} - u\right) - \frac{\mathrm{M}}{\mathrm{R}} = \frac{\mathrm{EA}}{\mathrm{R}}\left(\frac{\partial w}{\partial \theta} - u\right) - \frac{\mathrm{EI}}{\mathrm{R}^2}\left(\frac{\partial \varphi}{\partial \theta}\right) \tag{6.6}$$

where γ is the shear deformation.

Given that the centerline is assumed inextensible, the following relation is held [3]:

$$u = \frac{\partial w}{\partial \theta} \tag{6.7}$$

With this condition, the relationship between the shear force and the bending moment can be represented as follows:

$$Q = -\mathrm{k'AG}\gamma = -\frac{\mathrm{k'AG}}{\mathrm{R}}\left(\frac{\partial u}{\partial \theta} + w - \mathrm{R}\varphi\right) \tag{6.8}$$

where G is the rigidity modulus of the ring material and k' is a numerical factor that depends on the shape of the cross section.

By substituting Eqs. (6.4)-(6.8) into Eqs. (6.1)-(6.3) and performing necessary simplifications, Eq. (9) can be obtained as follows.

$$\frac{\partial^6 w(\theta,t)}{\partial\theta^6} + 2\frac{\partial^4 w(\theta,t)}{\partial\theta^4} + \frac{\partial^2 w(\theta,t)}{\partial\theta^2} = \left(\frac{R^2\rho}{E} + \frac{R^2\rho}{k\prime G}\right)\frac{\partial^6 w(\theta,t)}{\partial t^2\,\partial\theta^4} - \left(\frac{R^4\rho^2}{Ek\prime G}\right)\frac{\partial^6 w(\theta,t)}{\partial t^4\,\partial\theta^2} + \left(2\frac{R^2\rho}{E} - \frac{R^2\rho}{k\prime G} - \frac{R^4\rho A}{EI}\right)\frac{\partial^4 w(\theta,t)}{\partial t^2\,\partial\theta^2} + \left(\frac{R^4\rho^2}{Ek\prime G}\right)\frac{\partial^4 w(\theta,t)}{\partial t^4} + \left(\frac{R^2\rho}{E} + \frac{R^4\rho A}{EI}\right)\frac{\partial^2 w(\theta,t)}{\partial t^2} \tag{6.9}$$

The detailed derivation of Eq. (6.9) can be found in various publications, such as [3, 11, 24]. For the sake of brevity, that is not provided here. Eq. (6.9) can be solved with the variables separated by assuming the following.

$$w(\theta,t) = \sum_{j=1}^{\infty} \Psi_j(\theta)\,\mathrm{q}_j(t) \simeq \Psi(\theta)\,q(t) \tag{6.10}$$

$$\mathrm{q}_j(t) = B_j \exp(\hat{\imath}\omega_j t) \tag{6.11}$$

where $\Psi(\theta)$ is the mode shape and $\hat{\imath}$is the imaginary unit number$\hat{\imath} = \sqrt{-1}$. Substituting Eq. (6.10) into Eq. (6.9) gives

$$\frac{\partial^6\Psi}{\partial\theta^6} + H_1\frac{\partial^4\Psi}{\partial\theta^4} + H_2\frac{\partial^2\Psi}{\partial\theta^2} + H_3\Psi = 0 \tag{6.12}$$

where:

$$H_1 = 2 + \left(\frac{\mathrm{R}^2\rho}{\mathrm{E}} + \frac{\mathrm{R}^2\rho}{\mathrm{k'G}}\right)\omega^2 \tag{6.13}$$

$$H_2 = 1 + \left(2\frac{\mathrm{R}^2\rho}{\mathrm{E}} - \frac{\mathrm{R}^2\rho}{\mathrm{k\prime G}} - \frac{\mathrm{R}^4\rho\mathrm{A}}{\mathrm{EI}}\right)\omega^2 + \left(\frac{\mathrm{R}^4\rho^2}{\mathrm{Ek\prime G}}\right)\omega^4 \tag{6.14}$$

$$H_3 = \left(\frac{\mathrm{R}^2\rho}{\mathrm{E}} + \frac{\mathrm{R}^4\rho\mathrm{A}}{\mathrm{EI}}\right)\omega^2 - \left(\frac{\mathrm{R}^4\rho^2}{\mathrm{Ek\prime G}}\right)\omega^4 \tag{6.15}$$

6.2.2 Euler-Bernoulli Theory

In Euler-Bernoulli beam theory, the contributions of rotary inertia and shear deformation are disregarded. Therefore, Eqs. (6.4) through (6.6) can be simplified as below [3, 11, 24, 26]:

$$\varphi = \frac{1}{\mathrm{R}}\left(\frac{\partial u}{\partial \theta} + w\right) \tag{6.16}$$

$$M = \frac{\mathrm{EI}}{\mathrm{R}}\left(\frac{\partial \varphi}{\partial \theta}\right) \tag{6.17}$$

$$N = \frac{\mathrm{EA}}{\mathrm{R}}\left(\frac{\partial w}{\partial \theta} - u\right) - \frac{\mathrm{M}}{\mathrm{R}} = \frac{\mathrm{EA}}{\mathrm{R}}\left(\frac{\partial w}{\partial \theta} - u\right) - \frac{\mathrm{EI}}{\mathrm{R}^2}\left(\frac{\partial \varphi}{\partial \theta}\right) \tag{6.18}$$

Moreover, it is feasible to establish the correlation between the shear force and the bending moment in the following manner:

$$Q = -\frac{1}{\mathrm{R}}\frac{\partial M}{\partial \theta} = -\frac{\mathrm{EI}}{\mathrm{R}^2}\left(\frac{\partial^2 \varphi}{\partial \theta^2}\right) \tag{6.19}$$

By substituting Eqs. (6.16) through (6.19) into Eqs. (6.1) through (6.3), the in-plane vibration equation of a ring based on Euler-Bernoulli theory can be expressed in the following form:

$$\frac{\partial^6 w(\theta,t)}{\partial \theta^6} + 2\frac{\partial^4 w(\theta,t)}{\partial \theta^4} + \frac{\partial^2 w(\theta,t)}{\partial \theta^2} + \frac{R^4 \rho\, A}{E\, I}\,\frac{\partial^2}{\partial t^2}\left[\frac{\partial^2 w(\theta,t)}{\partial \theta^2} - w(\theta,t)\right] = 0 \tag{6.20}$$

Substituting Eq. (10) into Eq. (20) gives

$$\frac{\partial^6}{\partial \theta^6}\Psi(\theta)q(t) + 2\frac{\partial^4}{\partial \theta^4}\Psi(\theta)q(t) + \frac{\partial^2}{\partial \theta^2}\Psi(\theta)q(t) + \frac{R^4 \rho\, A}{E\, I}\left[\frac{\partial^2 \Psi(\theta)}{\partial \theta^2} - \Psi(\theta)\right]\ddot{q}(t) = 0 \tag{6.21}$$

Inserting Eq. (6.11) into above, produces

$$\left[\frac{\partial^6\Psi(\theta)}{\partial\theta^6}+2\frac{\partial^4\Psi(\theta)}{\partial\theta^4}+\frac{\partial^2\Psi(\theta)}{\partial\theta^2}\right]\exp(i\omega t)-\frac{R^4\rho\,A\,\omega^2}{E\,I}\left[\frac{\partial^2\Psi(\theta)}{\partial\theta^2}-\Psi(\theta)\right]\exp(i\omega t)=0 \quad (6.22)$$

The following must be true if the above holds.

$$\frac{\partial^6\Psi(\theta)}{\partial\theta^6}+a\,\frac{\partial^4\Psi(\theta)}{\partial\theta^4}+b\,\frac{\partial^2\Psi(\theta)}{\partial\theta^2}+c=0 \quad (6.23)$$

where:

$$a=2 \quad (6.24)$$

$$b=1-\Omega^2 \quad (6.25)$$

$$c=\Omega^2 \quad (6.26)$$

$$\Omega=\mathrm{R}^2\sqrt{\rho\,\mathrm{A}\,/\mathrm{E}\,\mathrm{I}}\,\omega \quad (6.27)$$

6.3 Solution Strategy

Eqs. (6.12) and (6.23) describe the governing equations based on Timoshenko and Euler-Bernoulli theories, respectively. It is postulated that a solution for those equations can be represented in the following form:

$$\Psi(\theta)=A\,e^{\Upsilon\,\theta} \quad (6.28)$$

This equation can be alternatively expressed in terms of λ_r as shown below.

$$\Psi(\theta) = A_1 e^{\sqrt{\lambda_1}\theta} + A_2 e^{-\sqrt{\lambda_1}\theta} + A_3 e^{\sqrt{\lambda_2}\theta} + A_4 e^{-\sqrt{\lambda_2}\theta} + A_5 e^{\sqrt{\lambda_3}\theta} + A_6 e^{-\sqrt{\lambda_3}\theta} \quad (6.29)$$

The detailed methodology for solving Eq. (6.29) has been extensively explained in Chapter 5, Section 5.3.

6.4 Compatibility and Equilibrium Conditions

Due to the evenly distributed of the bolts, as illustrated in Fig 6.2, the angle ζ between any two adjacent supports can be expressed as:

$$\zeta = \frac{2\pi}{n} \quad (6.30)$$

The radial displacement u and rotational motion φ can be determined based on the tangential displacement *w*. They can be expressed as follows, utilizing the mode shape.

$$u(\theta, t) = \sum_{j=1}^{\infty} D_j \, U_j(\theta) \, \mathrm{q}_j(t) \simeq U(\theta) \, q(t) \quad (6.31)$$

$$\varphi(\theta, t) = \sum_{j=1}^{\infty} E_j \, \Phi_j(\theta) \, \mathrm{q}_j(t) \simeq \Phi(\theta) \, q(t) \quad (6.32)$$

The boundary conditions for a bolt support can be expressed as follows:

$$\Psi_i(\theta_i) = \Psi_{i+1}(\theta_i) \quad (6.33)$$

$$\mathrm{U}_i(\theta_i) = \mathrm{U}_{i+1}(\theta_i) \quad (6.34)$$

$$\Phi_i(\theta_i) = \Phi_{i+1}(\theta_i) \quad (6.35)$$

$$\bar{N}_i(\theta_i) = \bar{N}_{i+1}(\theta_i) - k_t \Psi_i(\theta_i) \tag{6.36}$$

$$\bar{Q}_i(\theta_i) = \bar{Q}_{i+1}(\theta_i) - k_r \mathrm{U}_i(\theta_i) \tag{6.37}$$

$$\bar{M}_i(\theta_i) = \bar{M}_{i+1}(\theta_i) - k_s \Phi_i(\theta_i) \tag{6.38}$$

Eqs. (6.33) through (6.38) establish the continuity of the tangential, radial, and rotational displacements across the support. Φ, $\bar{N}$, $\bar{Q}$, and $\bar{M}$ represent the rotation angle, normal force, shear force, and bending moment of the cross-section at the support, respectively. These quantities can be computed using Eqs. (6.4), (6.5), (6.6), (6.8), and (6.16) through (6.19) as described in [11]:

$$\bar{N} = \frac{\mathrm{EA}}{\mathrm{R}}\left(\frac{\partial \Psi}{\partial \theta} - U\right) - \frac{\mathrm{EI}}{\mathrm{R}^2}\left(\frac{\partial \Phi}{\partial \theta}\right) \tag{6.39}$$

$$\bar{M} = \frac{\mathrm{EI}}{\mathrm{R}}\left(\frac{\mathrm{d}\Phi}{\mathrm{d}\theta}\right) \tag{6.40}$$

$$\Phi_{EB} = \frac{1}{\mathrm{R}}\left(\frac{\partial U}{\partial \theta} + \Psi\right) \tag{6.41}$$

$$\Phi_T = \frac{1}{\mathrm{R}}\left(\frac{\mathrm{d}^2\Psi}{\mathrm{d}\theta^2} + \frac{\mathrm{EI}/\mathrm{R}^2}{\rho \mathrm{AR}^2\omega^2 - \mathrm{EA}}\Psi\right) \tag{6.42}$$

$$\bar{Q}_{EB} = -\frac{\mathrm{EI}}{\mathrm{R}^2}\left(\frac{\mathrm{d}^2\Phi}{\mathrm{d}\theta^2}\right) \tag{6.43}$$

$$\bar{Q}_T = -\frac{\mathrm{k'AG}}{\mathrm{R}}\left(\frac{\partial U}{\partial \theta} + \Psi - \mathrm{R}\Phi_T\right) \tag{6.44}$$

where the indices “EB” and “T” represent Euler-Bernoulli and Timoshenko theory, respectively.

The methodology described can be employed for both theories, but it is crucial to utilize the appropriate versions of Eq. (6.41) through (6.44) for each specific scenario. By substituting Eq. (6.7) into Eq. (6.39), Eq. (6.39) can be simplified as follows.

$$\bar{N} = -\frac{\mathrm{EI}}{\mathrm{R}^2}\left(\frac{\partial \varphi}{\partial \theta}\right) \tag{6.45}$$

By applying the methodology described in Section 5.4 to both theories, the system of equations can be reorganized into a compact matrix form as follows:

$$[G(\omega)]\left\{\mathrm{A}_{1,1}\ \mathrm{A}_{1,2}\ \mathrm{A}_{1,3}\ \mathrm{A}_{1,4}\ \mathrm{A}_{1,5}\ \mathrm{A}_{1,6}\cdots \mathrm{A}_{\mathrm{n},1}\ \ \mathrm{A}_{\mathrm{n},2}\ \ \mathrm{A}_{\mathrm{n},3}\ \ \mathrm{A}_{\mathrm{n},4}\ \ \mathrm{A}_{\mathrm{n},5}\ \ \mathrm{A}_{\mathrm{n},6}\right\}^{\mathrm{T}}=\{0\} \tag{6.46}$$

where $G(\omega)$ is a matrix of $6n \times 6n$. For the specific case of four supports (n=4), the values of $G(\omega)$ are provided in Appendix B. A non-trivial solution of Eq. (6.46) exists if the determinant of $G(\omega)$ is equal to zero. By solving

$$|G(\omega)| = 0, \tag{6.47}$$

the natural frequencies ω will be obtained. Then the mode shape can be plotted through Eq. (6.29).

6.5 Abaqus Simulation

To simulate a ring in Abaqus, the procedure outlined in Chapter 4, Section 4.6 should be followed. However, an additional step involves identifying appropriate elements that can differentiate between Euler-Bernoulli and Timoshenko theories. The classical Euler-Bernoulli assumption is the simplest approach to beam theory, positing that plane cross-sections initially normal to the beam's axis remain plane, normal to the beam axis, and undistorted. In Abaqus,

the beam elements employing cubic interpolation (such as element types B23, B33, etc.) adopt this assumption while accommodating arbitrarily large rotations and small strains. Conversely, Abaqus beam elements utilizing linear and quadratic interpolation (B21, B22, B31, B32, PIPE21, PIPE22, PIPE31, PIPE32, etc.) are based on a similar formulation but allow for transverse shear strain, meaning that the cross-section may not necessarily remain normal to the beam axis. This extension corresponds to the Timoshenko beam theory, which is particularly useful for thicker beams where shear flexibility becomes significant. Quadratic terms in the nominal torsional strain are neglected in comparison to unity, and the axial strain is assumed to be small when calculating the torsional shear strain. Consequently, while axial strains can be arbitrarily large, only moderately large torsional strain is accurately modeled, and that too under the condition that the axial strain is not substantial. Throughout the motion, it is assumed that the ring's radius of curvature is significantly larger than distances within the cross-section, thereby preventing the beam from folding into a tight hinge. Another assumption made is that the strain within the ring's cross-section remains consistent in all directions and throughout the section.

Figs. 6.5 and 6.6 display the specifications of Euler-Bernoulli and Timoshenko elements in Abaqus, respectively. Both types of elements are employed in this chapter for their corresponding models. It is worth noting that when using the Timoshenko beam element, which employs a different analysis formulation [26], a higher number of mesh divisions is generally required to achieve a more accurate response compared to the Euler-Bernoulli case.

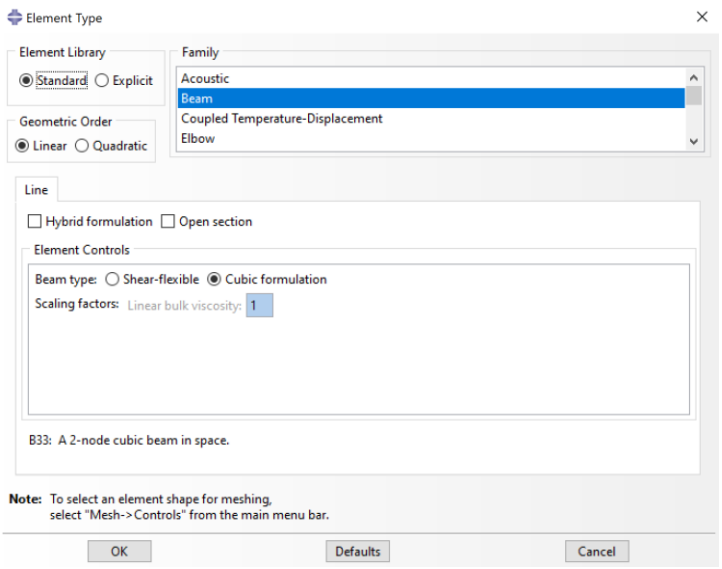

Fig. 6.5 *Euler-Bernoulli beam element in Abaqus, B33*

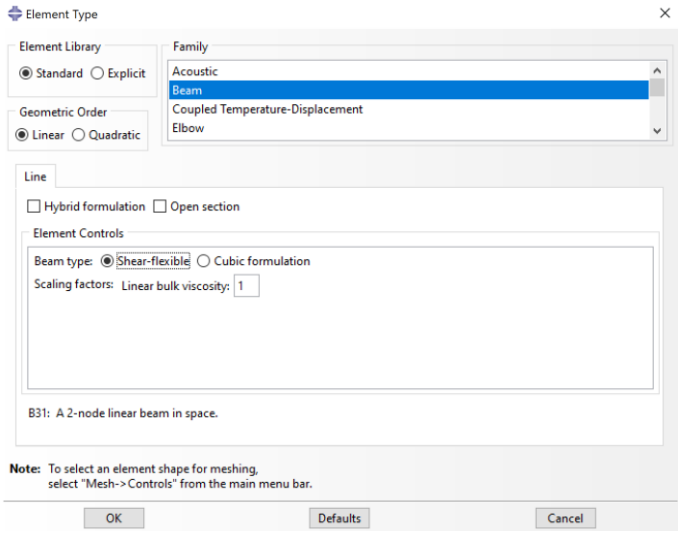

Fig. 6.6 *Timoshenko beam element in Abaqus, B31*

The cubic elements illustrated in Fig. 6.6 for Euler-Bernoulli beam elements lack the ability to incorporate shear flexibility. Consequently, the cross-sections of these elements maintain their perpendicular orientation to the beam axis. However, for Timoshenko elements, that shear factor needs to be considered. According to the Abaqus Documentation [27] and as listed in Table 6.2, the shear factor varies among different types of cross-sections. In the present

model, the cross section of the ring is rectangular, and Abaqus has taken into account a shear factor of 85%.

Table 6.1. Abaqus shear factor

Section Type	Box, I, T	Hex, Pipe	Circular	Elbow	**Rectangular**	Trapezoidal	Others
Shear Factor	0.44	0.53	0.89	0.85	**0.85**	0.822	1

6.6 Case Study

This section investigates a symmetrically supported ring with a rectangular cross-section. The ring is supported by four bolts equally spaced around its perimeter (n=4). The parameters for the ring and supports are provided in Table 6.2 below.

Table 6.2. Parameters of a thin-walled ring

Definition		Value	Unit
Radius	R	0.484	m
Thickness	h_1	0.008	m
	h_2	0.032	m
Width	b	0.032	m
Density	ρ	8800	kg/m^3

Cross-sectional area	A	2.56×10^{-4}	m^2
Poisson's ratio	ν	0.32	-
Young's modulus	E	211	GPa
Rigidity modulus	G	82.6	GPa
Tangential spring constant	k_t	7.263×10^7	N/m
Radial spring constant	k_r	7.263×10^7	N/m
Rotational spring constant	k_s	4.315×10^8	N-m/rad

Following the methodology explained in Sections 6.4 and 6.5, Eq. (6.46) can be derived for both Euler-Bernoulli and Timoshenko theories. The detailed entries of the matrix for the Euler-Bernoulli case are presented in Appendix B. Eq. (6.47) typically needs to be solved numerically for both cases. In this chapter, the Maple package is utilized to solve these equations for two sample thicknesses listed in Table 6.2. For each thickness, the first six natural frequencies are determined using the modified Newton-Raphson and Bisection methods, and listed in Tables 6.3 and 6.4, respectively.

Table 6.3. System's natural frequencies for a ring with thickness of h_1

Theory		ω_1 (Hertz)	ω_2 (Hertz)	ω_3 (Hertz)	ω_4 (Hertz)
Euler-Bernoulli	Analytical	25.76	123.32	271.04	461.16
	FEM	25.718	122.03	266.13	450.17
Timoshenko	Analytical	25.71	120.74	264.86	441.75
	FEM	25.641	118.63	257.54	425.64

Table 6.4. System's natural frequencies for a ring with thickness of h_2

Theory		ω_1 (Hertz)	ω_2 (Hertz)	ω_3 (Hertz)	ω_4 (Hertz)
Euler-Bernoulli	Analytical	81.72	341.54	790.19	1541.43
	FEM	79.457	331.06	762.67	1469.65
Timoshenko	Analytical	77.95	323.42	748.32	1446.29
	FEM	77.237	318.34	735.06	1416.90

Figures 6.7 through 6.8 investigate the convergence of the mesh by considering the total degrees of freedom (DOF) for both theories. Figure 6.9 provides a comparison of the convergence rates for both scenarios. Additionally, it illustrates that the Euler-Bernoulli model

anticipates higher natural frequencies when contrasted with the predictions from the Timoshenko model.

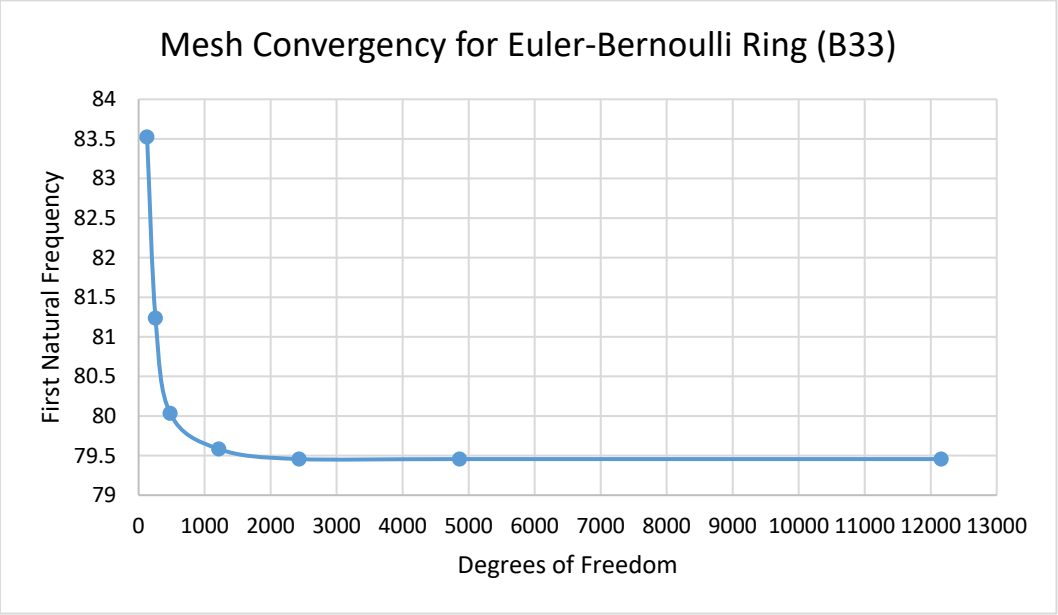

Fig. 6.7 *Mesh convergency for a ring with thickness of h_2*

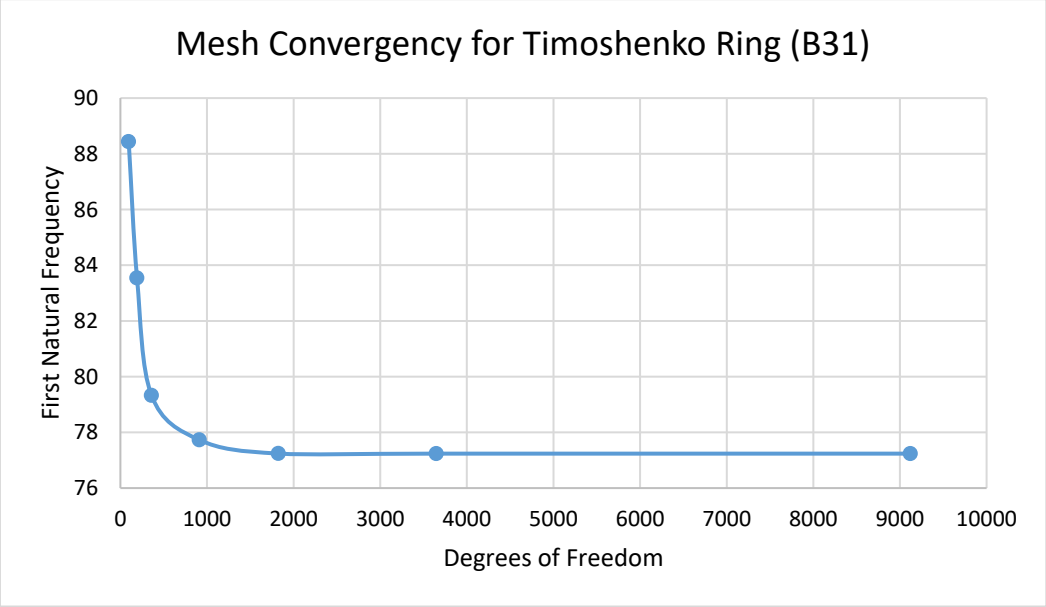

Fig. 6.7 *Mesh convergency for a ring with thickness of h_2*

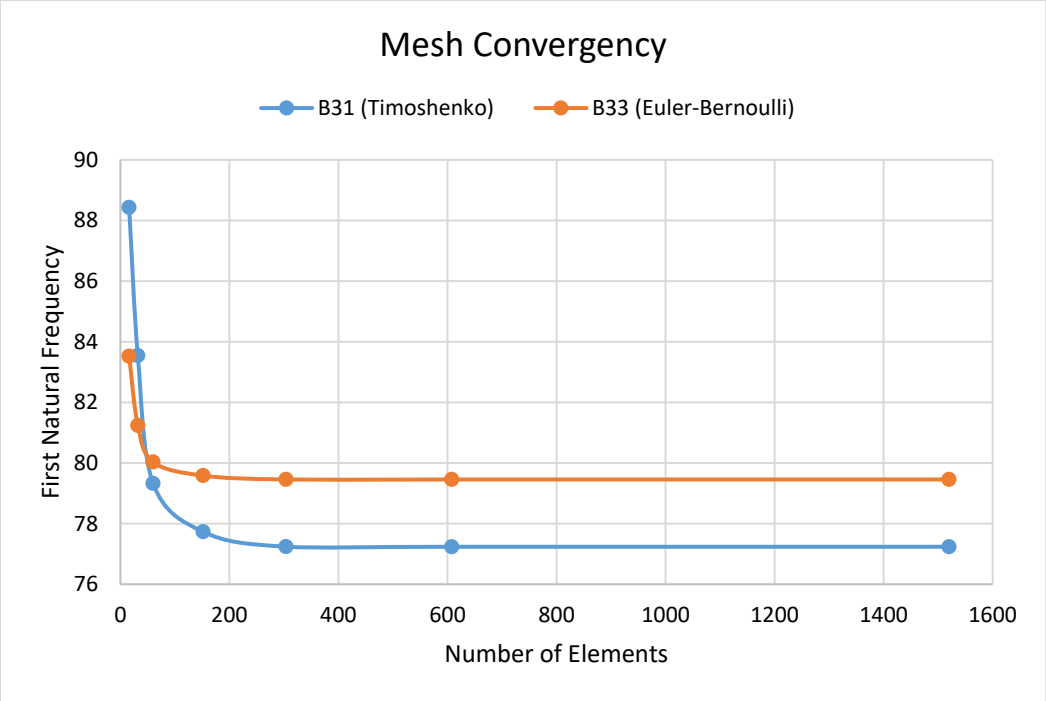

Fig. 6.8 *Mesh convergency for a ring with thickness of* h_2

Hence, the B33 beam element with dimensions of 0.005 (m) in all directions was implemented to adhere to the Euler-Bernoulli theory, whereas the B31 beam element with dimensions of 0.002 (m) in all directions was adopted for the Timoshenko theory.

Table 6.5 presents the percentage differences between the analytical and numerical results obtained from Abaqus for both theories.

Table 6.5. Percentage differences in system natural frequencies

Error %	h (m)	ω_1 (%)	ω_2 (%)	ω_3 (%)	ω_4 (%)
Euler-Bernoulli	0.008	0.163%	1.057%	1.845%	2.441%
	0.024	2.848%	3.166%	3.608%	4.884%

Timoshenko	0.008	0.269%	1.779%	2.842%	3.785%
	0.024	0.923%	1.596%	1.804%	2.074%

6.7 Conclusions

This chapter compares the Euler-Bernoulli and Timoshenko theories for a ring with general elastic boundary conditions. The findings presented in Tables 6.3 and 6.4 indicate that, for low natural frequencies, although the Euler-Bernoulli theory produces values closer to the FEM results compared to the Timoshenko theory, both theories can predict the system well. However, for higher frequencies, the Timoshenko theory exhibits greater accuracy when the thickness is increased. This can be attributed to the fact that, at low frequencies, the influence of shear deformation and rotary inertia is negligible. The results from Table 6.5 showed that while the Euler-Bernoulli theory holds true for lower frequencies, its accuracy diminishes as the thickness increases.

Through a comparison of both theories, it is crucial to recognize the need for caution when applying the Euler-Bernoulli assumptions. In the higher frequency range, neglecting the shear susceptibility and rotational inertia terms leads to significant discrepancies when compared to the more accurate Timoshenko model.

References

[1] R. Hoppe, The bending vibration of circular ring, Crelle Journal of Mathematics 73, pp. 158-168 (1871).

[2] A.E.H. Love, A treatise on the mathematical theory of elasticity. Cambridge University Press 4th edition (2013). ISBN-13: 978-1107618091.

[3] S.S. Rao, Vib. of continuous systems, (2019). https://doi.org/10.1002/9781119424284.

[4] D. Zhang, S. Wang, J. Liu, Analytical prediction for free response of rotationally ring-shaped periodic structures, Journal of Vibration and Acoustics, Transactions of the ASME. 136 (2014). https://doi.org/10.1115/1.4027630.

[5] P. Chidamparam, A.W. Leissa, Vibrations of planar curved beams, rings, and arches, Appl Mech Rev. 46 (1993). https://doi.org/10.1115/1.3120374.

[6] T.E. Lang, Vibration of Thin Circular Rings. Part II. Modal Functions and Eigenvalues of Constrained Semicircular Rings, Jet Propulsion Lab., California Inst. of Tech. Pasadena, USA (1962). Document ID: 19630006566.

[7] W. Lacarbonara, A. Arena, S.S. Antman, Flexural vibrations of nonlinearly elastic circular rings, Meccanica. 50 (2015). https://doi.org/10.1007/s11012-014-0038-3.

[8] X. Wu, R.G. Parker, Vibration of rings on a general elastic foundation, J Sound Vib. 295 (2006). https://doi.org/10.1016/j.jsv.2006.01.007.

[9] K. Singh, B.L. Dhoopar, Free vibration of circular rings on radial supports, J Sound Vib. 65 (1979). https://doi.org/10.1016/0022-460X(79)90521-2.

[10] F.M. Detinko, Free vibration of a thick ring on multiple supports, Int J Eng Sci. 27 (1989). https://doi.org/10.1016/0020-7225(89)90066-9.

[11] S.S. Rao, V. Sundararajan, In-plane flexural vibrations of circular rings, J. of Applied Mechanics, Transactions ASME. 36 (1964). https://doi.org/10.1115/1.3564726.

[12] K.B. Sahay, V. Sundararajan, Vibration of a stiffened ring considered as a cyclic structure, J Sound Vib. 22 (1972). https://doi.org/10.1016/0022-460X(72)90456-7.

[13] C.S. Chang, D.H. Hodges, Vibration characteristics of curved beams, J Mech Mater Struct. 4 (2009). https://doi.org/10.2140/jomms.2009.4.675.

[14] L. Domagalski, Comparison of the natural vibration frequencies of Timoshenko and Bernoulli periodic beams, Mater. 14 (2021). https://doi.org/10.3390/ma14247628.

[15] C.W. Lim, C.M. Wang, S. Kitipornchai, Timoshenko curved beam bending solutions in terms of Euler-Bernoulli solutions, Archive of Applied Mechanics. 67 (1997). https://doi.org/10.1007/s004190050110.

[16] P. Zhang, H. Qing, Free vibration analysis of Euler–Bernoulli curved beams using two-phase nonlocal integral models, JVC Journal of Vibration and Control. 28 (2022). https://doi.org/10.1177/10775463211022483.

[17] T. Li, J. Tang, Z. Hu, Z. Wang, Z. Fu, Three-dimensional vibration investigation of the thin web gear pair based on Timoshenko beam, Thin-Walled Structures. 184 (2023). https://doi.org/10.1016/j.tws.2022.110507.

[18] A.K. Mallik, D.J. Mead, Free vibration of thin circular rings on periodic radial supports, J Sound Vib. 54 (1977). https://doi.org/10.1016/0022-460X(77)90402-3.

[19] M.J. Abedinilaksar, J. Yang, Free Vibration Characteristics of a Thin-Walled Ring Under Different Boundary Conditions, (2020). https://doi.org/10.32393/csme.2020.1164.

[20] C.P. Filipich, M.B. Rosales, In-plane vibration of symmetrically supported circumferential rings, J Sound Vib. 136 (1990). https://doi.org/10.1016/0022-460X(90)90858-W.

[21] A.E. Zakrzhevskii, V.F. Tkachenko, V.S. Khoroshilov, Natural modes and frequencies of in-plane vibrations of a fixed elastic ring, International Applied Mechanics. 46 (2011). https://doi.org/10.1007/s10778-011-0436-3.

[22] J.S. Wu, F.T. Lin, H.J. Shaw, Free in-plane vibration analysis of a curved beam (arch) with arbitrary various concentrated elements, Appl Math Model. 37 (2013). https://doi.org/10.1016/j.apm.2013.02.029.

[23] J.S. Wu, L.K. Chiang, Free vibration of a circularly curved Timoshenko beam normal to its initial plane using finite curved beam elements, Comput Struct. 82 (2004). https://doi.org/10.1016/j.compstruc.2004.05.020.

[24] L.L. Philipson, On the Role of Extension in the Flexural Vibrations of Rings, J Appl Mech. 23 (1956). https://doi.org/10.1115/1.4011337.

[25] J. Henrych, The Dynamics of Arches and Frames, Elsevier Scientific Publishing Co., The Netherlands and New York, NY (1981), 350 pp, The Shock and Vibration Digest. 15. https://doi.org/10.1177/058310248301500406.

[26] M. Smith, ABAQUS/Standard User's Manual, Version 6.9, Abaqus Documentation, http://130.149.89.49:2080/v6.7/books/usb/default.htm?startat=pt06ch23s03ael13.html

[27] M. Smith, ABAQUS/Standard User's Manual, Version 6.9, Abaqus Documentation, https://classes.engineering.wustl.edu/2009/spring/mase5513/abaqus/docs/v6.6/books/usb/default.htm?startat=pt06ch23s03alm07.html

CHAPTER 7

In-plane Forced Vibration of a Thin-Walled Ring with Hinged Supports Undergoing Sinusoidal Moving Force

Authorship Statement.

A version of this chapter is under review for publication in the Journal of Sound and Vibration. As the first author, I developed the algorithm and performed numerical validation. Dr. James Yang, as the supervisor, proposed the concept, and reviewed the manuscript. Below is a concise summary outlining the declaration that identifies the authors of this work and describes the authors' contributions.

Javad Abedini: *Investigation, Methodology, Software, Writing - Original Draft, Review & Editing, Validation.*
James Yang: *Conceptualization, Methodology, Visualization, Supervision.*

Abstract – This study investigates the response of a uniform thin-walled ring subjected to a sinusoidal moving force. An example considered is a ring gear in a planetary gear train with four equally-spaced hinged supports. The excitation force moves along the circumference of the ring at a constant speed. A linear model is utilized, and the method of separation of variables is employed to derive the orthogonality relationship between the mode shapes and to solve the equations of motion. Due to the presence of multiple frequency excitations in the flexural in-plane vibrational equation, multiple resonant conditions coincide. Therefore, a parametric study is conducted to examine the relationship between the meshing and carrier rotational speed on the responses. Furthermore, the impact of the critical speed of the moving force is thoroughly investigated in this work. The study reveals that the maximum deflection for the centers of each segment occurs when the moving force exits that segment, rather than at the instant the force is at that point. The results obtained from the analytical method are validated using Abaqus simulations. This study provides valuable insights into the response of thin-walled rings subjected to a moving force and can be applied to various mechanical systems.

Keywords: Ring Vibration; Planetary Gear Train; Moving Force; Forced Vibration; Critical speed; Primary and Combined Instabilities.

7.1 Introduction

The study of the vibrations of rings holds great importance in a wide variety of engineering applications. Generally, analyzing the vibration of a thin-walled ring using beam theory is more complex compared to analogous problems involving straight beams. This complexity arises from the fact that, unlike straight beams, the structural deformations in a ring are dependent on rotational, radial, and coupled tangential displacements. Structures with ring geometry are utilized not only in mechanical systems such as bearings, rotors, and gears but also in interdisciplinary areas like bioengineering and vibration control. These structures are often treated as rings with elastic spring connections to the mating components.

The present study is motivated by Planetary Gear Trains (PGTs), in which the rotation of a planet gear applies a moving force to the ring gear. PGTs find widespread use in various applications, including helicopters, automobiles, wind turbines, automated guided vehicles, mobile satellite receivers, turbomachinery blades, and more. The ring gear in PGTs significantly influences the dynamics of the overall system, thus warranting a thorough investigation.

7.1.1 Elasticity of Ring Gears in PGT Dynamics

The ring gear in PGTs is generally designed to be thin in order to reduce the overall weight. This is advantageous for load sharing among the planet gears. However, it also leads to increased elastic deformation under the working load. Consequently, the impact on the dynamics of the thin-walled ring gear becomes significant. More importantly, the excitation force resulting from the planet-ring interaction constantly moves along the circumference,

thereby complicating the problem further. This aspect has been overlooked in the majority of literature, where the ring was modeled as a rigid body.

Thin-walled ring gears exhibit significant deformation with the increased flexibility. Numerous studies have been conducted to investigate the impact of ring gear elasticity on the dynamics of PGTs. Kahraman et al. [1-2] employed a semi-analytical approach to examine the effects of ring thickness. Their study investigated the stress, deflection, and load-sharing among the planets. The findings demonstrated that the elasticity of the ring gear has a substantial impact on load sharing among the components. Yong Hu et al. [3] conducted an analysis on the impact of the ring gear on the load distribution of PGTs. They found that the elasticity of the ring gear had a greater influence on the dynamics compared to other components. Their analysis also demonstrated that ring deformation significantly affected the meshing between the ring and planet gears, leading to changes in the load distribution of PGTs. In conclusion, it is essential to consider the elasticity of the ring gear in the dynamics of PGTs.

7.1.2 Different Approaches

Research on the vibration of rings (or curved beams) has been conducted using both analytical [4-6] and finite element methods [7-10]. However, analytical techniques appear to be more practical. Various approaches have been employed to investigate the effects of different constraints on rings. These include the complementary transfer matrix method [11], transfer matrix method [12, 13], Green's function [14], and wave approach [15], which have been utilized in previous studies.

7.1.3 Effects of Boundary Conditions

Rao and Sundararajan [16] conducted an analysis on a ring supported by rigid radial supports. In their study, the ring is divided into interconnected segments supported at both ends. However, this method is not suitable for cases with many supports. To address this limitation, Sahay and Sundararajan [14] proposed a method that can be applied to rings with multiple supports, albeit with the requirement of cyclic symmetry. In summary, there are numerous works in the literature regarding the vibration of rings on elastic foundations [11, 15-23]. These studies have examined the statics, dynamics, and stability of such systems. However, the majority of these works primarily focus on free vibration [11-12, 24-28], with only a limited number addressing forced vibration. Furthermore, in the research that specifically addresses forced vibrations, the loading was often modeled at a fixed location. However, this approach clearly oversimplifies the dynamics of the ring.

7.1.4 Moving Load

The dynamics of moving loads were initially acknowledged in the mid-19th century. One of the early studies on rings subjected to moving loads was conducted by Huang et al. [29]. They investigated a problem involving a harmonically varying moving load and compared the effects of a concentrated moving load versus a distributed load. They also calculated the percentage error that arises when assuming the distributed load as a point load. Zhao et al. [30] examined a ring-shaped structure and studied the parametric vibration of the system under the influence of a moving load. Similarly, Metrikine and Tochilin [31] examined the vibration of an elastic ring subjected to moving concentrated forces, to model train wheels. Forbes and Randall [32] investigated the response of a circular ring under a moving load. They classified their solutions

into three cases: magnitude-varying moving load, phase-varying moving load, and non-uniform continuous moving load. The ring model used in their study was unconstrained, allowing them to avoid the complexity caused by the boundary conditions. The effect of different supports on the ring's dynamics response was studied numerically by Taherikahnamouei and Yang [33]. Canchi and Parker [34-35] represented the interaction between ring-planet gears in a PGT by simulating the system as a circular ring with moving springs. They utilized numerical methods to investigate the parametric instabilities of in-plane bending vibrations, aiming to validate the analytical approach they studied. Their work focused on exploring the effects of various system parameters on the ring's instability boundaries. Similar to [32], the model used in [34-35] was unconstrained, without consideration of boundary conditions. Another relevant study on this topic was conducted by Abedinilaksar and Yang [23], who employed an analytical method to obtain precise solutions for the natural frequencies and associated mode shapes of a thin-walled ring under different boundary conditions. Notably, Ouyang [36] and Fryba [37] have extensively documented the works on dynamics of moving loads.

7.1.5 Gap in the Literature and Novelty of this Study

In spite of the aforementioned studies, the problem of the forced vibration of rings under a moving force is open. In particular, there is a scarcity of research on analytical methods and boundary conditions. This chapter aims to address this critical knowledge gap and examines the forced vibration behavior of the ring gear in a PGT when subjected to a sinusoidal meshing load resulting due to the interaction between the planet and ring gear. The primary focus is placed on the in-plane flexural vibration of the ring gear. In this investigation, the constraints imposed on the ring gear are represented by equally-spaced hinged supports along

the circumference. This research provides a pioneering analytical solution for the vibrational equation of a ring subjected to a moving force. It also compares deflections at critical points under non-moving and moving force conditions. Additionally, the study presents an equation to calculate the critical speed associated with the moving force and investigates its effects. The time variation of deflection at the critical point for different speeds relative to the critical speed of the rings is also examined.

This chapter is organized as follows: Section 7.1 provided a concise literature review. In Section 7.2, the dynamic model for the specific system under consideration is developed. This section focuses on deriving the in-plane vibrational equation and introducing the relevant boundary conditions. Section 7.3 explores the solution strategy, discussing a mathematical method to determine the system's natural frequencies and mode shapes. Section 7.4 presents a detailed analysis of moving force, including a discussion on the influences of critical speeds. In Section 7.5, the details about Abaqus simulation are provided. In Section 7.6, a case study is presented, where the simulation results obtained using the analytical method are compared with those obtained from the finite element method (FEM) using the Abaqus package. Finally, Section 7.7 draws the conclusion and summarizes the key findings of the study.

7.2 Dynamic Model

A standard single-stage PGT comprises a sun gear, a carrier, a ring gear, and several planet gears mounted on the carrier. The number of planet gears can vary, typically from three to five, depending on the specific application. In this study, for simplicity, only one planet gear

is considered. The model is expandable to include more planet gears if required, however, that will increase the complexity of the calculations.

Fig. 7.1 illustrates a thin-walled elastic ring hinged to a frame, while Fig. 7.2 depicts the centerline representing the motion of the ring within the plane. The force F represents the meshing force between the ring and planet gear (r-p), which rotates at a constant angular speed of the carrier, ω_c.

To develop a mathematical model, the following assumptions are made:

- The ring gear is simplified as a smooth ring with constant cross-section A, and bending rigidity EI.
- The effects of rotary inertia and shear deformations are neglected.
- The centerline of the ring remains inextensible.
- Supports are equally distributed circumferentially.

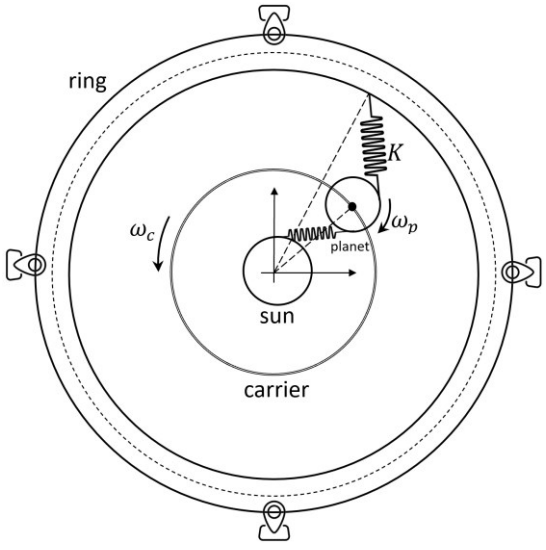

Fig. 7.1 *A thin-walled ring with hinged support*

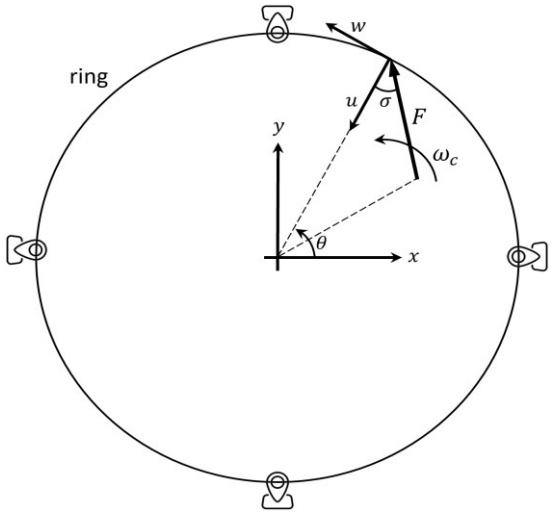

Fig. 7.2 *Mathematical model*

7.2.1 System Equations

The supports partition the ring into multiple segments, which are sequentially numbered for convenience, as shown in Fig. 7.3. A point on the centerline undergoes both a radial displacement (represented by u) and a tangential displacement (represented by w).

In order to obtain the equations of motion, a small section of the ring at an arbitrary angle "θ" is extracted and depicted in Fig. 7.4. The internal loads on this element include the normal force N, the shear force Q, and the in-plane bending moment M. The positive directions of those loads are as shown in Fig. 7.4.

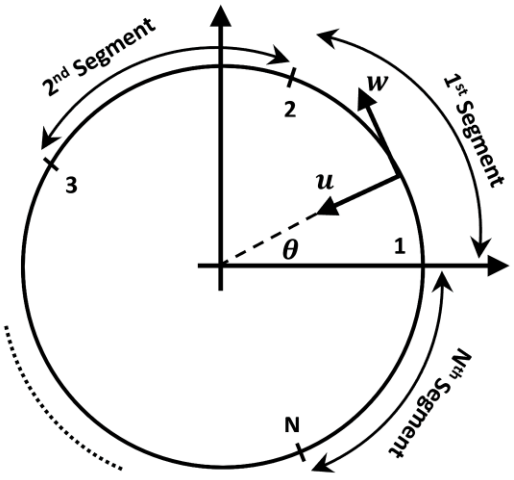

Fig. 7.3 *Ring segment*

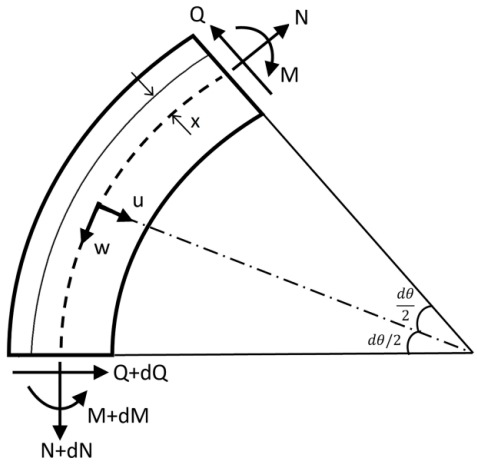

Fig. 7.4 *Ring element*

The force F represents the meshing force between the planet and ring gear, and can be assumed to follow a sinusoidal pattern, with the meshing frequency ω_m and a phase angle θ_0 as below.

$$F = F_{sh} + F_0 \cos(\omega_m t + \theta_0) \tag{7.1}$$

Where F_0 and F_{sh} are the meshing force amplitude and offset, respectively. The force F in Eq. (7.1), can be divided into its radial and tangential components. Eqs. (7.2) and (7.3) represent these relationships. The forces f and p, which are per unit length, sweep along the perimeter of the ring in a counter-clockwise direction at a constant angular speed of ω_c.

$$f = \frac{F}{\mathrm{R}} \cos(\sigma) \tag{7.2}$$

$$p = -\frac{F}{\mathrm{R}} \sin(\sigma) \tag{7.3}$$

where σ is the pressure angle.

Neglecting higher-order terms, the in-plane vibration equation of the ring can be expressed in the following form. The detailed derivation of this equation can be found in previous literature, such as [18].

$$\begin{aligned} &\frac{\partial^6 w(\theta,t)}{\partial\theta^6} + 2\frac{\partial^4 w(\theta,t)}{\partial\theta^4} + \frac{\partial^2 w(\theta,t)}{\partial\theta^2} + \frac{\mathrm{R}^4 \rho\, \mathrm{A}}{\mathrm{E\,I}} \frac{\partial^2}{\partial t^2}\left(\frac{\partial^2 w(\theta,t)}{\partial\theta^2} - w(\theta,t)\right) \\ &\qquad = \frac{\mathrm{R}^4}{\mathrm{E\,I}}\left(\frac{\partial f(\theta,t)}{\partial\theta} - p(\theta,t)\right)\delta(\theta - \omega_c t) \end{aligned} \tag{7.4}$$

where $w(\theta,t)$ is the tangential displacement of the ring centerline, R is the radius of the ring centerline, ρ is the mass density, A is the cross-sectional area, and I is the moment of inertia of the cross-sectional area A. The relationship between the strain ε and the displacements u and w is as below [18].

$$\varepsilon = \frac{1}{\mathrm{R}}\left(\frac{\partial w}{\partial\theta} - u - \frac{x^2}{\mathrm{R}^2}\frac{\partial}{\partial\theta}\left(w + \frac{\partial u}{\partial\theta}\right)\right) \tag{7.5}$$

where x is the distance from the ring centerline.

Given that the centerline is assumed inextensible, the following relation is held [20]:

$$u = \frac{\partial w}{\partial \theta} \tag{7.6}$$

Eq. (7.6) is called the inextensibility condition.

7.2.2 Boundary Conditions

The ring in the current research is attached to its frame at n equidistant points as shown in Fig. 7.3. The angle between two adjacent segments can be expressed as follows:

$$\zeta = \frac{2\pi}{n} \quad (rad) \tag{7.7}$$

Utilizing the u-w coordinate system depicted in Figs 7.2 and 7.3, the slope and bending moment of the ring can be represented by the second and third-order derivatives of the function *w(θ)*, respectively. For a hinged support, both tangential and radial displacements are zero *u*=*w*=0. In addition, the slope and moment are continuous across each support. Eqs. (7.8) through (7.11) represent this boundary condition.

$$u]_{\theta=\theta_s} = 0 \tag{7.8}$$

$$w]_{\theta=\theta_s} = 0 \tag{7.9}$$

$$\left.\frac{\partial^2 w}{\partial \theta^2}\right]_{\theta=\theta_s} = 0 \tag{7.10}$$

where θ_s is the location of the support.

7.3 Solution Strategy

7.3.1 Natural Frequencies

The solution for Eq. (7.4) can be expressed as the product of the mode shape function $\Psi(\theta)$ and the time-varying harmonic function $q(t)$, given by the following equation:

$$w(\theta,t) = \sum_{j=1}^{\infty} \Psi_j(\theta)\, \mathrm{q}_j(t) \tag{7.11}$$

$$\mathrm{q}_j(t) = D_j \exp(\hat{\imath}\omega_j t) \tag{7.12}$$

where $\hat{\imath}$ is the imaginary unit number $\hat{\imath} = \sqrt{-1}$. For simplicity, only the first order (j = 1) is considered throughout this chapter. Substituting Eq. (7.11) into Eq. (7.4) for free vibration gives:

$$\frac{\partial^6}{\partial\theta^6}\Psi(\theta)q(t) + 2\frac{\partial^4}{\partial\theta^4}\Psi(\theta)q(t) + \frac{\partial^2}{\partial\theta^2}\Psi(\theta)q(t) + \frac{\mathrm{R}^4 \rho\, \mathrm{A}}{\mathrm{E\ I}}\left[\frac{\partial^2\Psi(\theta)}{\partial\theta^2} - \Psi(\theta)\right]\ddot{q}(t) = 0 \tag{7.13}$$

Substituting Eq. (7.12) into Eq. (7.13) gives:

$$\left[\frac{\partial^6\Psi(\theta)}{\partial\theta^6} + 2\frac{\partial^4\Psi(\theta)}{\partial\theta^4} + \frac{\partial^2\Psi(\theta)}{\partial\theta^2}\right]\exp(\hat{\imath}\omega t) - \frac{\mathrm{R}^4 \rho\, \mathrm{A}\, \omega^2}{\mathrm{E\ I}}\left[\frac{\partial^2\Psi(\theta)}{\partial\theta^2} - \Psi(\theta)\right]\exp(\hat{\imath}\omega t) = 0 \tag{7.14}$$

The following must be true if Eq. (7.14) holds.

$$\frac{\partial^6\Psi(\theta)}{\partial\theta^6} + 2\,\frac{\partial^4\Psi(\theta)}{\partial\theta^4} + (1-\Omega^2)\frac{\partial^2\Psi(\theta)}{\partial\theta^2} + \Omega^2 = 0 \tag{7.15}$$

where:

$$\Omega = \mathrm{R}^2\sqrt{\rho\, \mathrm{A}\, /\mathrm{E\ I}}\,\omega \tag{7.16}$$

Assuming Eq. (7.11) has a solution of the following form:

$$\Psi(\theta) = \sum_{=1}^{6} A_i \, e^{\Upsilon_i \theta} = A_1 e^{\Upsilon_1 \theta} + A_2 e^{\Upsilon_2 \theta} + A_3 e^{\Upsilon_3 \theta} + A_4 e^{\Upsilon_4 \theta} + A_5 e^{\Upsilon_5 \theta} + A_6 e^{\Upsilon_6 \theta} \quad (7.17)$$

By employing the mathematical relationships between exponential and trigonometric functions, Eq. (7.17) can be alternatively expressed as follows:

$$\Psi(\theta) = X_1 \sin \Upsilon_1 \theta + Y_1 \cos \Upsilon_1 \theta + X_2 \sin \Upsilon_2 \theta + Y_2 \cos \Upsilon_1 \theta + X_3 \sin \Upsilon_3 \theta + Y_3 \cos \Upsilon_3 \theta \quad (7.18)$$

where the amplitudes X_i and Y_i (i=1-3) can be computed from the system of homogeneous equations based on the system's boundary conditions.

By applying the boundary conditions specified in Eqs. (7.8) through (7.10) at each support, a system of equations is obtained. Solving this system determines the natural frequencies. The detailed explanation of this process can be found in Section 4.3 of Chapter 4, as well as [23].

7.3.2 Orthogonality Relationship

To establish the orthogonality relationships for the mode shapes, it is necessary to formulate the governing equation of the system for two distinct modes, denoted as i and j. The following set of equations illustrates this process.

$$\frac{\partial^6 \Psi_i(\theta)}{\partial \theta^6} + 2\frac{\partial^4 \Psi_i(\theta)}{\partial \theta^4} + \frac{\partial^2 \Psi_i(\theta)}{\partial \theta^2} = \frac{\mathrm{R}^4 \rho \mathrm{A}}{\mathrm{EI}} \, {\omega_i}^2 \left(\frac{\partial^2 \Psi_i(\theta)}{\partial \theta^2} - \Psi_i(\theta) \right) = 0 \quad (7.19)$$

$$\frac{\partial^6 \Psi_j(\theta)}{\partial \theta^6} + 2\frac{\partial^4 \Psi_j(\theta)}{\partial \theta^4} + \frac{\partial^2 \Psi_j(\theta)}{\partial \theta^2} = \frac{\mathrm{R}^4 \rho \mathrm{A}}{\mathrm{EI}} \, {\omega_j}^2 \left(\frac{\partial^2 \Psi_j(\theta)}{\partial \theta^2} - \Psi_j(\theta) \right) = 0 \quad (7.20)$$

Eq. (7.19) needs to be multiplied by an arbitrary distinct mode, such as $\Psi_j(\theta)$ and subsequently integrated over the entire perimeter of the ring. The resulting calculation is presented below.

$$\int_0^{2\pi} \frac{\partial^6 \Psi_i(\theta)}{\partial \theta^6} \Psi_j(\theta) d\theta + 2\int_0^{2\pi} \frac{\partial^4 \Psi_i(\theta)}{\partial \theta^4} \Psi_j(\theta) d\theta + \int_0^{2\pi} \frac{\partial^2 \Psi_i(\theta)}{\partial \theta^2} \Psi_j(\theta) d\theta = \frac{\mathrm{R}^4 \rho \mathrm{A}}{\mathrm{EI}} \omega_i{}^2 \int_0^{2\pi} \left(\frac{\partial^2 \Psi_i(\theta)}{\partial \theta^2} \Psi_j(\theta) - \Psi_i(\theta) \Psi_j(\theta) \right) d\theta \tag{7.21}$$

Each integral in Eq. (7.21) can be divided into n definite integrals corresponding to the length of each segment between consecutive supports.

$$\int_{\theta_s}^{\theta_s + 2\pi} H_k(\theta)\, d\theta = \sum_{i=1}^{n} \left(\int_{\theta_{si}}^{\theta_{si} + \zeta} H_k(\theta)\, d\theta \right) \tag{7.22}$$

where $H_k(\theta)$ corresponds to various functions existing in Eq. (7.21) such as $\frac{\partial^6 \Psi_i(\theta)}{\partial \theta^6}\, \Psi_j(\theta)$, or $\frac{\partial^4 \Psi_i(\theta)}{\partial \theta^4}\, \Psi_j(\theta)$ and so on.

For instance, in the scenario where there are four equally-spaced hinged supports, each integral in Eq. (7.22) can be subdivided into four individual integrals, as shown below:

$$\int_0^{2\pi} H_k(\theta)\, d\theta = \int_0^{\pi/2} H_k(\theta)\, d\theta + \int_{\pi/2}^{\pi} H_k(\theta)\, d\theta + \int_{\pi}^{3\pi/2} H_k(\theta)\, d\theta + \int_{3\pi/2}^{2\pi} H_k(\theta)\, d\theta \tag{7.23}$$

In total, there will be 20 integrals that need to be simplified individually using the chain rule for integration. Once all of these integrals have been simplified, the corresponding boundary conditions can be applied.

Similarly, the same steps need to be applied for the arbitrary jth mode. Therefore, both sides of Eq. (7.20) should be multiplied by a distinct mode $\Psi_i(\theta)$ and then integrated over the perimeter of the ring.

By carefully analyzing and comparing the results derived from the calculations described above, it becomes apparent that the left-hand sides of the equations yield identical expressions. As a consequence, it can be concluded that the right-hand sides of these equations must also be equal. By equating the right-hand sides, the orthogonality relationship between any two arbitrary distinct modes of the system can be established. This significant relationship is presented below in Eq. (7.24).

$$\left({\omega_j}^2 - {\omega_i}^2\right) \int_0^{\theta_f} \left(\frac{\partial \Psi_i(\theta)}{\partial \theta} \frac{\partial \Psi_j(\theta)}{\partial \theta} + \Psi_i(\theta)\Psi_j(\theta) \right) d\theta = 0 \tag{7.24}$$

This orthogonality relationship can be alternatively represented as follows:

$$\int_0^{\theta_f} \left(\frac{\partial \Psi_i(\theta)}{\partial \theta} \frac{\partial \Psi_j(\theta)}{\partial \theta} + \Psi_i(\theta)\Psi_j(\theta) \right) d\theta = \delta_{ij} = \begin{cases} 0 & i \neq j \\ 1 & i = j \end{cases} \tag{7.25}$$

For the case of i=j, Eq. (7.25) can be simplified to:

$$\int_0^{\theta_f} \left(\frac{\partial \Psi_i(\theta)}{\partial \theta} \frac{\partial \Psi_i(\theta)}{\partial \theta} + \Psi_i(\theta)\Psi_i(\theta) \right) d\theta = 1 \tag{7.26}$$

7.4 Moving Force Analysis

The in-plane vibrational equation for a thin-walled ring, as expressed in Eq. (7.4), includes a term represented by the Dirac delta function. This function in Eq. (7.4) signifies that

both normal and tangential forces propagate along the ring at a constant angular velocity of ω_c. The mathematical definition of the Dirac delta function is illustrated in Eq. (7.27).

$$\delta(t) = \begin{cases} 0 & t \neq 0 \\ \infty & t = 0 \end{cases} \tag{7.27}$$

The Dirac delta function has the following two characteristics outlined in Eqs. (7.28) and (7.29).

$$\int_{t_1}^{t_2} \delta(t)\, dt = 1 \tag{7.28}$$

$$\int_0^{\overline{\theta}} g(\theta)\delta(\theta - \zeta)\, d\theta = g(\zeta) \tag{7.29}$$

On the other hand, the following transformation can be derived assuming the constant angular velocity of the carrier ring ω_c remains constant.

$$\frac{\partial f}{\partial \theta} = \frac{\partial f}{\partial t}\frac{\partial t}{\partial \theta} = \frac{\partial f}{\partial t}\frac{1}{\omega_c} = \frac{\dot{f}}{\omega_c} \tag{7.30}$$

Plugging Eq. (7.11) and (7.30) into Eq. (7.4) will result in:

$$\begin{aligned} &\sum_{j=1}^{\infty} \frac{\partial^6 \Psi_j(\theta)}{\partial \theta^6} \mathrm{q}_j(t) + 2\sum_{j=1}^{\infty} \frac{\partial^4 \Psi_j(\theta)}{\partial \theta^4} \mathrm{q}_j(t) + \sum_{j=1}^{\infty} \frac{\partial^2 \Psi_j(\theta)}{\partial \theta^2} \mathrm{q}_j(t) + \\ &\frac{\mathrm{R}^4 \rho \mathrm{A}}{\mathrm{EI}} \sum_{j=1}^{\infty} \frac{\partial^2 \Psi_j(\theta)}{\partial \theta^2} \ddot{\mathrm{q}}_j(t) - \frac{\mathrm{R}^4 \rho \mathrm{A}}{\mathrm{EI}} \sum_{j=1}^{\infty} \Psi_j(\theta) \ddot{\mathrm{q}}_j(t) = \frac{\mathrm{R}^4}{\mathrm{EI}} \left(\frac{\dot{f}}{\omega_c} - p\right) \delta(\theta - \omega_c t) \end{aligned} \tag{7.31}$$

In this step, it is necessary to multiply both sides of Eq. (7.31) by a distinct mode shape, such as $\Psi_k(\theta)$, and subsequently integrate over each segment length. This modification is demonstrated below.

$$\int_0^{\theta_f} \sum_{j=1}^{\infty} \Psi_k(\theta) \frac{\partial^6 \Psi_j(\theta)}{\partial \theta^6} \mathrm{q}_j(t) d\theta + 2 \int_0^{\theta_f} \sum_{j=1}^{\infty} \Psi_k(\theta) \frac{\partial^4 \Psi_j(\theta)}{\partial \theta^4} \mathrm{q}_j(t) d\theta +$$

$$\int_0^{\theta_f} \sum_{j=1}^{\infty} \Psi_k(\theta) \frac{\partial^2 \Psi_j(\theta)}{\partial \theta^2} \mathrm{q}_j(t) d\theta + \frac{\mathrm{R}^4 \rho \mathrm{A}}{\mathrm{EI}} \int_0^{\theta_f} \sum_{j=1}^{\infty} \Psi_k(\theta) \frac{\partial^2 \Psi_j(\theta)}{\partial \theta^2} \ddot{\mathrm{q}}_j(t) d\theta - \tag{7.32}$$

$$\frac{\mathrm{R}^4 \rho \mathrm{A}}{\mathrm{EI}} \int_0^{\theta_f} \sum_{j=1}^{\infty} \Psi_k(\theta) \Psi_j(\theta) \ddot{\mathrm{q}}_j(t) d\theta = \frac{\mathrm{R}^4}{\mathrm{EI}} \int_0^{\theta_f} \Psi_k(\theta) \left(\frac{\dot{f}}{\omega_c} - p \right) \delta(\theta - \omega_c t) d\theta$$

Following the methodology described in Section 7.3.2, the left-hand side of Eq. (7.32) can be simplified to:

$$\mathrm{LHS}_k = \frac{\mathrm{R}^4 \rho \mathrm{A}}{\mathrm{EI}} (\ddot{q}_k + {\omega_k}^2 \mathrm{q}_k) \tag{7.33}$$

Similarly, the right-hand side of Eq. (7.32) can be simplified and expressed as follows:

$$\mathrm{RHS}_k = \frac{R^4}{EI} \int_0^{\theta_f} \Psi_k(\theta) \left(-\frac{\omega_m \mathrm{F}_0 \cos\sigma}{\omega_c} \sin(\omega_m t + \theta_0) + F_{sh} \sin\sigma + F_0 \sin\sigma \cos(\omega_m t + \theta_0) \right) \delta(\theta - \omega_c t) d\theta \tag{7.34}$$

The integral in Eq. (7.34) can be eliminated by using the Dirac delta property expressed in Eq. (7.29). The result is presented below.

$$\mathrm{RHS}_k = \frac{R^4}{EI} \Psi_k(\omega_c t) \left(F_{sh} \sin\sigma + F_0 \left(-\frac{\omega_m}{\omega_c} \cos\sigma \sin(\omega_m t + \theta_0) + \sin\sigma \cos(\omega_m t + \theta_0) \right) \right) \tag{7.35}$$

By replacing $\Psi_k(\theta)$ from Eq. (7.18) into Eq. (7.35) and equating the results to Eq. (7.33), the following equation can be derived. Notably, Eq. (7.36) exhibits three distinct exciting phases, each contributing to the overall behavior of the system. These exciting phases are presented individually in Eqs. (7.44) through (7.46), providing a thorough understanding of

their respective influences. Solving Eq. (7.36) will yield the response of the system for any specific point at any desired time.

$$\ddot{q}_k + {\omega_k}^2 \mathrm{q}_k = Q_{0_k}\sin\left(P_{0_k}t\right) + Q_{0_k}\cos\left(P_{0_k}t\right) + Q_{1_k}\cos\left(P_{1_k}t\right) + Q_{2_k}\sin\left(P_{1_k}t\right) + Q_{3_k}\cos\left(P_{2_k}t\right) + Q_{4_k}\sin\left(P_{2_k}t\right) \tag{7.36}$$

where:

$$G_k = -\sqrt{\frac{2}{k^2+1}}\frac{\omega_m \cos(\sigma)\ F_0}{\omega_c\ \rho\ \mathrm{A}\sqrt{\theta_\mathrm{f}}} \tag{7.37}$$

$$W_k = \sqrt{\frac{2}{k^2+1}}\frac{\sin(\sigma)\ F_0}{\rho\ \mathrm{A}\sqrt{\theta_\mathrm{f}}} \tag{7.38}$$

$$Q_{0_k} = \sqrt{\frac{2}{k^2+1}}\frac{F_{sh}}{\rho\ \mathrm{A}\sqrt{\theta_\mathrm{f}}} \tag{7.39}$$

$$Q_{1_k} = \frac{G_k}{2}(\sin(\theta_0) + \cos(\theta_0)) + \frac{W_k}{2}(\cos(\theta_0) - \sin(\theta_0)) \tag{7.40}$$

$$Q_{2_k} = \frac{G_k}{2}(\cos(\theta_0) - \cos(\theta_0)) - \frac{W_k}{2}(\cos(\theta_0) + \sin(\theta_0)) \tag{7.41}$$

$$Q_{3_k} = \frac{G_k}{2}(\sin(\theta_0) - \cos(\theta_0)) + \frac{W_k}{2}(\cos(\theta_0) + \sin(\theta_0)) \tag{7.42}$$

$$Q_{4_k} = \frac{G_k}{2}(\sin(\theta_0) + \cos(\theta_0)) + \frac{W_k}{2}(\cos(\theta_0) - \sin(\theta_0)) \tag{7.43}$$

$$P_{0_k} = \frac{k\ \omega_c\ \pi}{\theta_\mathrm{f}} \tag{7.44}$$

$$P_{1_k} = \omega_m - \frac{k\,\omega_c\,\pi}{\theta_f} \tag{7.45}$$

$$P_{2_k} = \omega_m + \frac{k\,\omega_c\,\pi}{\theta_f} \tag{7.46}$$

In order to solve Eq. (7.36), the adaptive step-size Runge-Kutta-Fehlberg method (RK45) from the Maple package is utilized to numerically integrate the ODE and approximate the solution. Subsequently, this solution can be substituted into Eqs. (7.11) and (7.6) to determine the deflections in the tangential and radial directions, respectively.

7.4.1 Critical angular speed

One important issue involving a moving force is the determination of its critical speed. The critical speed refers to the speed at which the system resonates, leading to significant deflections of the ring structure, posing a potential risk of damage or failure. Therefore, accurately identifying and understanding the critical speed is crucial for ensuring the structural integrity and safe operation of the system.

To ascertain the critical speed for this system, an adjustment is needed to the method proposed for straight beams in [36]. The lowest critical angular speed associated with the first natural frequency of the system can be obtained by equating the exciting frequency derived from Eqs. (7.44) through (7.46) to a representative natural frequency. Among these equations, Eq. (7.46) yields the lowest critical speed and is shown below:

$$\omega_m + \frac{k\,\omega_{cr}\,\pi}{\theta_f} = \omega_n \tag{7.47}$$

By solving Eq. (7.47) for k=1, the lowest critical speed for the system as given in Eq. (7.48) can be determined.

$$\omega_{cr_1} = \frac{(\omega_n - \omega_m)\,\theta_f}{\pi} \tag{7.48}$$

To analyze the critical speed, the first step involves selecting the critical points of the structure, followed by studying the deflections at those points. In the current model, the critical points are identified as the midpoints of each segment. The deflection for the midpoint of each segment can be computed as shown below using the Pythagorean theorem:

$$\Delta_{mid} = \sqrt{{u_{mid}}^2 + {w_{mid}}^2} \tag{7.49}$$

7.5 Finite Element Analysis

7.5.1 Element Type and Material Direction

In order to confirm the accuracy of certain analytical findings of this chapter, a thin-walled ring has been simulated in Abaqus, as shown in Fig 7.5. The simulation employs a 3D model using C3D20 mesh elements. The C3D20 element is a 20-node quadratic brick element that surpasses the C3D8 element (an 8-node linear brick element) in terms of accuracy by incorporating additional nodes, thus providing a more refined representation of the geometry. This element type is suitable for tackling problems that demand enhanced precision, such as non-linear material behavior, complex contact scenarios, and moving forces. Opting for C3D20

over C3D8 is also influenced by its quicker convergence in results, resulting in the attainment of outcomes using fewer mesh elements.

Unlike the earlier chapters that utilized 2D elements, this section employs 3D elements to facilitate the application of a moving load. This approach aids in the incorporation of the delta function within the model's subroutine code by establishing a region where the moving load is implemented.

Fig. 7.6 illustrates the local cylindrical coordinate system, where axis 1 and axis 2 correspond to deflections in the radial and tangential directions, respectively. It is worth noting that in the Abaqus model, the orientation of the radial axis is opposite to that depicted in Figs. 7.2 and 7.3, which were used to derive the system equations.

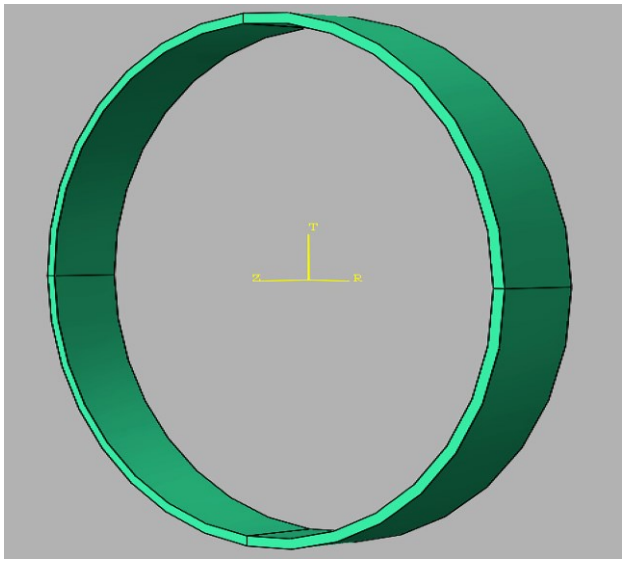

Fig. 7.5 *Thin-walled ring modelled in Abaqus*

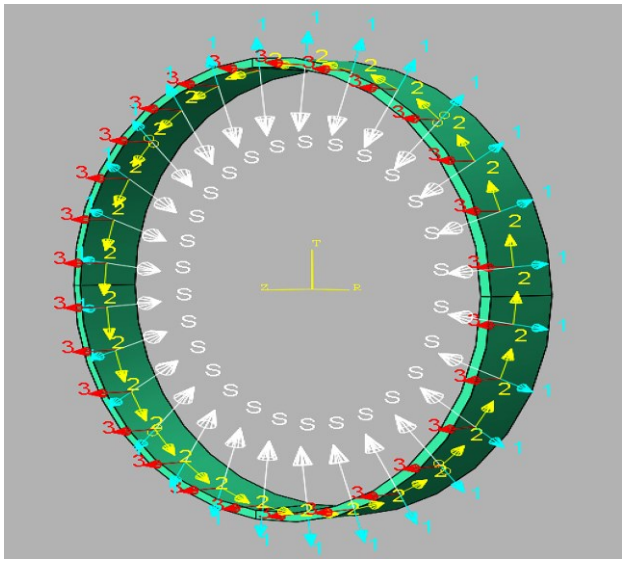

Fig. 7.6 *Material directions in Abaqus*

7.5.2 Moving Force

There are multiple methods available for modeling a moving force in Abaqus; however, each of them has certain flaws. One of the most common approaches, albeit more complex than others, involves using subroutine coding within Abaqus. Abaqus user subroutines enable customization of Abaqus for specific applications that are not supported by the main Abaqus functionalities. When dealing with moving-force problems, the loading cannot be directly defined using the built-in models provided by Abaqus. Therefore, in this study, the user subroutine DLOAD has been employed to model the moving force. The DLOAD subroutine allows for the specification of the variation in the magnitude of the load as a function of position, time, and velocity.

In this particular case, the loading involves a distributed pressure applied to the internal surface of the ring. Within the subroutine code, a specific section of the inner ring has been delineated to translate this pressure into a load configuration that satisfies Eq. (7.31). Researchers interested in further details are advised to study the Abaqus Documentation for comprehensive information [38].

7.5.3 Mesh Size

Mesh convergence is the iterative procedure of enhancing the finite element mesh to ensure precise and dependable outcomes in numerical simulations. The analysis of mesh convergence involves progressively augmenting the mesh density and evaluating the alterations in the computed solution. Fig. 7.7 visually demonstrates the mesh convergence trend as the total degrees of freedom (DOF) within the model progressively rise

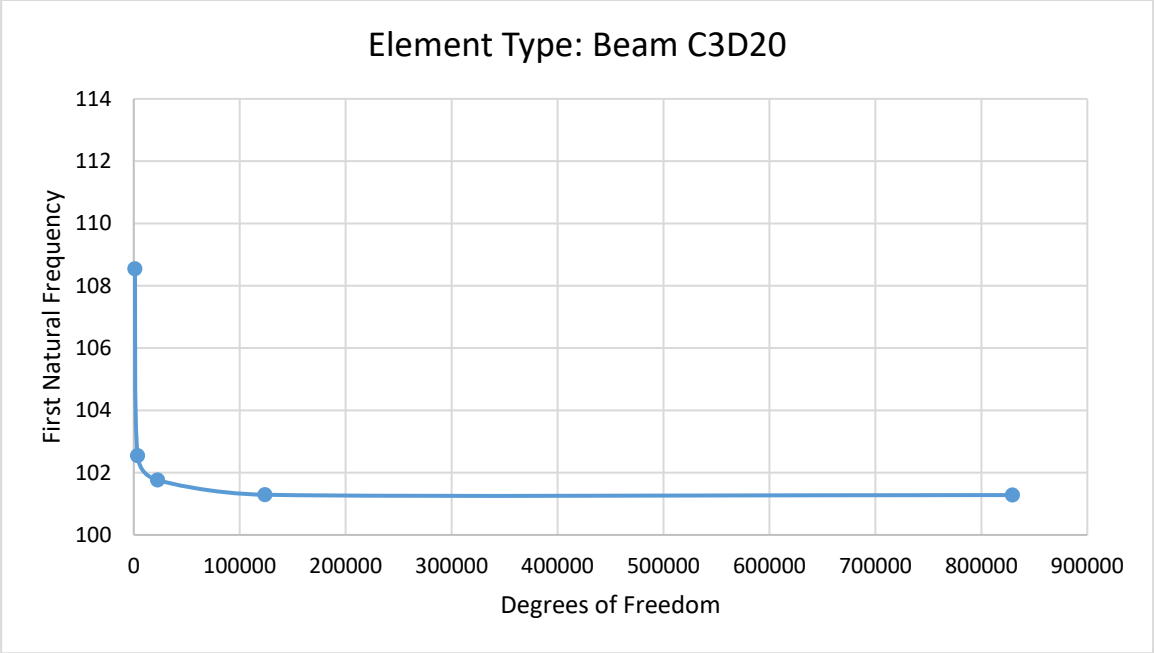

Fig. 7.7 *Mesh convergency for a thin-walled ring with four hinged supports*

Adjusting the mesh size in different dimensions can effectively improve processing time while maintaining result accuracy. The analysis of mesh convergence, as depicted in Fig. 7.7, facilitated a methodical enhancement of the mesh for the ring model in every dimension. Consequently, the current model's ring structure was meshed according to the pattern indicated in Fig. 7.8, employing distinct sizes tailored to individual dimensions. This approach led to the selection of mesh dimensions of 0.002 m, 0.01 m, and 0.02 m for the thickness, width, and perimeter of the ring, respectively.

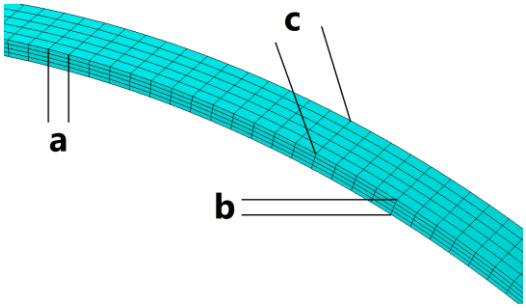

Fig. 7.8 *The recommended mesh dimensions determined from the mesh convergence analysis*

7.5.4 Analysis Method

The selected technique for conducting this simulation is the implicit dynamic method. The implicit dynamic is particularly suited for problems where the time scale of interest is relatively long compared to the natural frequencies of the structure or material being analyzed. Implicit dynamics is also known as the direct integration or implicit time integration method. In this case, equilibrium is enforced between externally applied load and internally generated reaction forces at every solution step (Newton Raphson method). In an implicit dynamics analysis, the equations of motion are integrated numerically over time using an implicit time-stepping algorithm. Unlike explicit dynamics, where the time step is typically limited by stability and accuracy considerations, implicit dynamics allows for larger time steps because it inherently considers the effects of inertia and damping over a larger time interval.

Implicit dynamics uses backward differencing or Newmark time integration schemes, which consider both the current and future displacements and velocities when calculating the forces and accelerations. This makes it numerically stable for larger time steps. Hence, the selection of the right time increment holds paramount importance. To achieve this, the system's highest natural frequency is identified, and the corresponding minimum time period is computed using the connection between natural frequency and time period, expressed as $\omega_{max} = 2\pi/T_{min}$. Consequently, for this scenario, the analysis time increment is set at 10% of the system's minimum time period.

7.6 Case Study

In this section, a thin-walled ring with a rectangular cross-section is investigated. The ring is mounted at four equally spaced points. The parameters pertaining to the ring and its supports are provided in Table 7.1.

Table 7.1. Parameters of a thin-walled ring

Definition		Value	Unit
Outer radius of ring	R_o	0.520	m
Inner radius of ring	R_i	0.500	m
Ring density	ρ	7800	kg/m^3
Ring thickness	t	0.020	m
Face width of ring	b	0.110	m
Young's modulus	E	410	GPa
Carrier rotational speed	ω_c	12.57	rad/s
Meshing force speed	ω_m	22	rad/s
Meshing force amplitude	F_0	50	N
Meshing force offset	F_{sh}	75	N
Meshing force phase angle	θ_0	0	rad
Pressure angle	σ	24.6	deg

7.6.1 Natural Frequencies and Mode Shapes

The first four natural frequencies of the system are computed using the methodology outlined in Section 7.3 and are listed in Table 7.2. A comparison is made between these results and the findings from previous research [25] as well as the Abaqus simulation.

Table 7.2. System natural frequencies

Method	ω_1 (Hertz)	ω_2 (Hertz)	ω_3 (Hertz)	ω_4 (Hertz)
Current work	98.26	222.64	532.06	628.20
[25]	96.63	237.25	583.83	847.62
Abaqus	101.28	226.63	545.28	667.15

The results presented in Table 7.2 indicate that for low natural frequencies, the results obtained using the current method aligns with previous research [25] and FEM. However, for higher frequencies, the method employed in this study exhibits closer agreement with FEM results compared to [25]. This disparity can be attributed to the use of an approximation formulation for natural frequencies in [25].

7.6.2 Critical Speed

In Fig. 7.9, the variation of maximum mid-point deflection with the carrier's angular speed, calculated using Eq. (7.49), is presented. Notably, certain peaks marked as A through G indicate resonance points in the system.

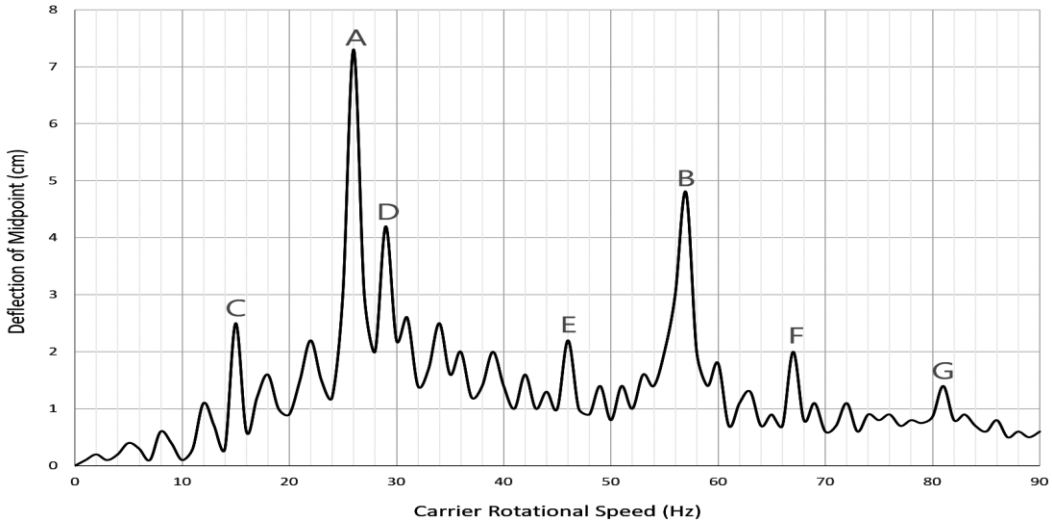

Fig. 7.9 *Critical velocity analysis for the moving force*

To assess the accuracy of the proposed method, a comparison is made between the carrier's angular speeds at these resonance points and the critical speeds obtained using Eq. (7.48). The results, presented in Table 7.3, exhibit an agreement between the results, validating the proposed approach.

Table 7.3. Validating the critical speeds

Peak	ω_c (Hz) Fig. 7.16	ω_{cr} (Hz) Eq. (7.49)	Error (%)
A	**25**	$\boldsymbol{\omega_{cr1} = 23.69}$	**5.53**
B	**57**	$\boldsymbol{\omega_{cr2} = 54.78}$	**4.05**

C	14	$\omega_{cr1}/2 = 12.28$	14.00
D	29	$\omega_{cr2}/2 = 27.83$	4.20
E	46	$\omega_{cr3}/3 = 44.33$	3.76
F	60	$\omega_{cr3}/2 = 66.51$	9.79
G	81	$\omega_{cr4}/2 = 78.52$	3.16

In Fig. 7.10, the time-dependent deflection at the center of a segment is presented for three distinct carrier speeds: below the critical speed, near the critical speed, and above the critical speed.

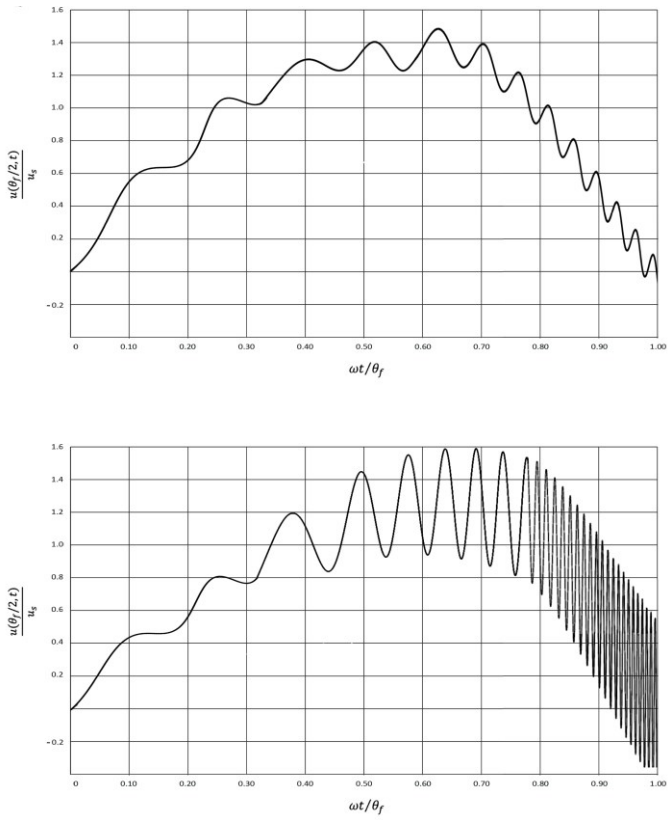

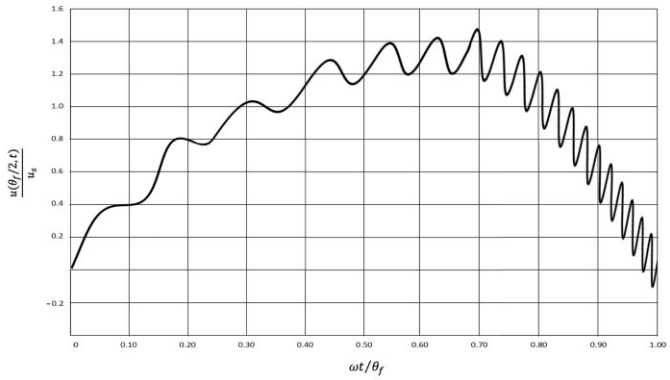

Fig. 7.10 *Time variation of the deflection of a mid-segment for three different speeds: a (top): $\omega_c < \omega_{cr}$, b (middle): $\omega_c \approx \omega_{cr}$, and c (bottom): $\omega_c > \omega_{cr}$*

As depicted in Fig. 7.10, it is evident that the response at speeds near the critical speed is significantly higher compared to the other two cases. This observation can be attributed to the system entering a resonance state at the critical speed, causing the response to increase substantially. Observing Fig. 7.10, it becomes evident that in order to maintain system stability, it is crucial to avoid operating the moving force at or near the critical speeds.

7.6.3 Dynamic Coefficient

In practical applications, the dynamic coefficient is commonly defined as the ratio between the dynamic deflection and the static deflection at the midpoint of a ring segment.

$$\mu = \frac{u\left(\theta_f/2, t\right)}{u_s} \tag{7.50}$$

Eq. (7.50) is derived under the assumption that the ring is simultaneously subjected to both constant and harmonic terms described in Eq. (7.11). The maximum deflection of the first component of motion at the mid-segment $\theta = \theta_f/2$ of the ring is denoted as u_s representing the deflection when the force passes over the center of the beam. Fig. 7.11 illustrates the temporal

variation of the deflection at the center of a segment bridge, traversed by a harmonic force with an angular speed of 2 Hz. The computation is performed according to the theory explained in Section 7.4. The vertical axis represents the ratio of the dynamic deflection to the static deflection, while the horizontal axis displays the ratio of the positions of all points of the segment to the location of the midpoint.

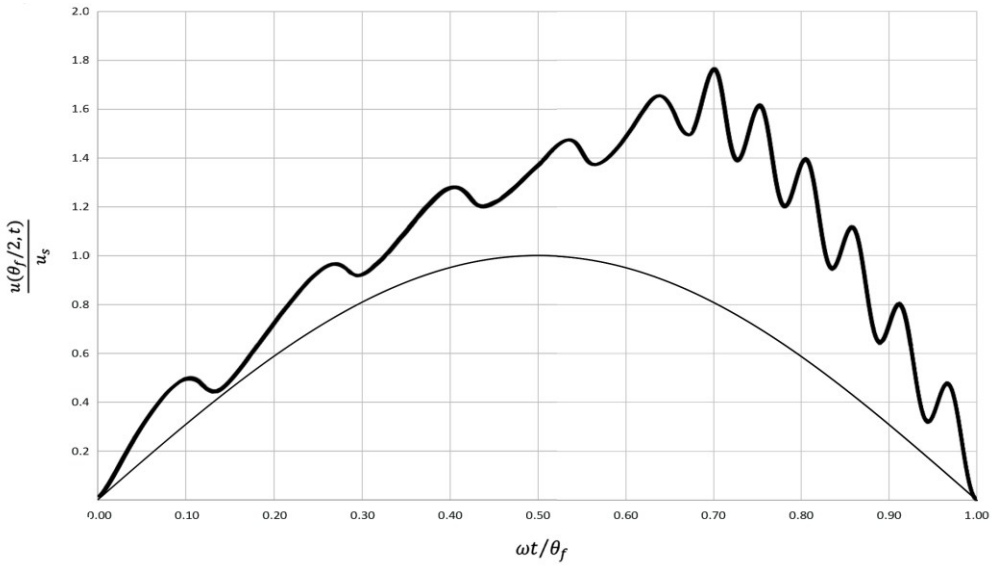

Fig. 7.11 *Time variation of the deflection of a mid-segment*

Fig. 7.11 reveals that the highest dynamic deflection caused by the movement of the harmonic force takes place when the force has moved past the center of the segment. This graph provides a significant finding, demonstrating that the maximum deflection of critical points in the rings occurs when the moving force is positioned near the end of the segment, rather than at the center.

7.6.4 Moving vs. Non-moving Force

Fig. 7.12 presents a comparison of the deflection at a specific critical point in the system under two scenarios:

a. When the periodic meshing force is positioned at the critical point without any movement. The solid line represents the corresponding deflections.

b. When the periodic meshing force is in motion counterclockwise with a constant angular velocity of 3.5 rad/s. The dotted line represents the deflections in this case.

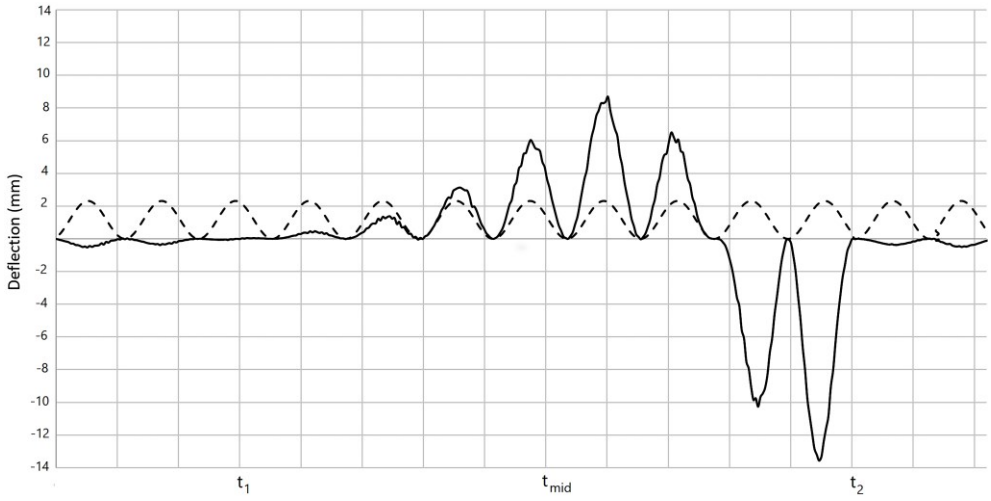

Fig. 7.12 *Comparison between motions for moving and non-moving force cases*

The findings from Fig. 7.12 lead to the conclusion that the deflection of the ring becomes significantly more noticeable when the force is in motion. It is evident that static analysis of PGTs, without considering the influence of the moving force, fails to provide acceptable results in capturing the system's behavior accurately.

7.6.5 Parametric Excitation

In cases involving multiple frequency excitations, such as Eq. (7.36), it is possible for more than one resonant condition to occur simultaneously. As a result, various combinations of natural frequencies can manifest concurrently. This chapter focuses specifically on the primary resonance of the system; however, it is important to acknowledge the existence of numerous resonance cases. The excitation described in Eq. (7.36) falls into the category of parametric excitations. In this category, even a small parametric excitation can generate a significant response when the excitation frequency closely aligns with the summation or combination of the structure's natural frequencies. Thus, resonance can be induced not only by the carrier speed ω_c but also by a combination of ω_c and ω_m, as evident in Eqs. (7.44) through (7.46). Exploring this phenomenon, a detuning parameter can be defined, and the system stability can be investigated, although that is not the primary focus of this work.

7.7 Conclusions

In this chapter, a thorough approach is presented for evaluating the dynamic responses of a PGT's ring subjected to a moving force resulting from the interaction between the planet and ring gears. The PGT ring in this study is treated as a cyclically symmetric structure secured at four equidistant points within its frame. The analysis conducted in this work examines the orthogonality relationship between modes and the influence of critical speed. The flexural in-plane vibrational equation of the investigated ring is expressed in a concise form in Eq. (7.36). This equation is solved using the Maple package, enabling the determination of the solution for the given system.

Based on the examination of the figures presented in Section 7.7, the following conclusions can be summarized:

a. The maximum deflection at the centers of each segment does not occur when the moving force is at that precise point, but rather when the moving force is leaving that particular segment.

b. The behavior of the system is significantly influenced by the speed of the moving force.

c. When comparing the deflection of any point on the ring, it is significantly more pronounced when the force is in motion along the ring, as opposed to when the force is stationary at a specific location.

d. Since the studied system involves multiple frequency excitations, simultaneous occurrence of more than one resonant condition takes place. Therefore, in addition to the primary natural frequencies, the combination of meshing and carrier frequencies also contributes to the instability of the system.

References

[1] A. Kahraman, A.A. Kharazi, M. Umrani, A deformable body dynamic analysis of planetary gears with thin rims, J Sound Vib. 262 (2003). https://doi.org/10.1016/S0022-460X(03)00122-6.

[2] A. Kahraman, S. Vijayakar, Effect of internal gear flexibility on the quasi-static behavior of a planetary gear set, Journal of Mechanical Design, Transactions of the ASME. 123 (2001). https://doi.org/10.1115/1.1371477.

[3] Y. Hu, D. Talbot, A. Kahraman, A Gear Load Distribution Model for a Planetary Gear Set with a Flexible Ring Gear Having External Splines, Journal of Mechanical Design, Transactions of the ASME. 141 (2019). https://doi.org/10.1115/1.4041583.

[4] S.S. Rao, Effects of transverse shear and rotatory inertia on the coupled twist-bending vibrations of circular rings, J Sound Vib. 16 (1971). https://doi.org/10.1016/0022-460X(71)90662-6.

[5] J.D. Yau, C.M. Wu, Dynamic response of a horizontally curved beam subjected to vertical and horizontal moving loads, Journal of Sound and Vibrations 242 (2001). https://doi.org/10.1006/jsvi.2000.3355.

[6] B.K. Lee, S.J. Oh, K.K. Park, Free vibrations of shear deformable circular curved beams resting on elastic foundations, International Journal of Structural Stability and Dynamics. 02 (2002). https://doi.org/10.1142/s0219455402000440.

[7] R. Davis, R.D. Henshell, G.B. Warburton, Curved beam finite elements for coupled bending and torsional vibration, Earthq Eng Struct Dyn. 1 (1972). https://doi.org/10.1002/eqe.4290010205.

[8] R. Dams, R.D. Henshell, G.B. Warburton, Discussion of Effects of transverse shear and rotatory inertia on the coupled twist-bending vibrations of circular rings, J Sound Vib. 21 (1972). https://doi.org/10.1016/0022-460X(72)90910-8.

[9] C.H. Yoo, J.P. Fehrenbach, Natural frequencies of curved girders. Journal of the Engineering Mechanics Division (1981), 107(2), pp.339-354.

[10] A.O. Lebeck, J.S. Knowlton, A finite element for the three-dimensional deformation of a circular ring, Int J Num Meth. 21 (1985). https://doi.org/10.1002/nme.1620210304.

[11] T.J. McDaniel, Dynamics of circular periodic structures, J Aircr. 8 (1971). https://doi.org/10.2514/3.44245.

[12] V.R. Murthy, N.C. Nigam, Dynamic characteristics of stiffened rings by transfer matrix approach. Journal of Sound Vibration (1975), 39(2), pp.237-245.

[13] K. Singh, B.L. Dhoopar, Free vibration of circular rings on radial supports, J Sound Vib. 65 (1979). https://doi.org/10.1016/0022-460X(79)90521-2.

[14] K.B. Sahay, V. Sundararajan, Vibration of a stiffened ring considered as a cyclic structure, J Sound Vib. 22 (1972). https://doi.org/10.1016/0022-460X(72)90456-7.

[15] A.K. Mallik, D.J. Mead, Free vibration of thin circular rings on periodic radial supports, J Sound Vib. 54 (1977). https://doi.org/10.1016/0022-460X(77)90402-3.

[16] S.S. Rao, V. Sundararajan, In-plane flexural vibrations of circular rings, Journal of Applied Mechanics, Transactions ASME. 36 (1964). https://doi.org/10.1115/1.3564726.

[17] X. Wu, R.G. Parker, Vibration of rings on a general elastic foundation, J Sound Vib. 295 (2006). https://doi.org/10.1016/j.jsv.2006.01.007.

[18] Rao, S. S. Vibration of continuous systems. Vibration of Continuous Systems (2019). https://doi.org/10.1002/9781119424284.

[19] T.E. Lang, Vibration of Thin Circular Rings. Part II. Modal Functions and Eigenvalues of Constrained Semicircular Rings, Jet Propulsion Lab., California Inst. of Tech. Pasadena, USA (1962). Document ID: 19630006566

[20] W. Lacarbonara, A. Arena, S.S. Antman, Flexural vibrations of nonlinearly elastic circular rings, Meccanica. 50 (2015). https://doi.org/10.1007/s11012-014-0038-3.

[21] A.E. Zakrzhevskii, V.F. Tkachenko, V.S. Khoroshilov, Natural modes and frequencies of in-plane vibrations of a fixed elastic ring, International Applied Mechanics. 46 (2011). https://doi.org/10.1007/s10778-011-0436-3.

[22] S. Azimi, In-Plane Vibration of Simply Supported-Simply Supported Circular Ring Segments. Proceedings of the ASME Design Technical Conferences. 13th Biennial Conference on Mechanical Vibration and Noise: Machinery Dynamics and Element Vibrations. Miami, USA. pp. 147-151 (2021). https://doi.org/10.1115/DETC1991-0287.

[23] M. Abedinilaksar, J. Yang, Free in-plane vibration of thin-walled rings with elastic supports, Journal of Mechanical Science and Technology. 37 (2023). https://doi.org/10.1007/s12206-022-1203-6.

[24] R. Hoppe, The bending vibration of circular ring, Crelle Journal of Mathematics 73, pp. 158-168 (1871).

[25] A.E.H. Love, A treatise on the mathematical theory of elasticity. Cambridge University Press 4th edition (2013). ISBN-13: 978-1107618091.

[26] P. Chidamparam, A.W. Leissa, Vibrations of planar curved beams, rings, and arches, Appl Mech Rev. 46 (1993). https://doi.org/10.1115/1.3120374.

[27] J.S. Wu, F.T. Lin, H.J. Shaw, Free in-plane vibration analysis of a curved beam (arch) with arbitrary various concentrated elements, Appl Math Model. 37 (2013). https://doi.org/10.1016/j.apm.2013.02.029.

[28] J.S. Wu, Analytical and Numerical Methods for Vibration Analyses, 2015. https://doi.org/10.1002/9781119137207.

[29] C.S. Huang, Y.P. Tseng, C.L. Hung, An accurate solution for the responses of circular curved beams subjected to a moving load, Int J Numer Methods Eng. 48 (2000). https://doi.org/10.1002/1097-0207(20000830)48:12<1723::AID-NME965>3.0.CO;2-J.

[30] Z. Zhao, S. Wang, J. Xiu, Parametric vibration of an elastic structure with stationary and rotating rings subjected to traveling loads, J Sound Vib. 358 (2015). https://doi.org/10.1016/j.jsv.2015.07.025.

[31] A. V. Metrikine, M. V. Tochilin, Steady-state vibrations of an elastic ring under a moving load, J Sound Vib. 232 (2000). https://doi.org/10.1006/jsvi.1999.2756.

[32] G.L. Forbes, R.B. Randall, Resonance phenomena of an elastic ring under a moving load, J Sound Vib. 318 (2008). https://doi.org/10.1016/j.jsv.2008.05.021.

[33] J. Taheri Kahnamouei, J. Yang, Random vibration analysis of thin-walled elastic rings under multiple moving loads, Proc Inst Mech Eng C J Mech Eng Sci. 236 (2022). https://doi.org/10.1177/0954406221996408.

[34] S.V. Canchi, R.G. Parker, Parametric instability of a circular ring subjected to moving springs, J Sound Vib. 293 (2006). https://doi.org/10.1016/j.jsv.2005.10.007.

[35] S.V. Canchi, R.G. Parker, Effect of ring-planet mesh phasing and contact ratio on the parametric instabilities of a planetary gear ring, Journal of Mechanical Design, Transactions of the ASME. 130 (2008). https://doi.org/10.1115/1.2803716.

[36] H. Ouyang, Moving-load dynamic problems: A tutorial (with a brief overview), Mech Syst Signal Process. 25 (2011). https://doi.org/10.1016/j.ymssp.2010.12.010.

[37] L. Frýba, Vibration of solids and structures under moving loads (Vol. 1). Springer science & business media (2013) DOI: 10.1007/978-94-011-9685-7.

[38] M. Smith, ABAQUS/Standard User's Manual, Version 6.9, Abaqus Documentation, https://classes.engineering.wustl.edu/2009/spring/mase5513/abaqus/docs/v6.6/books/sub/default.htm?startat=ch01s01asb14.html

CHAPTER 8

Summary and Conclusion

8.1 Summary of Dissertation

The primary focus of this Ph.D. dissertation was to investigate the dynamic behavior of a planetary gear train that incorporated an elastic ring gear when subjected to a moving force. In addition, this study also addressed other significant topics concerning PGT dynamics, such as stability analysis and free vibration of thin-walled rings.

Fig. 8.1 offers a graphical representation of the dissertation's structure, followed by short summaries for each topic. The numbers in parentheses in Fig. 8.1 indicate the corresponding chapter numbers of each topic.

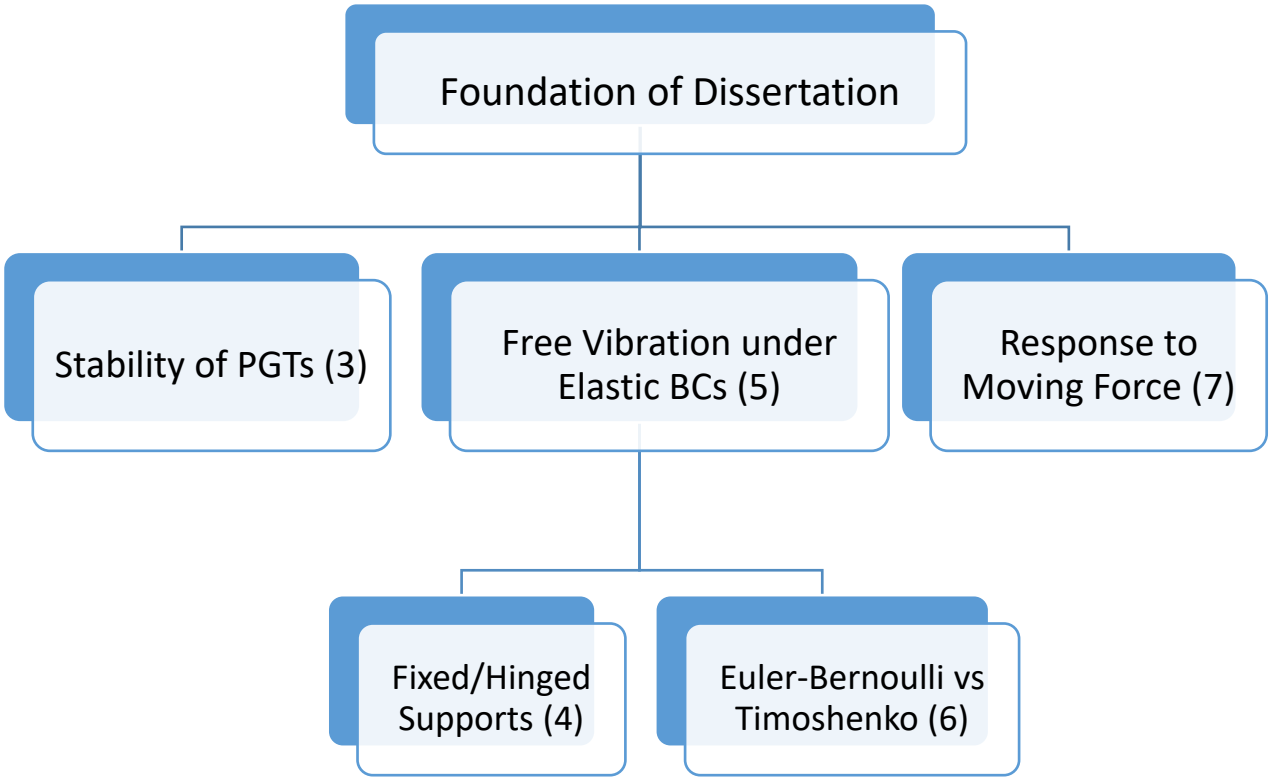

Fig. 8.1 *Structure of dissertation*

8.1.1 Stability of PGTs

Chapter 3 explored the stability of PGT caused by the varying mesh stiffness. The specific objective of this chapter was to investigate the instabilities that arose from repeated natural frequencies in a PGT. The chapter employed the multiple-scale method, which was validated with numerical results from Floquet theory.

8.1.2 Free Vibration under Elastic Boundary Conditions

Understanding the free vibration of thin-walled rings is crucial for conducting further research on the forced response to the moving force. Although this is a classical topic which has been studied since 1970s, works dealing with general elastic boundary conditions are still rare. In Chapters 4 through 6, particular attention was given to the effects of boundary conditions on the response of the ring gear component of a PGT, laying foundation for Chapter 7. The investigation also examined the influence of various model parameters, such as the radius-to-thickness ratio and support stiffness, on the behavior of the system. Validation was made against FEM results obtained from Abaqus simulation.

8.1.3 Response to Moving Force

Chapter 7 served as the central focus of this dissertation, delving into the investigation of the response of a PGT ring subjected to a moving force due to the ring-planet interaction. Method of separation of variables was synergistically applied alongside numerical methods. Leveraging the results obtained from the free vibration analyses in Chapters 4 through 6, the governing PDE was first converted into an ODE, which was then solved using numerical techniques and validated against the previous literature.

8.2 Novelties

Comprehensive lists of results for each chapter can be found in the concluding section of each respective chapter. This section only provides a condensed summary of the top three novelties of this study:

- The present study introduced an enhancement in the formulation of closed-form equations that described the unstable regions of a PGT. The methodology employed in this work exhibited a conservative approach for analyzing a typical PGT, resulting in the identification of a slightly larger unstable region. This improvement was attributed to the inclusion of off-diagonal terms present in the Jordan canonical matrix, which were previously overlooked in the existing literature.

- This study systematically addressed the free vibration behavior of a ring supported by general elastic supports, establishing a crucial groundwork for exploring the dynamics of PGT. Unlike previous literature that primarily focused on hinged and fixed supports, this study showcased the innovative use of general elastic supports, akin to bolt connections. As a result, it opened up promising avenues for further practical applications such as the field of aerospace engineering where the significance of boundary conditions holds a pivotal role.

- The core focus of this work lied in the response of a ring to forced vibration caused by a moving force. The moving force was designed to imitate the force experienced in a PGT when the ring meshed with a planet and was acting as the internal gear. This study represented a pioneering effort in the field of PGT

dynamics, as it is the first of its kind to explore and model this specific phenomenon for such system. It also introduced a novel closed-form formulation for determining the critical speed of a moving force in curvilinear coordinates. By dedicating sufficient effort, it is possible to expand this study to encompass multiple moving forces, thereby presenting a substantial improvement to the existing models of PGT systems.

8.3 Future Work

This research uncovers unexplored avenues, creating opportunities for further studies in this domain. This chapter will not only showcase the novelty of the current investigation but also present potential research directions for future studies. Promising avenues for further research are yet to be explored, unveiling exciting opportunities for future investigators to delve into. Within this context, two specific paths are identified as prospective directions for exploration and investigation. These paths offer potential areas of focus for future researchers to pursue and advance the understanding of the subject matter.

I. The model proposed in this study holds potential for various extensions, presenting opportunities to explore different scenarios. One instance involves considering a realistic case where the planet, carrier, and ring gear possess rotational freedom while the sun gear remains motionless, both in terms of translation and rotation. In this scenario, the system would exhibit five degrees of freedom (DOF). By applying Newton's Law, the governing equation for this system can be expressed as follows:

For the carrier:

$$J_c\ddot{\theta}_c - \sum_{i=1}^{N_P}\left(f_{spi}r_c + f_{rpi}r_c\right)\cos(\sigma) = 0 \tag{8.1}$$

where:

$$J_c = J_{c_0} + N_P m_P {r_c}^2 \tag{8.2}$$

For the planet gears:

$$J_{p_i}\ddot{\theta}_{p_i} - f_{spi}r_{pi} + f_{rpi}r_{pi} = 0 \tag{8.3}$$

For the ring gear:

$$\begin{aligned}&\frac{\partial^6 w(\theta,t)}{\partial\theta^6} + 2\frac{\partial^4 w(\theta,t)}{\partial\theta^4} + \frac{\partial^2 w(\theta,t)}{\partial\theta^2} + \frac{R^4\rho A}{E I}\frac{\partial^2}{\partial t^2}\left(\frac{\partial^2 w(\theta,t)}{\partial\theta^2} - w(\theta,t)\right)\\ &\quad = \frac{R^4}{EI}\sum_{i=1}^{N_P}\left(\left(\frac{\partial f_i(\theta,t)}{\partial\theta} - p_i(\theta,t)\right)\delta(\theta + (i-1)\beta - \omega_c t)\right)\end{aligned} \tag{8.4}$$

where:

$$f_{spi} = k_{spi}\left(-\theta_{p_i}r_{p_i} - \theta_c r_c\cos(\sigma)\right) \tag{8.5}$$

$$f_{rpi} = k_{rpi}\left(\theta_{p_i}r_{p_i} - \theta_c r_c\cos(\sigma) - u.\cos(\gamma) + w.\sin(\gamma)\right) \tag{8.6}$$

In order to represent the above governing equations in a matrix form, the state variables of $\{X\} = \left\{r_c\theta_c, r_{p_1}\theta_{p_1}, r_{p_2}\theta_{p_2}, r_{p_3}\theta_{p_3}, r_r\theta_r = w\right\}$ can be proposed. Thus, the dynamic equation for free vibrations of this system can be expressed as:

$$[M]\{\ddot{X}\} + [K]\{X\} = \{F\} \tag{8.7}$$

where M, K, F, and X are mass, stiffness, force, and state variable matrices, respectively.

The moving load due to the interaction between the ring and planets can be decomposed and expressed into polar u-w coordinates. Eqs. (8.8) and (8.9) represent these relationships as functions of planet-ring pressure angle σ.

$$f_i(\theta, t) = f_{rpi} \cos(\sigma) \tag{8.8}$$

$$p_i(\theta, t) = -f_{rpi} \sin(\sigma) \tag{8.9}$$

Executing the technique used in Chapter 7 of this research for this complicated case will result in:

$$\begin{aligned}
&\ddot{q}_k + {\omega_k}^2 \mathrm{q}_k = \left(U_{1k} \sin^2\left(\frac{k\pi}{\theta_f}\omega_c t\right) + U_{2k} \sin^2\left(\frac{k\pi}{\theta_f}(\beta - \omega_c t)\right) + U_{3k} \sin^2\left(\frac{k\pi}{\theta_f}(2\beta - \right.\right. \\
&\left.\left. \omega_c t)\right)\right) \ddot{q}_k + \left(U_{4k} \sin^2\left(\frac{k\pi}{\theta_f}\omega_c t\right) + U_{5k} \sin^2\left(\frac{k\pi}{\theta_f}(\beta - \omega_c t)\right) + U_{6k} \sin^2\left(\frac{k\pi}{\theta_f}(2\beta - \right.\right. \\
&\left.\left. \omega_c t)\right)\right) q_k + U_{7k} \sin\left(\frac{k\pi}{\theta_f}\omega_c t\right) \dot{\theta}_{p_1} + U_{8k} \sin\left(\frac{k\pi}{\theta_f}\omega_c t\right) \theta_{p_1} + U_{9k} \sin\left(\frac{k\pi}{\theta_f}(\beta - \omega_c t)\right) \dot{\theta}_{p_2} + \\
&U_{10k} \sin\left(\frac{k\pi}{\theta_f}(\beta - \omega_c t)\right) \theta_{p_2} + U_{11k} \sin\left(\frac{k\pi}{\theta_f}(2\beta - \omega_c t)\right) \dot{\theta}_{p_3} + U_{12k} \sin\left(\frac{k\pi}{\theta_f}(2\beta - \right. \\
&\left. \omega_c t)\right) \theta_{p_3} + \left(U_{13k} \sin\left(\frac{k\pi}{\theta_f}\omega_c t\right) + U_{14k} \sin\left(\frac{k\pi}{\theta_f}(\beta - \omega_c t)\right) + U_{15k} \sin\left(\frac{k\pi}{\theta_f}(2\beta - \right.\right. \\
&\left.\left. \omega_c t)\right)\right) \theta_c + U_{16k} \sin\left(\frac{k\pi}{\theta_f}\omega_c t\right) + U_{17k} \sin\left(\frac{k\pi}{\theta_f}(\beta - \omega_c t)\right) + U_{18k} \sin\left(\frac{k\pi}{\theta_f}(2\beta - \omega_c t)\right)
\end{aligned} \tag{8.10}$$

By defining new parameters, Eq. (8.10) can be alternatively expressed as follows:

$$\ddot{q}_k + {\omega_k}^2 \mathrm{q}_k = T_{1k}(t).\ddot{q}_k + T_{2k}(t).q_k + T_{3k}(t).\dot{\theta}_{p_1} + T_{4k}(t).\theta_{p_1} + T_{5k}(t).\dot{\theta}_{p_2} + T_{6k}(t).\theta_{p_2} + T_{7k}(t).\dot{\theta}_{p_3} + T_{8k}(t).\theta_{p_3} + T_{9k}(t).\theta_c + T_{10k}(t) \tag{8.11}$$

Once Eq. (8.11) is derived, the governing equations of the system can be obtained accordingly.

For the carrier:

$$\left(J_{c_0} + N_P m_P {r_c}^2\right)\ddot{\theta}_c - \sum_{i=1}^{N_P}\left(k_{spi}\left(-\theta_{p_i} r_{p_i} - \theta_c r_c \cos(\sigma)\right) + k_{rpi}\left(\theta_{p_i} r_{p_i} - \theta_c r_c \cos(\sigma) - \frac{\dot{w}}{\omega_c}.\cos(\gamma) + w.\sin(\gamma)\right)\right) r_c \cos(\sigma) = 0 \tag{8.12}$$

Or alternatively:

$$J_c\ddot{\theta}_c + R_1\theta_{p_1} + R_2\theta_{p_2} + R_3\theta_{p_3} + R_4\theta_c + R_5\dot{w} + R_6 w = 0 \tag{8.13}$$

For the planet gears:

$$J_{p_i}\ddot{\theta}_{p_i} - k_{spi}\left(-\theta_{p_i} r_{p_i} - \theta_c r_c \cos(\sigma)\right) r_{pi} + k_{rpi}\left(\theta_{p_i} r_{p_i} - \theta_c r_c \cos(\sigma) - \frac{\dot{w}}{\omega_c}.\cos(\gamma) + w.\sin(\gamma)\right) r_{pi} = 0 \tag{8.14}$$

Or alternatively:

$$J_{p_i}\ddot{\theta}_{p_i} + S_{1i}\theta_{p_i} + S_{2i}\theta_c + S_{3i}\dot{w} + S_{4i} w = 0 \tag{8.15}$$

By considering the state variables of $\{X\} = \{\theta_{p_1}, \theta_{p_2}, \theta_{p_3}, w\}$, the governing equations of the system can be presented in a neat matrix form of:

$$[M]\{\ddot{X}\} + [C]\{\dot{X}\} + [K]\{X\} = \{F\} \tag{8.16}$$

Eq. (8.16) can be expanded as follows:

$$\begin{bmatrix} J_{p1} & 0 & 0 & 0 \\ 0 & J_{p2} & 0 & 0 \\ 0 & 0 & J_{p3} & 0 \\ 0 & 0 & 0 & R_1(t) \end{bmatrix} \begin{Bmatrix} \ddot{\theta}_{p1} \\ \ddot{\theta}_{p2} \\ \ddot{\theta}_{p3} \\ \ddot{q}_1 \end{Bmatrix} + \begin{bmatrix} 0 & 0 & 0 & S_{21} \\ 0 & 0 & 0 & S_{22} \\ 0 & 0 & 0 & S_{23} \\ R_3(t) & R_4(t) & R_5(t) & 0 \end{bmatrix} \begin{Bmatrix} \dot{\theta}_{p1} \\ \dot{\theta}_{p2} \\ \dot{\theta}_{p3} \\ \dot{q}_1 \end{Bmatrix}$$
$$+ \begin{bmatrix} S_{11} & 0 & 0 & S_{31} \\ 0 & S_{12} & 0 & S_{32} \\ S_{13} & 0 & S_{13} & S_{33} \\ R_6(t) & R_7(t) & R_8(t) & R_2(t) \end{bmatrix} \begin{Bmatrix} \theta_{p1} \\ \theta_{p2} \\ \theta_{p3} \\ q_1 \end{Bmatrix} = \begin{Bmatrix} 0 \\ 0 \\ 0 \\ T_{91}(t) \end{Bmatrix} \tag{8.17}$$

Eq. (8.17) comprises three ordinary differential equations (ODEs) and one partial differential equation (PDE). The author of this dissertation is presently engaged in the endeavor of identifying an analytical approach to solve this set of coupled equations.

II. All the models investigated in this dissertation have been assumed to be symmetrical. However, when a structure deviates from axisymmetric conditions due to various factors, the behavior of the system can differ qualitatively from that of the idealized representation. Traditional approaches typically analyze the vibration of systems with simple geometries and homogeneous materials. In the presence of perturbations within a system, the harmonic mode shapes can become contaminated by additional wavenumbers as the modes split. Mode splitting occurs when two resonant subsystems, which have the same frequency, become coupled to each other. The perturbed mode shapes, comprising components of other unperturbed mode shapes, can interact with different split modes, resulting in their own splitting. Practical examples of such deviations from axisymmetry can be found in the automotive industry or aircraft tires that are not perfectly axisymmetric.

   An intriguing extension to the current research would be to investigate a ring that is mounted into its frame at different points using various types of supports. Due to this

departure from axisymmetry, a significant alteration is anticipated in the natural frequencies and their corresponding mode shapes. Consequently, some mode pairs could split into singlet modes with distinct frequencies. Therefore, an exploration of the mode contaminations and splits in such a system would enable the determination of the natural frequencies of a ring deviating from axisymmetry.

III. In this study, the motions of a ring are considered in two dimensions, and the focus is solely on analyzing its in-plane vibrational behavior. The equations presented in this work can be modified to include the ring's out-of-plane vibration. A more effective approach to obtain the equations of motion for this scenario involves using the Langrange equation. By applying the Hamilton principle, the equations of motion for a freely vibrating system can be derived from Eq. (8.18), where non-conservative virtual work $\delta W_{nc} = 0$ is set to zero, essentially yielding:

$$\int_{t_1}^{t_2} (\delta T - \delta V) dt = 0 \tag{8.18}$$

where δT and δV are the variations of total kinetic energy T and total potential (or strain) energy V, respectively, while t_1 and t_2 denote the instants of time with zero variations of the associated parameters (or virtual displacements).

Solving this equation will lead to the derivation of the equation of motion for the out-of-plane vibrations of the ring. Readers interested in exploring the thin-walled ring's out-of-plane vibrations are encouraged to study and compare the results with the findings presented in this research.

APPENDICES

Appendix A

Matrix entries for governing equation of a PGT system with three planets (Chapter 3)

$$M_0 = J_c/{r_c}^2 + 3m_p \tag{A1}$$

$$M_1 = J_s/{r_s}^2 \tag{A2}$$

$$M_2 = J_p/{r_p}^2 \tag{A3}$$

$$K_{11} = \sum_{i=1}^{3} \left(k_{sp}^i + k_{rp}^i\right) \cos\gamma \tag{A4}$$

$$K_{12} = K_{21} = -\sum_{i=1}^{3} k_{sp}^i \cos\gamma \tag{A5}$$

$$K_{13} = K_{31} = \left(k_{rp}^1 - k_{sp}^1\right) \cos\gamma \tag{A6}$$

$$K_{14} = K_{41} = \left(k_{rp}^2 - k_{sp}^2\right) cos\,\gamma \tag{A7}$$

$$K_{15} = K_{51} = \left(k_{rp}^3 - k_{sp}^3\right) cos\,\gamma \tag{A8}$$

$$K_{22} = \sum_{i=1}^{3} k_{sp}^{i} \tag{A9}$$

$$K_{23} = K_{32} = k_{sp}^{1} \tag{A10}$$

$$K_{24} = K_{42} = k_{sp}^{2} \tag{A11}$$

$$K_{25} = K_{52} = k_{sp}^{3} \tag{A12}$$

$$K_{33} = k_{sp}^{1} + k_{rp}^{1} \tag{A13}$$

$$K_{44} = k_{sp}^{2} + k_{rp}^{2} \tag{A14}$$

$$K_{55} = k_{sp}^{3} + k_{rp}^{3} \tag{A15}$$

$$K_{34} = K_{43} = K_{35} = K_{53} = K_{45} = K_{54} = 0 \tag{A16}$$

Appendix B

For a ring held at four equally spaced points, Eq. (5.44) will take the form of (B1) where $[G(\omega)]$ is represented as a matrix with $B_{s,i}$ (i=1,2 and s=1-4) components, as follows:

$$[G(\omega)].\{A_{ij}\} = \begin{bmatrix} B_{1,1} & B_{1,2} & 0 & 0 \\ 0 & B_{2,1} & B_{2,2} & 0 \\ 0 & 0 & B_{3,1} & B_{3,2} \\ B_{4,2} & 0 & 0 & B_{4,1} \end{bmatrix}_{24\times24} . \begin{Bmatrix} D_1 \\ D_2 \\ D_3 \\ D_4 \end{Bmatrix}_{24\times1} = 0 \qquad \text{(B1)}$$

where

$$D_p=\{A_{p,1}\ A_{p,2}\ A_{p,3}\ A_{p,4}\ A_{p,5}\ A_{p,6}\}^T \qquad (p=1\text{-}4) \qquad \text{(B2)}$$

$$B_{s,k}=\begin{bmatrix} B_{s,k_{[1,1]}} & B_{s,k_{[1,2]}} & B_{s,k_{[1,3]}} & B_{s,k_{[1,4]}} & B_{s,k_{[1,5]}} & B_{s,k_{[1,6]}} \\ B_{s,k_{[2,1]}} & B_{s,k_{[2,2]}} & B_{s,k_{[2,3]}} & B_{s,k_{[2,4]}} & B_{s,k_{[2,5]}} & B_{s,k_{[2,6]}} \\ B_{s,k_{[3,1]}} & B_{s,k_{[3,2]}} & B_{s,k_{[3,3]}} & B_{s,k_{[3,4]}} & B_{s,k_{[3,5]}} & B_{s,k_{[3,6]}} \\ B_{s,k_{[4,1]}} & B_{s,k_{[4,2]}} & B_{s,k_{[4,3]}} & B_{s,k_{[4,4]}} & B_{s,k_{[4,5]}} & B_{s,k_{[4,6]}} \\ B_{s,k_{[5,1]}} & B_{s,k_{[5,2]}} & B_{s,k_{[5,3]}} & B_{s,k_{[5,4]}} & B_{s,k_{[5,5]}} & B_{s,k_{[5,6]}} \\ B_{s,k_{[6,1]}} & B_{s,k_{[6,2]}} & B_{s,k_{[6,3]}} & B_{s,k_{[6,4]}} & B_{s,k_{[6,5]}} & B_{s,k_{[6,6]}} \end{bmatrix} \qquad (k=1,2) \qquad \text{(B3)}$$

$$B_{s,1_{[1,n]}}=e^{\Upsilon_n\beta_s} \qquad (n=1\text{-}6) \qquad \text{(B4)}$$

$$B_{s,1_{[2,n]}}=\Upsilon_n e^{\Upsilon_n\beta_s} \qquad (n=1\text{-}6) \qquad \text{(B5)}$$

$$B_{s,1}{}_{[3,n]} = \left(1+\Upsilon_n{}^2\right) e^{\Upsilon_n \beta_s} \quad (n=1\text{-}6) \quad (B6)$$

$$B_{s,1}{}_{[4,n]} = \left(-\frac{EI}{R^3}\left(\Upsilon_n{}^3+\Upsilon_n\right)+k_t\right) e^{\Upsilon_n \beta_s} \quad (n=1\text{-}6) \quad (B7)$$

$$B_{s,1}{}_{[5,n]} = \left(-\frac{EI}{R^3}\left(\Upsilon_n{}^3+\Upsilon_n\right)+k_r\right) \Upsilon_n e^{\Upsilon_n \beta_s} \quad (n=1\text{-}6) \quad (B8)$$

$$B_{s,1}{}_{[6,n]} = \left(\frac{EI}{R^2}\Upsilon_n+\frac{k_s}{R}\right)\left(1+\Upsilon_n{}^2\right) e^{\Upsilon_n \beta_s} \quad (n=1\text{-}6) \quad (B9)$$

$$B_{s,2}{}_{[1,n]} = -e^{\Upsilon_n \beta_s} \quad (n=1\text{-}6) \quad (B10)$$

$$B_{s,2}{}_{[2,n]} = -\Upsilon_n e^{\Upsilon_n \beta_s} \quad (n=1\text{-}6) \quad (B11)$$

$$B_{s,2}{}_{[3,n]} = -\left(1+\Upsilon_n{}^2\right) e^{\Upsilon_n \beta_s} \quad (n=1\text{-}6) \quad (B12)$$

$$B_{s,2}{}_{[4,n]} = \left(\frac{EI}{R^3}\left(\Upsilon_n{}^3+\Upsilon_n\right)+k_t\right) e^{\Upsilon_n \beta_s} \quad (n=1\text{-}6) \quad (B13)$$

$$B_{s,2}{}_{[5,n]} = \left(\frac{EI}{R^3}\left(\Upsilon_n{}^3+\Upsilon_n\right)+k_r\right) \Upsilon_n e^{\Upsilon_n \beta_s} \quad (n=1\text{-}6) \quad (B14)$$

$$B_{s,2}{}_{[6,n]} = -\left(\frac{EI}{R^2}\Upsilon_n+\frac{k_s}{R}\right)\left(1+\Upsilon_n{}^2\right) e^{\Upsilon_n \beta_s} \quad (n=1\text{-}6) \quad (B15)$$

In all above equations, the indices ‘s’ and ‘p’ represented the position of the nodes. Since those matrices are derived for a ring with four supports, thus, ‘s’ and ‘p’ will be varied from 1 to 4.